

LOCAL ENVIRONMENT EFFECTS IN SOME *Fe* BASED QUASI-BINARY A_3B AND AB TYPE ALLOYS

THESIS SUBMITTED FOR THE DEGREE OF

DOCTOR OF PHILOSOPHY

BY

T.V.S.M. MOHAN BABU



**SCHOOL OF PHYSICS
UNIVERSITY OF HYDERABAD
HYDERABAD • 500 046
INDIA
AUGUST 1995**

TO

LORD VENKATESWARA

DECLARATION

I hereby declare that the matter embodied in this thesis is the result of investigations carried out by me in the School of Physics, University of Hyderabad, Hyderabad, India, under the supervision of Prof. C. Bansal.

Placet Hyderabad

(T.V.

T.V.S.M. Mohan Babu

S. M. Mohan Babu)

Date : 11.8.1995

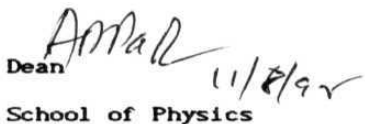
CERTIFICATE

This is to certify that the research work described in this thesis entitled "LOCAL ENVIRONMENT EFFECTS IN SOME Fe BASED QUASI-BINARY A_3B AND AB TYPE ALLOYS", has been carried out by Mr. T.V.S.M. Mohan Babu under my direct supervision and the same has not been submitted for the award of research degree of any university.

Place: Hyderabad

Date t 11.8.95


(Thesis Supervisor)


Dean
11/8/95
School of Physics

ACKNOWLEDGEMENTS

It gives me great pleasure to express **my** sincere gratitude to Prof. C. Bansal, for his excellent guidance and constant encouragement throughout this work.

I **am** thankful to the Dean, School of Physics, for providing necessary facilities.

I am grateful to Prof. **S.N. Kaul** and Dr. G. **Rajaram** for their help during this work and thanks go to other faculty members also.

I thank Prof. Girish Chandra and Dr. **A.K. Nigam** at Tata Institute of Fundamental Research, Bombay, for allowing me to use their low temperature **Mössbauer** set up.

I would like to thank the Principal Scientific Officer, **CIL** and other staff for their help.

I must thank Mr. **Goutam**, Mr. P.D. Babu, Dr. Ch.V. Mohan, Dr. M.S. Rao, Dr. Y.S. Rao, Dr. V. Siruguri and other colleagues for their timely help.

I thank Mr. Ravi Sankar and other staff in School of Physics and Mr. Prasad, Glass Blowing Section, for extending their **co-**operation.

Financial Assistance in the form of Senior Research Fellowship from Council of Scientific and Industrial Research, India is greatly acknowledged.

Finally, I express my deep gratitude to my parents, who supported me throughout all these years with their love and encouragement. I am grateful to my wife, **Naga Lakshmi** and my

son, **Tarun** for their love and **moral** support. I like to thank my sisters and all other **family members** for their constant support and encouragement.

CONTENTS

	Page
List of Publications	i
List of Figures	iv
List of Tables	xiii
CHAPTER 1: INTRODUCTION	1-42
1.1. Crystal Structures and Phases	3
1.2. Order-Disorder Effects	6
1.3. Kinetics of Ordering	8
1.4. Magnetic Properties	10
2. Mossbauer Effect	15
2.1. Hyperfine Interactions	20
a. Isomer Shift	20
b. Nuclear Dipole Interaction or Zeeman Effect	24
c. Electric Quadrupole Interaction	27
d. Contributions to EFG	29
3. Ferromagnetic Resonance	31
References	38
CHAPTER 2s EXPERIMENTAL TECHNIQUES	43-64
2.1. Mossbauer Spectrometer	43
a. Velocity Drive and Feedback System	43
b. Gamma Ray Detection System	45
c. μP based Data Acquisition System	46
d. Low Temperature Measurements	49

2.2. Mössbauer Data Analysis	51
2.3. Ferromagnetic Resonance Spectrometer	54
2.4. AC susceptibility	60
2.5. Sample Preparation	61
2.6. Characterisation of Samples	62
References	64

CHAPTER 3: MAGNETIC BEHAVIOUR IN $\text{Fe}_{3-x}\text{Mn}_x\text{Si}$ ALLOYS 65-112

3.1. Introduction	65
3.2. Experimental	69
3.3. Results	69
a. AC susceptibility	69
b. Ferromagnetic Resonance	72
c. Mössbauer Spectroscopy	81
3.4. Discussion	102
a. Effect of Preferential Substitution of Mn on Exchange Interactions	105
b. Spin Canting and Magnetic Structure	106
3.5. Conclusions	110
References	111

CHAPTER 4: SITE SUBSTITUTION BEHAVIOUR AND SOLUBILITY

LIMIT IN $\text{Fe}_{3-x}\text{Cr}_x\text{Si}$ ALLOYS	113-137
4.1. Introduction	113
4.2. Experimental and Data Analysis Procedure	114

4.3. Results and Discussion	119
a. Solubility Limit of Cr	119
b. Hyperfine Fields and Local Environment Model	120
c. Chemical Ordering and Kinetic Path Approach	127
d. Isomer Shift Behaviour	133
4.4. Conclusions	134
References	136

CHAPTER 5s EFFECT OF CHEMICAL ORDER ON THE MAGNETIC	
PROPERTIES OF Fe Mn Al ALLOYS AND KINETICS OF	
ORDERING IN Fe₈Mn₁Al₂	138-159
5.1. Introduction	138
5.2. Experimental	140
5.3. Results and Discussion	141
a. Hyperfine Fields in Disordered Alloys	143
b. Hyperfine Fields in Ordered Alloys	146
c. Chemical Ordering and Reentrant Behaviour in	
Fe₁₈Mn₁Al₂	148
d. Kinetics of Ordering in Fe₈Mn₁Al₂	150
5.4. Conclusions	157
References	158

CHAPTER 6: EFFECT OF Si SUBSTITUTION ON THE ORDERING OF	
Ni₃Fe AND SITE SUBSTITUTION EFFECTS IN	
Ni₃Fe_{1-x}Si_x ALLOYS	160-172
6.1. Introduction	160
6.2. Experimental	161

6.3. Results and Discussion	162
a. X-ray Diffraction	162
b. Hyperfine Fields, Linewidths and Magnetic Dilution in Disordered Alloys	164
c. Chemical Ordering Effects	167
6.4. Conclusions	171
References	172
CHAPTER 7: QUADRUPOLE SPLITTING IN FeSi AND EFFECT OF Ni	
SUBSTITUTION IN (Fe, Ni)_{1-x}-Si_x - ALLOYS 173-189	
7.1. Introduction	173
7.2. Experimental	175
7.3. Results and Discussion	175
a. X-ray Diffraction	175
b. Mössbauer Spectroscopy	177
c. Resonating Valence Bond Theory and Valence State of Si and Fe	184
d. Quadrupole Splitting in FeSi	185
e. Effect of Ni substitution on Quadrupole Splitting and Isomer Shift Behaviour	186
7.4. Conclusions	188
References	189
SUMMARY	190

LIST OF PUBLICATIONS

PAPERS PUBLISHED IN INTERNATIONAL JOURNALS

- (1) "**Spin-wave** stiffness and the range of exchange interaction in amorphous $(\text{Fe}_{1-x}\text{Ni}_x)_{75}\text{B}_{25}$ and $(\text{Fe}_{1-y}\text{W}_y)_{83}\text{B}_{17}$ " (M.Phil. work)
S.N. Kaul and T.V.S.M. Mohan Babu
J. Phys. Condense Matter **1**, 8509(1989).
- (2) "**A** Mossbauer Effect Study of Ni substitution in **equiatomic** FeSi"
T.V.S.M. Mohan Babu and C. Bansal
Phys. Stat. Sol.(b) **177**, **K83**(1993).
- (3) "A Mossbauer Effect Investigation of Fe hyperfine fields and Solubility limit of Cr in $\text{Fe}_{\frac{2}{3}-x}\text{Cr}_x\text{Si}$ alloys"
T.V.S.M. Mohan Babu and C. Bansal
Phys. Stat. Sol.(b) **180**, 479(1993).
- (4) "Evidence for Re-entrant behaviour in crystalline compound Fe_2MnSi "
T.V.S.M. Mohan Babu, C. Bansal and S.N. Kaul
AIP Conf. Proceedings 286, 297(1994).
- (5) "Study of Disorder-Order transformation in $\text{Fe}_2\text{Mn}_{\frac{2}{3}}\text{Si}$ by **Mössbauer Spectroscopy**"
T.V.S.M. Mohan Babu and C. Bansal
AIP Conf. Proceedings **286**, 294(1994).
- (6) "**Magnetic** Behaviour of Ordered $\text{Fe}_{\frac{2}{3}-x}\text{Mn}_x\text{Si}$ **Reentrants**"
T.V.S.M. Mohan Babu, C.Bansal and S.N. Kaul
J. Magn. Magn. Mater. **140-144**, 127(1995).

- (7) "A **Mössbauer** Effect Study of $\text{Ni}_{1-x}\text{Fe}_x\text{Si}$ alloys with $0 < x \leq 0.9$ ".

T.V.S.M. Mohan Babu and C. Bansal

Communicated to Phys. Stat. **Sol.(b)**

- (8) "A Mossbauer Effect study of chemical and magnetic order in $\text{Fe}_{0.75-x}\text{Mn}_x\text{Al}_{0.25}$ alloy system and Disorder-order kinetics in $\text{Fe}_{0.45}\text{Mn}_{0.3}\text{Al}_{0.25}$ "

T.V.S.M. Mohan Babu and C. Bansal

Accepted for Publication in Phys. Stat. **Sol.(b)**

- (9) "Detailed AC susceptibility, Mossbauer Effect and Ferromagnetic resonance study of ordered $\text{Fe}_{1-x}\text{Mn}_x\text{Si}$ alloy"

To be communicated.

- (10) "Evidence for reentrant behaviour in ordered $\text{Fe}_{1/8}\text{Mn}_{1/2}\text{Al}$ "
- To be communicated.

PAPERS PRESENTED **IN NATIONAL CONFERENCES/SYMPOSIA**

- (1) "FMR study of amorphous $(\text{Fe}_{1-x}\text{Ni}_x)_{75}\text{B}_{25}$ and $(\text{Fe}_{1-y}\text{W}_y)_{83}\text{B}_{17}$ alloys" (M.Phil. work)

T.V.S.M. Mohan Babu and S.N. Raul

Solid State Physics (India) **Vol. 31C, 234(1988)**.

- (2) "A Mossbauer Effect Study of **Ni** substitution in **equiatomic FeSi**"

T.V.S.M. Mohan Babu and C. Bansal

Solid State **Pjysics** (India) Vol. **34C**, 92(1991).

- (3) "A Mossbauer Effect Investigation of Fe hyperfine fields in $\text{Fe}_{1-x}\text{Cr}_x\text{Si}$ alloys"

T.V.S.M. Mohan Babu and C. Bansal

Solid State Physics (India) Vol. **35C**, 131(1992).

(4) "Re-entrant Behaviour in Ordered Fe_2MnSi alloys"

T.V.S. M. Mohan Babu, C. Bansal and S.N. Kaul

Solid State Physics (India) Vol.36C, 148(1993).

(5) "Influence of Chemical Order on the Magnetic State of

$\text{Fe}_{1-x}\text{Mn}_x\text{Al}$ alloy"

T. V. S. M. Mohan Babu and C. Bansal

Solid State Physics (India) Vol.37C, 156(1994).

LIST OF FIGURES

	Page
CHAPTER 1	
Fig.1.1.1. Typical ternary phase diagram showing quasi-binary and pseudo-binary sections.	2
Fig.1.1.2. Crystal structures appearing in different concentration ranges for $\text{Fe}_{3-x}\text{V}_x\text{Ge}$ alloy system [7].	4
Fig.1.1.3. Mössbauer spectra for as quenched alloys of Fe-50 at% Co (a), Fe-49 at% Co-2at%Mo (b) and Fe - 48 at% Co - 4 at % Mo (c)[15].	7
Fig.1.1.4. Kinetic paths for ternary (ABC) alloys started at same initial state but ordered at different temperatures [15].	9
Fig.1.1.5. Numerically obtained results by Anthony and Fultz (20) from Master Equation formalism for variation of B2, DO_3 , and B2 order parameters in Fe_3Al .	11
Fig.1.1.6 a. Kinetic paths of LRO for Fe_3Al as measured using X-ray diffraction [57].	12
b. Kinetic paths of short range ordering (SRO) for Fe_3Al using Mössbauer spectroscopy [57].	12
Fig.1.1.7 a. γ -ray emission and absorption lines with a shift due to the recoil energy E_R for gamma emission and absorption from a nucleus at rest.	17
b. Small overlap of emission and absorption lines due to Doppler broadening (E_D) for a gas of atoms at finite temperature.	17

Fig.1.8	a. Schematic diagram of Mössbauer experiment.	19
	b. Schematic representation of resonance emission and absorption of γ-ray .	19
	c. Typical Mössbauer spectrum which consists of intensity of γ-rays detected by the detector as a function of relative velocity between source and absorber.	19
Fig.1.9.	Representation of Isomer shift (a), Nuclear Zeeman Splitting (b), Quadrupole splitting (c), Thermal red shift (d) and their typical Mössbauer spectra.	22
Fig.1.10.	Typical FMR first derivative (dP/dH) absorption spectrum.	37
CHAPTER 2		
Fig.2.1.	Block diagram of Mossbauer Spectrometer.	44
Fig.2.2.	Flow chart to implement low dead time in data acquisition.	48
Fig.2.3.	Set-up for Variable temperature Mossbauer experiments using closed cycle refrigerator .	50
Fig.2.4.	Block diagram of FMR Spectrometer.	55
Fig.2.5	a. Quartz rod with a half cut at one end and a groove to place the sample.	57
	b. Sample is sandwiched between the half cut end of the quartz rod and quartz piece. Copper-constantan thermocouple is attached to the quartz rod.	57

- c. The quartz rod with sample and thermocouple is pushed into a quartz tube. 57

Fig.2.6 a. Horizontal-parallel (\parallel^H) sample geometry in which the static magnetic field H lies in the sample plane and is directed along the length of the sample. 59

- b. Vertical-parallel (\parallel^V) sample geometry in which the static magnetic field H lies in the sample plane and is directed along the breadth of the sample. 59

CHAPTER 3

Fig.3.1. DO_3 structure with A, B, C, and D sublattices having origins at $(0,0,0)$, $(1/4,1/4,1/4)$, $(1/2,1/2,1/2)$ and $(3/4,3/4,3/4)$ along the body diagonal. 66

Fig.3.2 a. Variation of AC susceptibility (χ) with temperature (T) for $\text{Fe}_{1-x}\text{Mn}_x\text{Si}$ alloys. 70

- b. Variation of dc magnetisation (M) with temperature (T) for $x = 0.75$ and $x = 0.90$ alloy compositions. 70

Fig.3.3. FMR power absorption derivative spectra at different temperatures for Fe_2MnSi alloy. 73

Fig.3.4. Variation of the FMR resonance field (H_{res}) with temperature (T) in $\text{Fe}_{1-x}\text{Mn}_x\text{Si}$ alloys. 75

Fig.3.5. The dependence of saturation magnetisation (M_S) on temperature (T) for $\text{Fe}_{1-x}\text{Mn}_x\text{Si}$ alloys. 76

- Fig.3.6.** Variation of $\frac{[M_S(0) - M_S(T)](D(T))^{3/2}}{2(3/2, t_H)}$ with $T^{3/2}$ in $\text{Fe}_{3-x}\text{Mn}_x\text{Si}$ alloys. 80
- Fig.3.7.** Variation of FMR linewidth (ΔH) with T/T_{\min} in $\text{Fe}_{3-x}\text{Mn}_x\text{Si}$ alloys. 82
- Fig.3.8.** Mössbauer spectra and their hyperfine field distributions (calculated using model-independent Le Cäer program) at different temperatures for $\text{Fe}_{2.25}\text{Mn}_{0.75}\text{Si}$ alloy. 84
- Fig.3.9.** Correlation between Fe hyperfine field and magnetic moment (μ_F) for AC site Fe atoms. The number of Mn nn atoms for these sites is indicated by n. 86
- Fig.3.10.** Temperature dependence of hyperfine field (H_{hf}) for Fe(AC) atoms having different number of Mn near neighbours (n) for $\text{Fe}_{2.25}\text{Mn}_{0.75}\text{Si}$ alloy. 87
- Fig.3.11.** Mössbauer spectra and their hyperfine field distributions (calculated using model-independent Le Cäer program) at different temperatures for $\text{Fe}_{2.1}\text{Mn}_{0.9}\text{Si}$ alloy. 89
- Fig.3.12.** Temperature dependence of hyperfine field (H_{hf}) for Fe(AC) atoms having different number of Mn near neighbours (n), and Fe(B) atoms with 8 Fe and 6 Fe near neighbours for $\text{Fe}_{2.1}\text{Mn}_{0.9}\text{Si}$ alloy. 93

- Fig.3.13.** Variation of mean hyperfine field (H_{hf}) and isomer shift parameters (A and B defined in Eq. 3.12) with temperature (T) for $Fe_{21}Mn_{28}Si$ alloy. 95
- Fig.3.14.** Temperature dependence of isomer shift (δ_n) for Fe(AC) atoms having different number of Mn near neighbours (n) for $Fe_{21}Mn_{28}Si$. 96
- Fig.3.15.** Mössbauer spectra and their hyperfine field distributions (fitted to two Gaussians) at different temperatures for Fe_2MnSi alloy. 97
- Fig.3.16.** Mössbauer spectra and their hyperfine field distributions (fitted to two Gaussians) at different temperatures for $Fe_{18}Mn_{12}Si$ alloy. 99
- Fig.3.17** a. Temperature dependence of hyperfine field \overline{H}_{hf}^L (lower field) and \overline{H}_{hf}^H (higher field) for Fe_2MnSi alloy. 103
- b. Variation of area under low field peak (LFS) and high field peak (HFS) for Fe_2MnSi . 103
- Fig.3.18** a. Temperature dependence of hyperfine field \overline{H}_{hf}^L (lower field) and \overline{H}_{hf}^H (higher field) for $Fe_{18}Mn_{12}Si$ alloy. 104
- b. Variation of area under low field peak (LFS) and high field peak (HFS) for $Fe_{18}Mn_{12}Si$. 104
- Fig.3.19** a. Schematic representation of Fe and Mn atomic moments on AC and B sites and their exchange interactions with neighbours. 107
- b. Canting of Mn spins at low temperatures. 107

- c. Frustration at Fe(AC) site due to **antiferromagnetic** ordering on B sublattice. 107

Fig.3.20. Magnetic phase diagram for **Fe₂** Mn Si alloy system. 109

CHAPTER 4

Fig.4.1. The complete fitted spectrum for **Fe₂Si** using the stripping procedure as discussed in Section 4.2. 116

Fig.4.2. (a) and (b) are the residual spectra for **Fe₂ 75Cr₀ 25Si** after stripping B and AC fields respectively. The **Mössbauer** spectrum fitted with a field distribution comprising of five gaussians is shown in (c) and the corresponding field distribution is shown in (d). 121

Fig.4.3. **Mössbauer** spectra of **Fe_{1-x}Cr_xSi** alloys for $x \geq 0.5$, fitted to a field distribution consisting of a superposition of four Gaussian peaks (Eq. 4.1) and the corresponding hyperfine field distributions. 125

Fig.4.4. Variation of hyperfine fields with Cr concentration for different nn **configurations**. 126

Fig.4.5. Probability of low field peak, $P(0)$, as a function of Cr concentration. 128

Fig.4.6. Probability of Fe(B) sites with **8 Fe 1nn**, $P(8)$, vs. probability of Fe(AC) sites with **4 Fe 1nn**, $P(4)$. 130

- Fig.4.7** a. The possible ordered structures in **bcc Fe₃Si** (i) B2; (ii) **DO₃**; (iii) B32. 132
- b. Calculated probabilities of Fe atoms with different number of Fe atoms in 1 nn shell for these structures. 132
- Fig.4.8.** Dependence of **isomer** shift δ (relative to α - Fe) on Cr concentration for various nn configurations. 134
- CHAPTER 5
- Fig.5.1.** Phase diagram for disordered **Fe-Mn-Al** alloy system [9]. 142
- Fig.5.2.** Room temperature Mossbauer spectra for disordered **Fe_{3-x}Mn_xAl** alloys and hyperfine field distributions calculated using model-independent Le Cäer program. 144
- Fig.5.3** a. Variation of average hyperfine field, H_{hf} , with Mn concentration (x) for disordered **Fe_{3-x}Mn_xAl** alloys. 145
- b. Variation of Curie temperature, T_C , with Mn concentration x for disordered **Fe_{3-x}Mn_xAl** alloys. 145
- Fig.5.4.** Room temperature Mössbauer spectra for ordered **Fe_{3-x}Mn_xAl** alloys and hyperfine field distributions calculated using model-independent Le Cäer program. 147
- Fig.5.5.** Dependence of hyperfine field on number of Fe atoms as near neighbours of an Fe atom in ordered **Fe_{2.4}Mn_{0.6}Al**. 149

- Fig.5.6.** Temperature dependence of magnetisation for ordered $\text{Fe}_{1.8}\text{Mn}_{1.2}\text{Al}$ alloy. 151
- Fig.5.7.** Room temperature Mössbauer spectra for $\text{Fe}_{1.8}\text{Mn}_{1.2}\text{Al}$ annealed at different times, and corresponding hyperfine field distributions obtained by fitting data to two Gaussian field distributions. 152
- Fig.5.8.** Time dependence of the intensity of low field Gaussian (a) and high field Gaussian (b). 154
- CHAPTER 6
- Fig.6.1.** Variation of lattice parameter (a) for fcc unit cell with Si concentration (x) in $\text{Ni}_3\text{Fe}_{1-x}\text{Si}_x$ system. 163
- Fig.6.2.** Quasi-binary section of the phase diagram for $\text{Ni}_3\text{Fe}_{1-x}\text{Si}_x$ alloy system. 165
- Fig.6.3.** Mossbauer spectra for splat quenched alloys: Ni_3Fe (a), and $\text{Ni}_3\text{Fe}_{0.75}\text{Si}_{0.25}$ (b). 166
- Fig.6.4.** Mossbauer spectra for ordered $\text{Ni}_3\text{Fe}_{1-x}\text{Si}_x$ alloys of various compositions subjected to the ordering heat treatment as discussed in text. 169
- Fig.6.5.** Observed variation of average hyperfine field, H_{hf} , in the $\text{Ni}_3\text{Fe}_{1-x}\text{Si}_x$ alloy system. 170

CHAPTER 7

- Fig.7.1.** B20 cubic structure of FeSi. 174
- Fig.7.2.** Powder X-ray diffraction patterns for $(\text{Fe}_{1-x}\text{Ni}_x)_{0.5}\text{Si}_{0.5}$ alloys with $x = 0, 0.25$ and 0.6 . 176
- Fig.7.3.** Mossbauer spectra of $(\text{Fe}_{1-x}\text{Ni}_x)_{0.5}\text{Si}_{0.5}$ alloys for various nickel concentrations (x). 181

Fig.7.4. Variation of cubic lattice parameter (a), **isomer** shift δ (relative to α - Fe) and quadrupole splitting A with nickel concentration (x) in $(\text{Fe}_{1-x}\text{Ni}_x)_{0.5}\text{Si}_{0.5}$ alloys.

LIST OF TABLES

	Page
Table 1.1. Solubility limits for 3d transition metals in the $\text{Fe}_{3-x}\text{T}_x\text{Si}$ alloy systems at room temperature (Ref. 13).	5
Table 3.1. Near neighbour configurations of (AC), B and D sites in the DO_3 structure. The near neighbour distance is in units of lattice constant a.	67
Table 3.2. Magnetic transition temperatures and spin wave parameters for $\text{Fe}_{3-x}\text{Mn}_x\text{Si}$. Numbers in brackets indicate errors.	79
Table 4.1. The final values of parameters b, r, AQ , and GIS as function of x in $\text{Fe}_{3-x}\text{Cr}_x\text{Si}$ alloys.	118
Table 4.2. Hyperfine fields and magnetic moments for different nn configurations in $\text{Fe}_{3-x}\text{Cr}_x\text{Si}$ alloys.	123
Table 7.1. Indexing of Powder X-ray diffraction pattern for FeSi.	178
Table 7.2. Indexing of Powder X-ray diffraction pattern for $(\text{Fe}_{0.75}\text{Ni}_{0.25})_{0.5}\text{Si}_{0.5}$.	179
Table 7.3. Indexing of Powder X-ray diffraction pattern for $(\text{Fe}_{0.75}\text{Ni}_{0.6})_{0.5}\text{Si}_{0.5}$.	180
Table 7.4. Coordinates of Si atoms in the rotated frame and their contribution to EFG at Fe .	183

CHAPTER 1

INTRODUCTION

Many alloys of technological and commercial interest are Bulticomponent alloys and a basic physical understanding of these alloys is complicated but necessary for their designing, **processing** and improvement in performance. For **example, commonly** used materials such as Stainless **steel**, Alnico, Heusler **alloys**, **Sendust**, **Pernendur** etc. are ternary or **multicomponent** alloys **developed** for practical applications. Binary alloys have been **studied** extensively and understood both theoretically and **experimentally** but relatively less is understood for ternary systems. Compilation of ternary phase diagrams have begun appearing in **literature [1-3]**, and important work has been undertaken to study their order-disorder behaviour and kinetics **[4,5]**, magnetic behaviour **[6]** etc.

Because of the wide composition range and phases present in ternary alloys, it is much easier to concentrate on specific regions of compositions (Fig. 1.1) which are called **quasi-binary** or pseudo-binary sections. A section taken through two **congruently** melting compounds (e.g. line 2-3 in Fig. 1.1) or one metal and a congruently melting compound on **opposite** face (line 1-2) is termed quasi-binary whereas when percentage of one component is held fixed (line 4-5) or the ratio of two constituents is held constant (line 1-5) one gets pseudo-binary alloys. In the present thesis, work is presented on ternary alloys based on **A₂B** and AB type **intermetallic** compounds.

We first discuss typical illustrative examples of systematic behaviour of crystal structures, phase **formation**, chemical **order-**

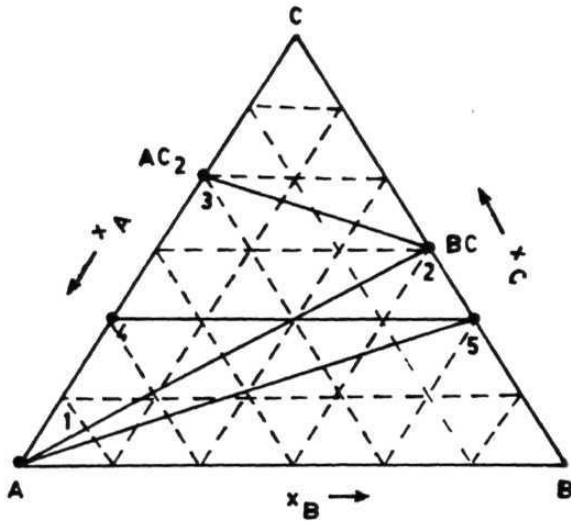


Fig.1.1.1. Typical ternary phase diagram showing quasi-binary (lines 1 - 2, 2 - 3) and pseudo-binary sections (lines 4 - 5, 1 - 5). x_A , x_B , x_C are the concentrations of A, B, C elements respectively.

ing behaviour and magnetic behaviour etc. observed with ternary additions present in quasi-binary or pseudo-binary systems.

1.1. Crystal Structures and Phases

The end members (Fe_3Ge and V_3Ge) of the Quasi-binary system ($\text{Fe}_{1-x} \text{V}_x$)₃Ge have hexagonal close packed (DO_{19}) and cubic (A15) structures respectively. For concentration ranges $0 \leq x \leq 0.10$ the hcp structure of Fe_3Ge persists in the ternary system [7]. Similarly on the other side for $0.55 \leq x \leq 1.0$ the A15 structure of V_3Ge is formed but in the intermediate composition range $0.19 < x \leq 0.28$ the fcc DO_3 structure is obtained (Fig. 1.2). In the case of the quasi-binary $\text{Fe}_3 \text{Mn}_{1-x} \text{Si}_x$ system, both the end members Fe_3Si and Mn_3Si have fcc DO_3 structure and solid solutions which are formed in the complete concentration range also have fcc DO_3 structure. Ternary alloys of Fe_3Si with other metals such as Ni, Co, Cr etc. (end members Ni_3Si is fcc L1₂, Cr_3Si has cubic A15 structure whereas Co_3Si phase has not been found) do not form in the entire composition range and show solubility limited behaviour upto different concentration ranges (Table 1.1).

The phase formation in ternary systems of transition elements with Al in alloys such as Fe-Mn-Al, Mn-Ti-Al, Mn-Ni-Al is considerably altered with the presence of Al [7]. Al stabilises the bcc phase and suppresses the β -Mn electron phase of the transition element rich region. Chapter 3 of this thesis which discusses work on Fe-Mn-Al system shows the presence of CsCl type B2 order in the bcc phase field which is obtained by presence of Al.

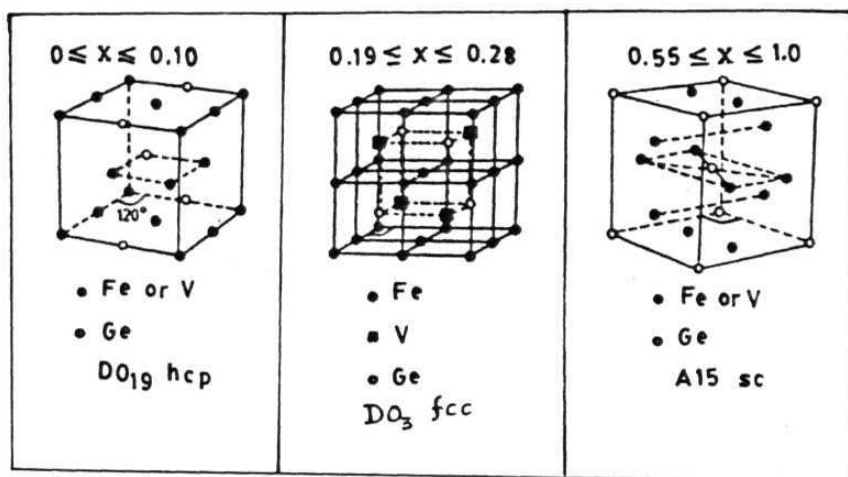


Fig.1.2. Crystal structures appearing in different concentration ranges for $\text{Fe}_{3-x}\text{V}_x\text{Ge}$ alloy system [7].

Table **1.1.** Solubility **limits** for 3d transition metals in the **Fe-T** Si alloy system at room temperature **[13]**.

Metal (T)	Concentration limit
Ti	0.7 (Ref.59)
V	1.0
Cr	0.5 (Ref.58)
Mn	3.0
Co	2.15
Ni	0.8 - 1.0

1.2. Order-Disorder Effects

Many studies have been conducted on ordering in ternary or **multicomponent** alloys [9] but a quantitative understanding becomes difficult owing to the limitations of conventional diffraction techniques with X-rays, electrons or neutrons in determining quantities with respect to the atomic **configurations** or order parameters in ternary and **multinary** alloy systems. For an **n-component** alloy, removal of a symmetry element due to the ordering **transformation** [10] yields $(n - 1)$ long-range order parameters (**LRO**) which are necessary to characterise the degree of order. In the binary case $n = 2$, and the structure factor **of** a superlattice reflection involves only one LRO parameter which can be determined. For ternary system, the intensity of superlattice reflection cannot be used to extract the two order **parameters** unless the scattering factors of elements are varied. This involves study with variation in X-ray wavelength or isotopic substitution and though elegant in principle, requires **experimental** facilities of synchrotron source or atomic reactor [11-12]. But for iron based alloys **Mössbauer spectroscopy** has been fruitfully employed to study ordered atom **configurations** in ternary alloys [13-17]. Although restricted to Fe and Sn based systems this technique has a potential for yielding information on atomic configurations in these systems which is not possible by **other** methods. In the ternary Fe-Co-Mo system for example, the effect of Co on ^{57}Fe **Mössbauer** spectra could be clearly **distinguished** from the effect of Mo [15]. As shown in Fig. 1.3, the presence of

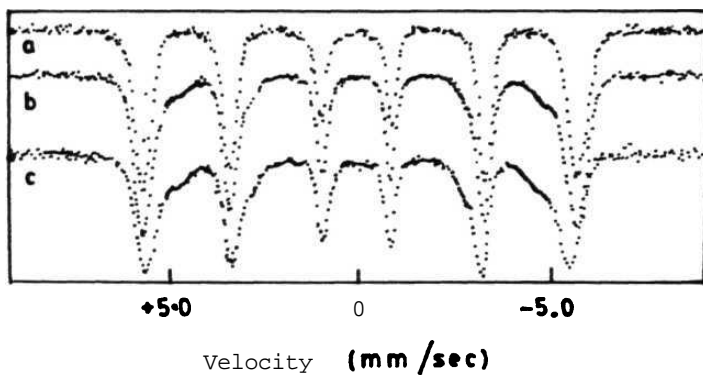


Fig.1.3. Mössbauer spectra for as quenched alloys of Fe-50 at% Co (a), Fe-49 at% Co-2at%Mo (b) and Fe - 48 at% Co - 4 at % Mo (c). The darkend places shows the satellite peaks due to Fe atoms having Mo atoms as first and second nearest neighbours [15].

Mo first and second neighbours give satellite lines in the spectrum whereas Co neighbours affect the mean hyperfine field or width of the main peak. Two **Warren-Cowley** short-range order parameters involving $\langle \text{Co/Fe} \rangle$ correlation and $\langle \text{Mo/Fe} \rangle$ correlations could be separately determined for different states of **chemical** order in the system. This sensitivity of the **Mössbauer** technique to local neighbour **configurations** has been used to study order-disorder effects in this thesis.

1.3. Kinetics of Ordering

The kinetic approach from disordered state of an **alloy** to ordered state is also of great interest. The mechanism of atom movements affects the temporal rate at which **thermodynamic equilibrium** is achieved. Direct atom-atom interchange or atom-vacancy interchange mechanisms have been used to set up rate **equations** and calculate **SRO** and **LRO** relaxations in **binary** alloys [18]. For a single observable order parameter an alloy would go through the same non-equilibrium states of order for all temperatures and initial conditions except for anomalies such as overshoots or reversals of the trajectory near the end state [19]. However with more order parameters there is a possibility of different "**kinetic paths**" as shown by Anthony and **Fultz** [20]. The path of the alloy through the space spanned by two order parameters is termed its kinetic path. For B2 ordering in a ternary alloy the kinetic path in two order parameters were found to be temperature dependent when the three atomic species (ABC) had either different interatomic potentials or diffusive jump energies. With the B2

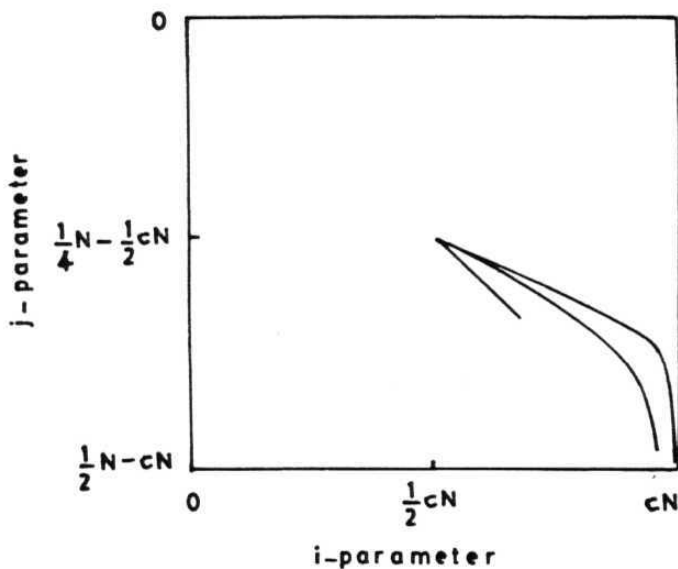


Fig.1.4. Kinetic paths for ternary (ABC) alloys started at same initial state but ordered at different temperatures [15]. i and j are the number of C atoms and A atoms respectively on the α -sublattice of B2 structure. c is the concentration of C atom species and N is the total number of sites; $0 < i < cN$, and j can range from $N/2 - cN$ (perfect order) to $N/4 - cN/2$ (zero order), to 0 (perfect order of opposite phase).

structure represented as two interpenetrating simple cubic lattices α and β , order parameters were defined for occupancy of these sublattices by different atoms. Fig. 1.4 shows a plot of order parameter i (number of C atoms on the α sublattice) against order parameter j (number of A atoms on α sublattice) at different temperatures [15]. An experimental study of kinetic paths in Fe-Co-Mo ternary system gave temperature dependent kinetic paths and were understood in terms of high diffusive energy for Mo diffusion.

It was also shown that for a binary alloy with AB_2 stoichiometry on a bcc lattice, different combinations of B2 and DO_{19} order can develop along its kinetic path towards equilibrium. The relative rates of B2 and DO_{19} ordering (and hence kinetic path in B2 and DO_{19} space) were found to depend on the relative strengths of the interatomic potentials and on temperature. A transient B2 structure was observed to develop at early times (Fig. 1.5). Both these were experimentally verified as shown in Fig. 1.6 by Mössbauer studies in Fe_2Al system [21].

1.4. Magnetic Properties

The magnetic properties of 3d transition metal alloys with competing exchange interactions are extremely interesting because of the wide variety of magnetically ordered states possible in these systems. In these alloys one can go continuously from spin glass ordering to ferromagnetic ordering by varying the concentration [22]. In between the two limits a new type of behaviour

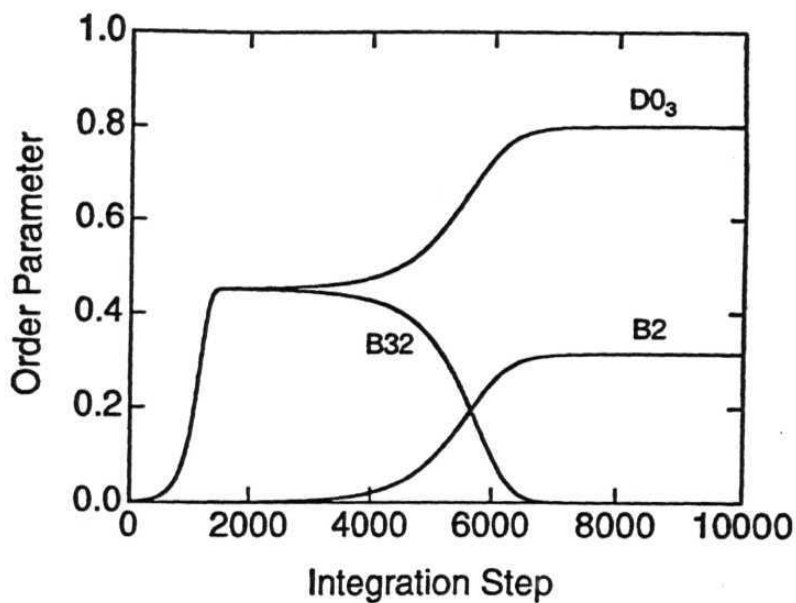


Fig.1.5. Numerically obtained results by Anthony and **Fultz** (20) from Master Equation formalism for variation of $B2$, $D0$ and $B2$ order parameters in Fe_3Al .

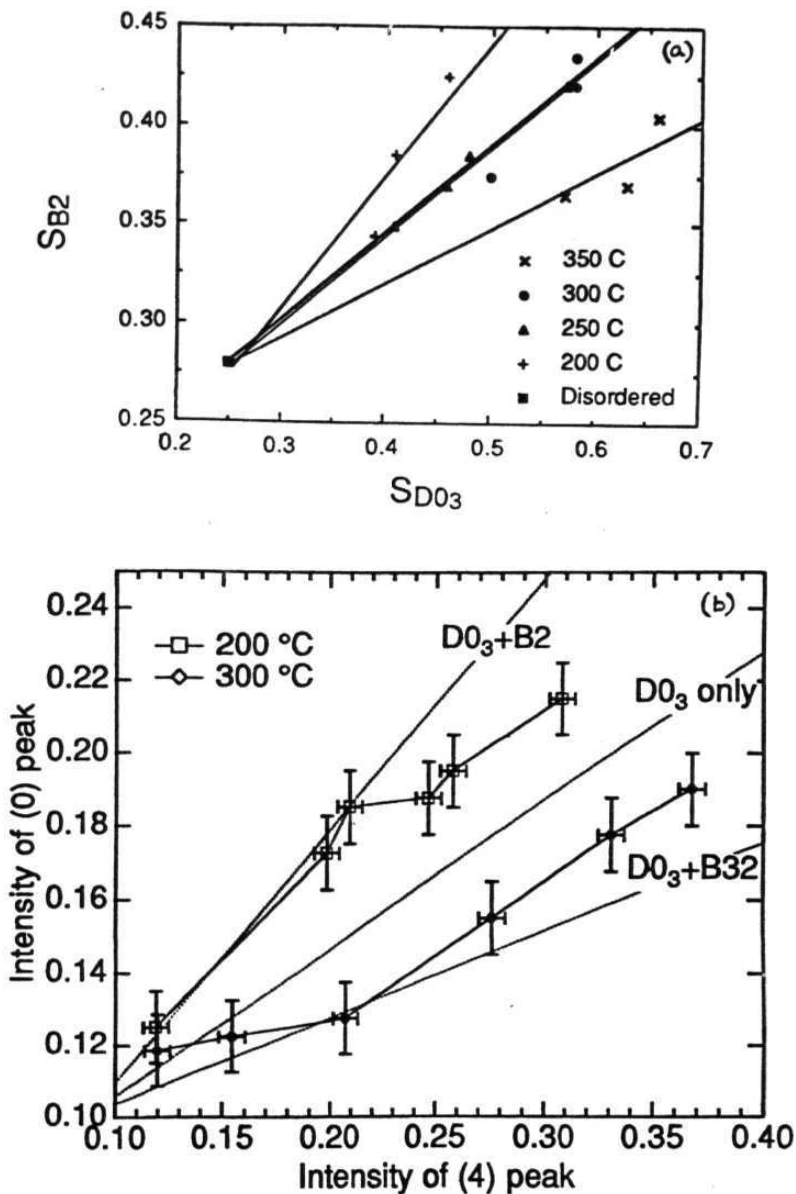


Fig.1.6 a. Kinetic paths of LRO for Fe_3Al as measured using X-ray diffraction [57]. S_{B2} and S_{D0_3} are the order parameters for B2 and $D0_3$ ordered structures.

b. Kinetic paths of short range ordering (SRO) for Fe_3Al using Mössbauer spectroscopy [57]. The intensity of peaks for 4 Al near neighbours and 0 Al neighbours to Fe, were taken as a measure of SRO parameters

has been observed which is termed 're-entrant' **magnetism** which shows characteristics of both spin glass and ferromagnetic behaviour [23]. At high temperature the system is paramagnetic and below a Curie temperature (T_C) the system shows a non-uniform magnetic behaviour. At a still lower temperature, T_{RE} , the system shows irreversibility and loses its magnetisation as it enters a spin glass state.

Several theoretical attempts have been made to understand these alloys, and questions such as whether the reentrant state is a true transition and what is the exact nature of the reentrant state are being extensively discussed [24-27]. The first model due to Sherrington and Kirkpatrick [24] considered **Ising** spins interacting through long-range exchange of random sign and with an overall positive bias. This gave a ferromagnetic phase at T_C and at low temperature a mixed phase with irreversibility. The extension of this model to Heisenberg spins by Gabay and Toulouse [25] showed that at the **ferromagnetic** transition (T_C) there is long-range ferromagnetic order on the longitudinal (Z) direction and this coexists with the random (XY) spin components. This is followed by a transition to mixed phase (M1) in which transverse spin components also freeze in random orientations. At a still lower temperature another mixed phase M2 exists which is characterised by strong irreversibility in magnetisation. Saslow and Parker [26] considered randomly frustrated sites in a square lattice of XY spins. The sequence of phases observed by them were: **paramagnet**; non-uniform **ferromagnet**; **non-collinear** non-uniform **ferromagnet**; reentrant spin glass.

In the phenomenological model of **Kaul** [27] the spin system for $T < T_C$ is considered to be composed of an infinite 3D ferromagnetic matrix with finite spin clusters (consisting of ferromagnet coupled spins) embedded in the ferromagnetic matrix. The spin clusters freeze in random orientations (cluster spin glass) over a wide temperature range without a phase transition at the 're-entrant' temperature.

Ternary alloys of pseudo-binary or quasi-binary type provide systems to study re-entrant behaviour if the magnetic exchange interaction between the added third component and the host binary alloy is different from that which exists between the atoms of the binary system. Similarly if the end members of the binary system have ferromagnetic and antiferromagnetic ordering, the ternary system has mixed exchange interactions which can be varied with alloy composition and provide interesting possibilities of magnetic behaviour. As an example, Mn_3Si is an antiferromagnet with a Neel temperature of 25.8 K [28] whereas Fe_3Si which crystallises in the same structure as Mn_3Si , has a ferromagnetic order with a Curie temperature of 810 K [29]. The ternary system $Fe_3 - Mn_x Si$ shows ferromagnetic behaviour for $x < 0.75$ composition [30] a reentrant spin glass behaviour for $0.75 \leq x < 1.5$ [31] and only a spin glass transition for $x = 1.8$ composition [32]. Chapter 3 of this thesis presents my detailed work on this system with an aim to understand its magnetic properties in the light of existing theoretical models. In the related ternary system $Fe_3 - Mn Al$, the change in magnetic behaviour of Fe_3Al with Mn

addition is also investigated in Chapter 5.

The method of ^{57}Fe **Mössbauer** spectroscopy is well suited to study all the **aspects** of Fe ternary alloys discussed above. Ferromagnetic resonance studies also provide valuable complementary information. In the following sections I therefore discuss briefly the principles of **Mössbauer** Effect [33] and Ferromagnetic resonance [53] and also the parameters of interest which can be obtained using these measurement techniques.

2. **MÖSSBAUER** EFFECT

The emission of a gamma ray photon from a nucleus without loss of energy due to recoil with its natural linewidth and its resonant absorption in an identical nucleus is known as **Mössbauer** effect. Several books and monographs discuss this topic in detail [34-44]. For the sake of completeness a simple introduction is presented. If we consider a nucleus of mass **M** at rest and it emits a gamma ray (i.e. transition from one nuclear energy level to another takes place) the gamma ray loses energy **E_R** due to recoil of the nucleus and the energy of the gamma ray is **E_γ** = **E₀** - **E_R**, where **E₀** is energy difference between the two nuclear levels. The recoil energy **E_R** is given by

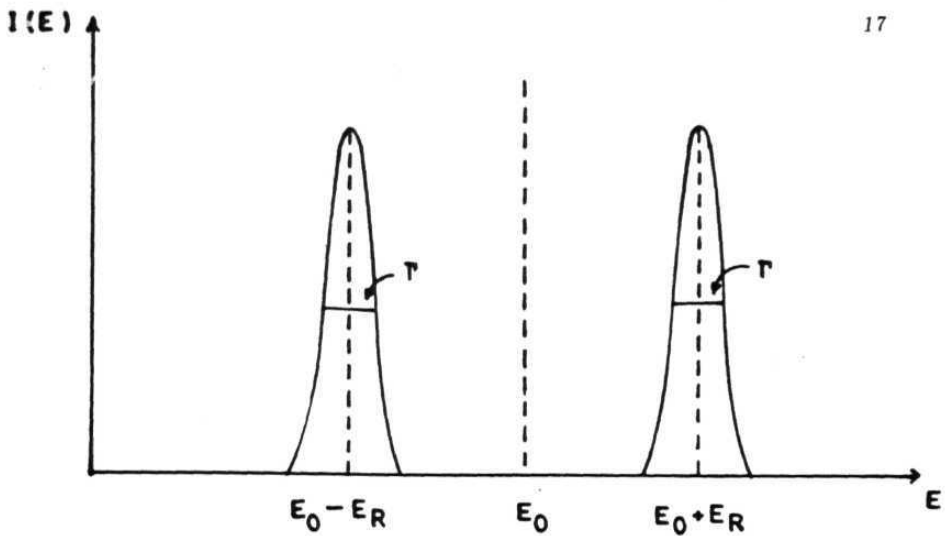
$$E_R = \frac{P_\gamma^2}{2M} = \frac{E_\gamma^2}{2Mc^2} = \frac{(E_0 - E_R)^2}{2Mc^2} \cong \frac{E_0^2}{2Mc^2} \quad (1.1)$$

where **P** is the momentum of the gamma ray photon. If the emitted

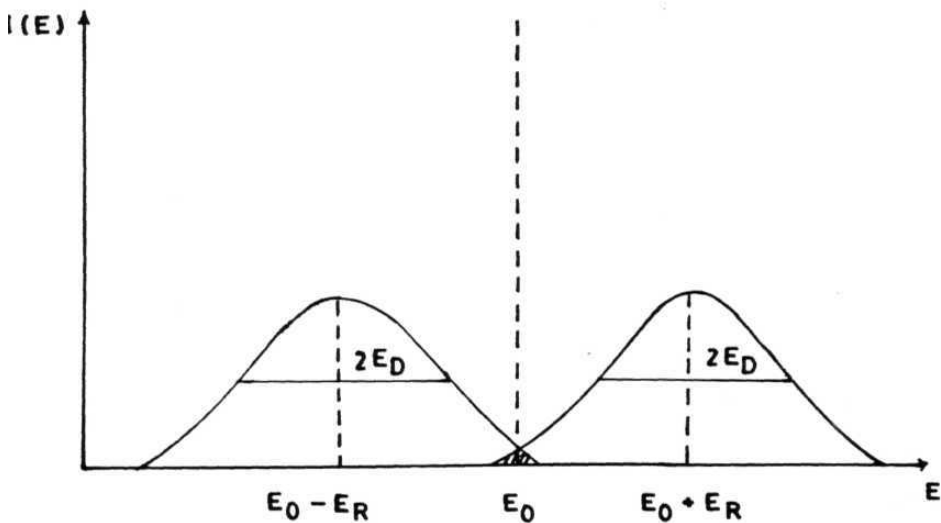
gamma ray photon is to be absorbed by a identical nucleus, the energy required to excite the nucleus would be $E_0 + E_R$. The emission and absorption lines are of Lorentzian shape (Fig.1.7a). The natural linewidth Γ for emission and absorption line is typically of the order of 10^{-7} eV and is very much smaller than the recoil energy E_R (typically of the order of 10^{-9} to 10^{-3} eV). Hence no resonance takes place. At certain temperature T , the emission and absorption lines are broadened because of the thermal motion of the nuclei. This is known as Doppler broadening and emission and absorption lines can overlap to a very small extent at high temperatures (Fig.1.7b). But resonance absorption cannot be observed clearly [35]. The overlapping of emission and absorption lines can be achieved when the nuclei are embedded in a solid lattice. For a typical solid, the threshold displacement energy is of the order of 10-50 eV depending on mass, crystal structure and direction. The recoil energy E_R is much less than the displacement energy and insufficient to displace the atom. E_R is of the order of phonon energies and it can be transferred to the lattice. There is finite probability for zero phonon transitions i.e. emission of γ -ray without excitation of phonons in the lattice. This results in emission of γ -ray with its full energy E_0 and natural linewidth Γ . The fraction of γ -rays emitted without loss of energy is given by recoil-free fraction f as follows [38]:

$$f = \exp \left\{ \frac{-3E_R}{2k_B\theta_D} \left[1 + 4 \left(\frac{T}{\theta_D} \right)^2 \int_0^{\theta_D/T} \frac{x}{e^x - 1} dx \right] \right\}$$

where θ_D is the Debye temperature for the lattice



(a)



(b)

- Fig.1.7** a. γ -ray emission and absorption lines with a shift due to the recoil energy E_R for gamma emission and absorption from a nucleus at rest. E_0 is the transition energy.
- b. Small overlap of emission and absorption lines due to Doppler broadening (E_D) for a gas of atoms at finite

$$\text{For } T \ll \theta_D, f = \exp\left\{\frac{-3E_R}{2k_B\theta_D}\right\} \quad (1.3)$$

$$T > \theta_D, f = \exp\left\{\frac{-6E_R T}{k_B\theta_D^2}\right\} \quad (1.4)$$

The recoil-free fraction f is **large** for low temperatures and small recoil energies, E_D .

In a resonance absorption experiment, an emission line with natural linewidth r is moved over an absorption line with natural linewidth P . This can be achieved by giving t small relative Doppler velocity between source and absorber (Fig. 1.8). The shape of the resulting absorption profile is **Lorentzian** with linewidth 2Γ and the total **cross-section** is given by [34]

$$\sigma = \sigma_0 \frac{\Gamma^2}{\Gamma^2 + 4(E - E_0)^2} \quad (1.5)$$

where $\sigma_0 = 2\pi\lambda^2 \frac{2I_e + 1}{2I_g + 1} \frac{1}{\alpha_t + 1}$ is the maximum cross-section, I and

I are the nuclear spins of excited and ground **states**, $\lambda (\lambda = 2\pi\lambda)$ is the wavelength of the **γ -ray**, α_t is the total internal conversion coefficient (for ^{57}Fe , α_t is of the order of 10). The ratio of the natural linewidth and photon energy ($\Gamma/E = 3 \times 10^{-13}$ for Fe) is a measure of accuracy in the determination of relative energy changes. Because of this **high resolution**, **Mössbauer spectroscopy** has been used extensively in studying extremely small energy changes in the nuclear levels. These are known as hyperfine interactions.

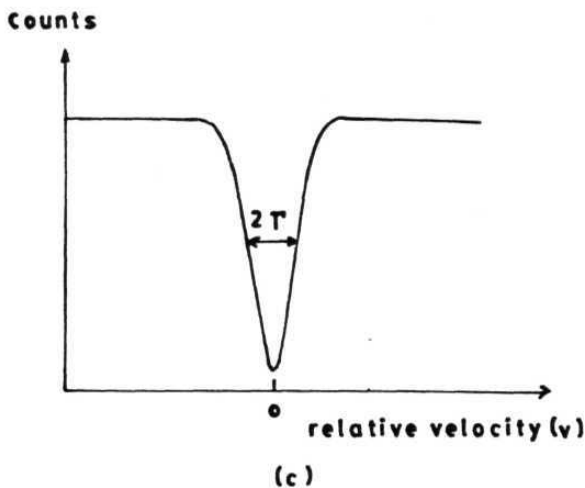
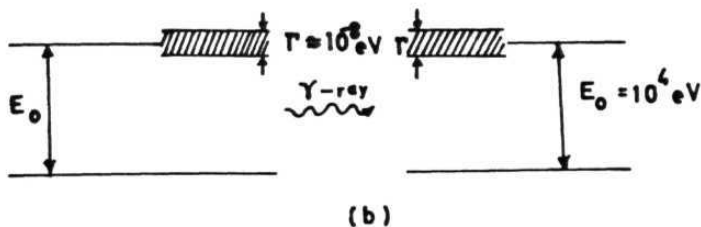
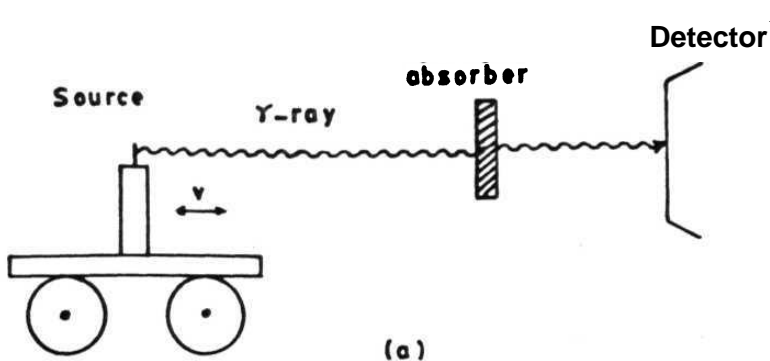


Fig.1.8 a. Schematic diagram of **Mössbauer** experiment.
 b. Schematic representation of resonance emission and absorption of γ -ray.
 c. Typical Mössbauer spectrum which consists of intensity of γ -rays detected by the detector as a function of relative velocity between source and absorber.

2.1. **Hyperfine** Interactions

There are mainly three types of hyperfine **interactions**, which give valuable information about chemical **environment** around the nucleus due to the splitting or shifting of the nuclear energy levels by these interactions: (a) Electric **monopole** interaction or **Isomer** shift which arises due to the Coulomb interaction between the nucleus and the **s-electron** density around the **nucleus**. It is also known as chemical shift, (b) Magnetic Dipole interaction or Nuclear **Zeeman** effect which arises due to the interaction of the nuclear dipole **moment** with the effective magnetic field at the nucleus, (c) Electric quadrupole interaction or quadrupole splitting which arises due to the interaction of nuclear electric quadrupole **moment** with the electric field **gradient** (EFG) around the nucleus. **Mössbauer** spectrum reflects the nature and strength of the hyperfine interactions. All these interactions are discussed in detail below.

2.1.a. Isomer shift

The size of the nucleus in the excited state is different from the size of the nucleus in the ground state.

$$\delta R = R_e - R_g \quad (1.6)$$

where R_e and R_g are radii of the nucleus in the excited and ground states respectively. For ^{57}Fe , δR is negative and is **posi-**

tive for ^{119}Sn . For a nucleus having a finite volume, **s-electrons** around the nucleus have a ability to penetrate into the nucleus and spend a fraction of their **time** inside the nuclear region. Then the nuclear charge interacts electrostatically with the **s-electrons** and the nuclear levels will be shifted by small amount $6E$ (See Fig. 1.9a).

$$\delta E = \int_0^{\infty} \rho_{el} (V_f - V_p) 4\pi r^2 dr$$

where $V(r) = Ze/r$ for $0 < r \leq \infty$ represents the electrostatic potential for a point-charge nucleus at a distance r , and

$$V_f(r) = (Ze/R)[3/2 - (r^2/2R^2)] \quad \text{for } r < R \quad (1.8)$$

$$V_f(r) = Ze/r \quad \text{for } r > R \quad (1.9)$$

represents the electrostatic potential of a nucleus of finite **size**. ρ_e is the electron density at the nucleus and is given in terms of electron wave function ψ by $-e|\psi(0)|$. Then

$$\delta E = (2\pi/5)Ze^2R^2|\psi(0)|^2 \quad (1.10)$$

The nuclear volume will be different in each state of excitation and δE will be different in each nuclear state. When a transition between the excited state and ground state of a nucleus takes **place**, the change in gamma ray energy due to the difference in nuclear energy is

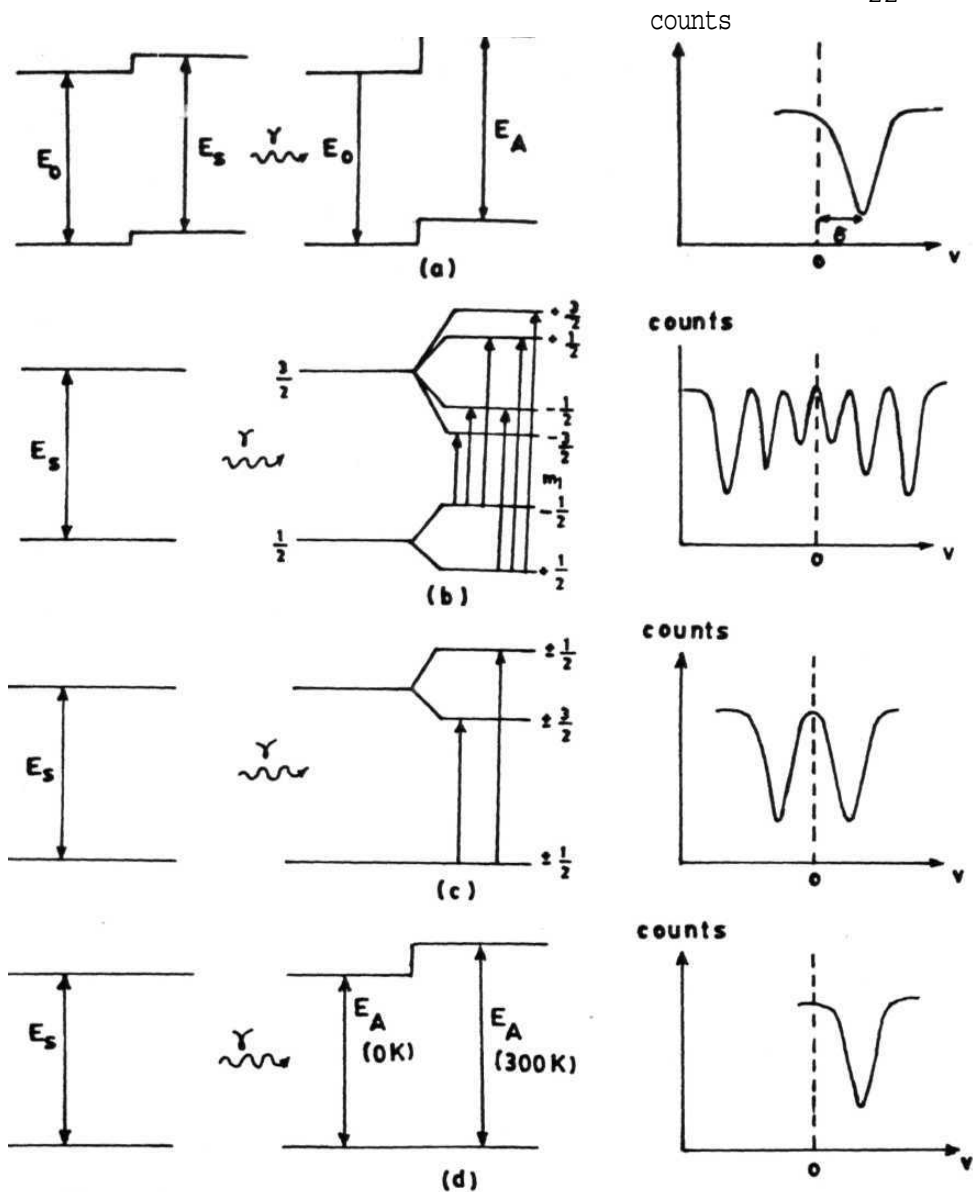


Fig.1.9. Representation of **Isomer** shift (a), **Nuclear Zeeman** Splitting (b), **Quadrupole** splitting (c), **Thermal red** shift (d) and their typical **Mössbauer** spectra. S and A refer to source and absorber respectively.

$$\Delta E = \langle \delta E \rangle_e - \langle \delta E \rangle_g = (2\pi/5) Z e^2 |\psi(0)|^2 (R_e^2 - R_g^2) \quad (1.11)$$

In a Mossbauer experiment, small Doppler velocity is applied to the source(S) or absorber(A) to observe the resonance. So, we observe the difference in **isomer** shift between source and absorber which is given by

$$\delta_{IS} = \Delta E_A - \Delta E_S = (2\pi/5) Z e^2 (R_e^2 - R_g^2) \left[|\psi(0)|_A^2 - |\psi(0)|_S^2 \right] \quad (1.12)$$

There is one more contribution to isomer shift which arises from the many oscillations ($\approx 10^{11}$ /sec) of the vibrating atoms that take place during the life time of the excited nuclear states (10^{-7} - 10^{-8} sec) which is temperature dependent. $\langle v \rangle$ of oscillating atoms causes a shift in resonance line by second-order Doppler effect [44,45]. It is known as temperature shift or thermal red shift (Fig. 1.9d) and is given as

$$\delta_{SOD} = \frac{\langle v^2 \rangle}{2c^2} E_\gamma \quad (1.14)$$

$\langle v^2 \rangle$ is dependent on temperature, pressure, Debye temperature, and lattice defects.

In Mossbauer experiments, generally we use a standard source, then $|\psi(0)|_S^2$ is a constant. If $6R$ is positive, a positive isomer shift indicates an increase in the electron density at the nucleus in going from source to absorber and vice-versa. The isomer shift for a particular absorber will be different relative to different sources or same source in different chemical environ-

ments (For eg. ^{57}Co embedded in Pd, Rh, Pt, Cr or stainless steel matrix) because $|\psi(0)|^2$ changes with the chemical environment around the nucleus. Hence **isomer** shift data are always compared with standard absorber. In Fe **Mössbauer** spectroscopy, metallic iron and Sodium nitroprusside dihydrate $\text{Na}_2[\text{Fe}(\text{CN})_5\text{NO}]\cdot 2\text{H}_2\text{O}$ (SNP) are commonly used as standard absorbers and isomer shift is quoted relative to these standards.

2.1.b. Nuclear Dipole Interaction or Zeeman effect

The nuclear magnetic moment μ_N interacts with the magnetic field H at the nucleus and splits the nuclear level with spin I ($I > 0$) into $2I+1$ sublevels. This interaction is described by the **Hamiltonian**

$$H = -g_N \mu_N I \cdot H \quad (1.15)$$

where g_N is the nuclear **Lande** splitting factor and $\mu_N = eh/2Mc$, is the nuclear **magneton**. M is the mass of the nucleus. The eigen values of the Hamiltonian are

$$E_m = -g_N \mu_N H m_I$$

where $m_I = I, I-1, \dots, -I$, is the nuclear magnetic quantum number. For **example**, in the case of Fe, the ground state $I = 1/2$ splits into 2 sublevels ($m_I = \pm 1/2$) and first excited state $I = 3/2$ splits into 4 sublevels ($m_I = \pm 3/2, \pm 1/2$) and the splitting of energy levels is shown in Fig. 1.9b. The transitions bet-

ween various levels are governed by the selection rules $\Delta m = 0, \pm 1$. The intensities of six **Zeeman** transitions are dependent on the angle θ between the direction of the magnetic field at the nucleus and the direction of γ -ray [41]. The angular dependence of the allowed transitions are given as $(\pm 3/2 \rightarrow \pm 1/2, \Delta m = \pm 1): 9/4(1+\cos^2\theta)$, $(\pm 1/2 \rightarrow \pm 1/2, \Delta m = 0): 3\sin^2\theta$, $(\pm 1/2 \rightarrow \pm 3/2, \Delta m = \pm 1): 3/4(1+\cos^2\theta)$. The intensity ratios for the six transitions can be written as $3:x:1::1:x:3$ where $x = 4\sin^2\theta/(1+\cos^2\theta)$. When the magnetic field at the nucleus is along the direction of γ -emission ($\theta = 0^\circ$), the intensity ratios are $3:0:1::1:0:3$. When the magnetic field is perpendicular to γ -emission ($\theta = 90^\circ$) and the intensity ratios are $3:4:1::1:4:3$. For a polycrystalline absorber free of texture and without an external magnetic field, the angular dependence can be integrated over all directions which gives average value and the intensity ratios are given by $3:2:1::1:2:3$.

The field H acting at the nuclear site in Eq. 1.15 is called the magnetic hyperfine field when it arises from the electrons around the **Mössbauer** nucleus. This can consist in general of several contributions each of a different magnitude. These contributions are [46]

$$H = H_{\text{core}} + H_{\text{cond}} + H_{\text{ov}} + H_{\text{orb}} + H_{\text{mag}} + H_{\text{dip}} \quad (1.17)$$

in decreasing order of magnitude. The first three contributions (we consider the typical case of Fe and its alloys) are proportional to difference in the number of spin up and spin down **electrons** at the ^{57}Fe nucleus (unpaired electron spin density or spin

polarisation) and arise from the Fermi Contact interaction [47]. Other three terms have their origin in classical magnetics and atomic physics.

H_{core}: The core polarisation term is the most dominant one and refers to the spin polarisation of the core 1s, 2s, 3s and relativistic 2p electrons around the ⁵⁷Fe nucleus and this generates a hyperfine field because these electrons have a finite probability of overlap with the nucleus. Changes in core polarisation in metals and alloys are induced by changes in number of unpaired d electrons of the Fe atom, which in turn exchange polarise the core electrons.

H_{cond}: The spin polarisation of the 4s conduction electrons is called conduction electron polarisation. A solute atom in an alloy causes a disturbance in local spin or charge density and this is transmitted to the ⁵⁷Fe nucleus through an exchange polarisation of the 4s conduction electrons [48].

H : An overlap of the Fe atom wave function with those of solute atoms also causes a change in hyperfine field because one has to orthogonalise the wave function of 3d and 3d↓ electrons with the solute atom wave function and this contribution tends to show a dependence in the solute size.

H_{orb} : Fe atoms retain some free atom character and orbital moment in bcc iron and its alloy and a spin-orbit interaction between the nuclear spin and orbital angular momentum of the 3d electrons gives this hyperfine field contribution [49].

H_{mag} : This contribution includes the demagnetisation field which

depends on sample **geometry**, and Lorentz field.

H_{dip} : The **magnetic** dipole moments at neighbouring sites of Fe give this magnetic dipole field contribution which vanishes for cubic symmetry of the lattice for pure Fe but does exist when a solute of different magnetic moment substitutes a neighbouring site. However this contribution is extremely small.

The sign of the hyperfine magnetic field at the nucleus relative to the **ap**plied external field can be determined. The field at nucleus will increase or decrease depending on whether the external field is applied parallel or **antiparallel** to the hyperfine field [50]. For this study large external fields (typically 20 - 50 kOe) are required and these fields can be obtained using superconducting magnets. The sign of hyperfine field for **α -Fe** is negative.

2.1.c. Electric Quadrupole Interaction

Any nucleus with a spin greater than $I = 1/2$ has a non-spherical charge distribution. The deviation from spherical symmetry is different in each state of excitation. A measure of the deviation from spherical symmetry is given by electric quadrupole moment **eQ** which is a tensor **quantity**,

$$eQ = \int r^2 (3\cos^2\theta - 1) dT \quad (1.18)$$

where e is the charge of the proton, P is the charge density in a

volume **element** $d\tau$ at a distance r from the centre of the nucleus and **makes** an angle θ with the nuclear spin quantisation axis. The sign of Q represents the shape of the distorted nucleus. Q is negative for flattened nucleus and positive for elongated nucleus. The electric quadrupole moment eQ can interact **with** an inhomogeneous electric field known as electric field gradient (EFG) at the nucleus. The **Hamiltonian** is given by [38]

$$H = \frac{eQV_{33}}{4I(2I-1)} \left[3\hat{I}_3^2 - I(I+1) + \eta (\hat{I}_1^2 - \hat{I}_2^2) \right] \quad (1.19)$$

where I is the nuclear spin, I_1 , I_2 and I_3 are spin **operators**. η is the asymmetry parameter given by

$$\eta = \frac{V_{11} - V_{22}}{V_{33}} \quad (1.20)$$

where $V_{i,j} = \frac{\partial^2 V}{\partial x_i \partial x_j}$ ($i, j = 1, 2, 3$) and V is the electrostatic potential at the nucleus. The electric field gradient has been **specified** in terms of only two **independent** parameters η (**defined** above) and V_{33} (usually written as $-eq$), because it is possible to find a principal axis such that the off-diagonal elements vanish. Out of the three diagonal elements, one is further reduced because V satisfies the **Laplace** equation

$$V_{11} + V_{22} + V_{33} = 0 \quad (1.21)$$

The diagonal elements are ordered as

$$|v_{33}| \geq |v_{22}| \geq |v_{11}| \quad (1.22)$$

giving $0 < \eta < 1$.

The **eigen** values of the **Hamiltonian** are

$$E_Q = \frac{e^2 q Q}{4I(2I-1)} \left[3m_I^2 - I(I+1) \right] \left(1 + \frac{\eta^2}{3} \right)^{1/2} \quad (1.23)$$

where $m_I = I, I-1, \dots, -I$ is the nuclear spin **quantum** number. A nuclear level with spin I splits in to $(2I+1)/2$ sub-levels. For ^{57}Fe , the quadrupole splitting of $I = 3/2$ level is shown in Fig. 1.9c. The Mossbauer spectrum contains two absorption lines with equal intensity.

The EFG at the nucleus arises **from** the charges on the ions surrounding the nucleus and from **el.ctrons** of unfilled shells.

2.1.d. Contributions to EFG

- (1) **Ligand** or lattice contribution: The charges on distant atoms or ions surrounding the Mossbauer nucleus **in** non-cubic symmetry gives a contribution to EFG, known as Ligand or lattice **contribution**.
- (2) Valence electron contribution: This contribution is from non-cubic electron distribution in partially filled valence **orbitals** of the Mossbauer atom.

The EFG elements can be expressed in terms of the spherical polar coordinates $x = r \sin\theta \cos\phi$, $y = r \sin\theta \sin\phi$ and $z = r \cos\theta$. If the distances r . and angles θ . and ϕ . of all n ions with res-

pect to the **Mössbauer** atoms are known from crystal **structure**, and effective charges q_i assigned to the **ions**, then the lattice contributions to V_{33} and η can be written as

$$V_{33} = \sum_i^n q_i r_i^{-3} (3 \cos^2 \theta_i - 1) \quad (1.24)$$

$$\text{and } \eta_L = 1/(V_{33})_L \sum_i^n q_i r_i^{-3} 3 \sin^2 \theta_i \cos 2\phi_i \quad (1.25)$$

This interaction between the ligands and the quadrupole moment of the **Mössbauer** nucleus is complicated by the presence of the electronic cloud belonging to the **Mössbauer** atom. Sternheimer [51] has shown that, for relatively large atoms, this cloud distorts the quadrupole interaction in such way as to **amplify** the interaction. This phenomenon is known as "Sternheimer antishielding" and is corrected for by multiplying $(V_{33})_I$ by the factor $(1 - \gamma_\infty)$ where γ_∞ is called the Sternheimer antishielding **factor**. For Fe^{3+} compounds $(1 - \gamma_\infty)$ is estimated to be of the order of 10 and in general depends on the number of 3d electrons in the ion [52].

The valence electron contribution to V_{33} can be evaluated by taking the expectation value of the quantity $-e(3\cos^2\theta - 1)r^{-3}$ for each electron in the valence orbital state $|l.m.\rangle$ and summing over all valence electrons:

$$(V_{33})_{\text{val}} = -e \sum_i \langle l_i m_i | 3\cos^2\theta - 1 | l_i m_i \rangle \langle r_i^{-3} \rangle \quad (1.26)$$

Due to the screening of the valence electrons from the nucleus by inner shell electrons, the value of $\langle V_{33} \rangle$, given by Eq. (1.26) will not be the actual valence contribution to the EFG at the nuclear site. **Sternheimer** has corrected $\langle V_{33} \rangle_{\text{val}}$ by multiplying it by $(1 - R)$. The Sternheimer shielding factor R has been estimated to be 0.2 - 0.3 for iron and tin.

3. FERROMAGNETIC RESONANCE

The **phenomenon** of **ferromagnetic resonance (FMR)** was first discovered by Griffiths [53]. The resonant absorption of external microwave field in ferromagnetic materials is called "Ferromagnetic resonance". When an electron, which acts like a **magnetic dipole**, is placed in a uniform static magnetic field H , the **magnetic moment** of the electron precesses about the axis of the magnetic field H with the **Larmor frequency**

$$\omega_L = \gamma H \quad (1.27)$$

where $r = \hbar \gamma / \omega$ is the **gyromagnetic ratio**, is the ratio of the magnetic moment to the angular momentum. When the external microwave field with a frequency $\omega = \omega_L$ is applied perpendicular to the static magnetic field H , the microwave power is absorbed by the magnetic dipole, i.e. transition from **ground level** to higher energy level takes place. The resonance condition is

$$\hbar \omega = g \mu_B H \quad (1.28)$$

This phenomenon is known as electron spin resonance (ESR). This technique is valid for the substances having unpaired electrons and their spins are non interacting. In the case of ferromagnetic materials, the spins are coupled with each other through strong exchange interactions and give rise to large resultant magnetisation. This magnetisation \vec{M} precesses about the axis of an effective magnetic field H_{eff} , which takes into account the demagnetisation and anisotropy fields in addition to the external field. For the experimental convenience the microwave frequency ω is kept fixed and magnetic field H is scanned to observe the resonance.

In ferromagnetic materials, the Landau-Lifshitz-Gilbert (LLG) equation of motion for magnetisation \vec{M} is [54]

$$\frac{d\vec{M}}{dt} = -\gamma(\vec{M} \times \vec{H}_{eff}) + \frac{\lambda}{\gamma M_S^2} \left(\vec{M} \times \frac{d\vec{M}}{dt} \right) \quad (1.29)$$

In Eq. (1.29), the first term is the torque experienced by the magnetisation vector and second term is the damping term. M_S is the saturation magnetisation and λ is the Gilbert damping parameter. The effective magnetic field, $H_{eff} = H + \vec{h}(t) - H_{dem} + H_K$, where H is the homogeneous static magnetic field, $\vec{h}(t)$ is the weak alternating magnetic field which arises from microwave field, H_{dem} is the demagnetising field and H_K is the anisotropy field. In Eq. (1.29) the exchange term $(2A\gamma/\hbar^2)(\vec{M} \times \nabla^2 \vec{M})$ is neglected because its contribution to linewidth and resonance fields

is very small.

By solving Eq. (1.29), the resonance conditions for a rectangular **sample** in horizontal-parallel ($||$) and vertical-parallel ($||^v$) geometries have been calculated [55]. In horizontal-parallel sample geometry, the static external **magnetic** field H is applied along the length of the sample (along the symmetry **axis**, i.e. z-axis), and the resonance condition is

$$\left[\left(\frac{\omega}{\gamma} \right)^2 + \Gamma_{||h}^2 \right] = \left[H_{res}^{||h} + 4\pi M_S + H_k \right] \left[H_{res}^{||h} + H_k \right] \quad (1.30)$$

where $\Gamma = \frac{\Delta H}{1.45}$. In vertical-parallel sample geometry, the **magnetic** field H is applied along the breadth of the sample. The **magnetic** field H and **symmetry axis** (**z-axis**) lie in the sample plane. The resonance condition is

$$\left[\left(\frac{\omega}{\gamma} \right)^2 + \Gamma_{||v}^2 \right] = \left[H_{res}^{||v} + 4\pi M_S - H_k \right] \left[H_{res}^{||v} - H_k \right]$$

Since the linewidth parameter r is independent of H_k and ω is kept fixed in these experiments, the left hand side of Eqs. (1.30) and (1.31) have the same values regardless of the magnitude of H_k .

To calculate the value of H_k from Eqs. (1.30) and (1.31),

first it is assumed that $H_k = 0$, then Eqs. (1.30) and (1.31) becomes

$$(H_{\text{res}}^{\parallel} + 4\pi M_S) H_{\text{res}}^{\parallel} = (H_{\text{res}}^{\parallel h} + 4\pi M_S + H_k) (H_{\text{res}}^{\parallel h} + H_k) \quad (1.32)$$

and

$$(H_{\text{res}}^{\parallel} + 4\pi M_S) H_{\text{res}}^{\parallel} \simeq (H_{\text{res}}^{\parallel v} + 4\pi M_S - H_k) (H_{\text{res}}^{\parallel v} - H_k) \quad (1.33)$$

where H_{res} is the resonance field in the absence of H_k . These Eqs. (1.32) and (1.33) can be satisfied only when

$$H_{\text{res}}^{\parallel} = H_{\text{res}}^{\parallel h} + H_k \quad (1.34)$$

$$\text{and } H_{\text{res}}^{\parallel} = H_{\text{res}}^{\parallel v} - H_k \quad (1.35)$$

$$\text{Then } H_k = (H_{\text{res}}^{\parallel v} - H_{\text{res}}^{\parallel h})/2 \quad (1.36)$$

Once H_{res} value is known, $4\pi M_S$ value can be calculated from Eq. (1.30),

$$4\pi M_S = \frac{\left(\frac{\omega}{\gamma}\right)^2 + \Gamma_{\parallel h}^2}{H_{\text{res}}^{\parallel h} + H_k} - (H_{\text{res}}^{\parallel h} + H_k)$$

The accurate values of resonance field, H_{res} , saturation magnetisation M_S and Lande splitting factor g can be calculated

by fitting **FMR** spectra using a non-linear least squares fit program to the expression [55] for the parallel geometry

$$\frac{dP_{||}}{dH} \propto \frac{d}{dH} \left[(\mu'^2 + \mu''^2)^{1/2} + \mu'' \right]^{1/2} \quad (1.38)$$

with the μ' and μ'' are the real and imaginary components of the dynamic permeability given by,

$$\mu' = \frac{[(H+H_k)(B+H_k)-\Gamma^2-(\omega/\gamma)^2][(B+H_k)^2-\Gamma^2-(\omega/\gamma)^2] + 2\Gamma^2(B+H_k)(B+H+2H_k)}{[(H+H_k)(B+H_k)-\Gamma^2-(\omega/\gamma)^2]^2 + \Gamma^2(B+H+2H_k)^2} \quad (1.39a)$$

and

$$\mu'' = \frac{-2\Gamma(B+H_k)[(H+H_k)(B+H_k)-\Gamma^2-(\omega/\gamma)^2] + \Gamma(B+H+2H_k)[(B+H_k)^2-\Gamma^2-(\omega/\gamma)^2]}{[(H+H_k)(B+H_k)-\Gamma^2-(\omega/\gamma)^2]^2 + \Gamma^2(B+H+2H_k)^2} \quad \dots (1.39b)$$

where $B = H + 4\pi M_c$, H_c is the 'in-plane' uniaxial anisotropy field, $\nu = \omega/2\pi$ is the frequency of the microwave field, $r = \lambda\omega/\gamma^2 M_S$ is the linewidth parameter and X is the Gilbert damping parameter. Lande splitting factor g and $4\pi M_S$ are the free fitting parameters.

The **FMR** linewidth ΔH depends on the frequency ω of the microwave field and increases as ω increases. The inhomogeneities, porosity and defects also give contribution to linewidth. The resonance field, H_{res} , depends on the saturation magnetisation

tion M_g , sample shape and domain structure [56]. A derivative power absorption spectrum is shown in Fig. 1.10. with the definition of linewidth and resonance field. Experimental details of **FMR** measurements are given briefly in Chapter 2 and work based on these measurements is presented in Chapter 3.

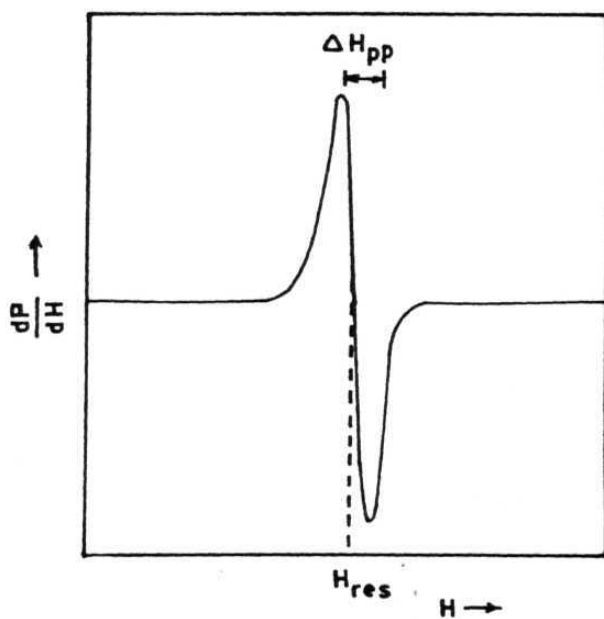


Fig.1.10. Typical **FMR** first derivative (dP/dH) absorption spectrum. ΔH_{pp} is the peak-to-peak linewidth and H_{res} is the resonance field.

REFERENCES

- [1] "Ternary Alloys: A comprehensive compendium of Evaluated constitutional Data and Phase Diagrams", edited by G. Petzow and G. Effenberg (**Wienheim**, New York, 1992).
- [2] "Phase Equilibria in Iron Ternary **Alloys**", Vol.4, G.V. **Raynor** and V.G. Rivlin (Institute of Metals, London, 1988).
- [3] "Ternary Equilibrium **Diagrams**", D.R.F. **West** (Chapman and Hall, London, 1982).
- [4] B.Fultz, J. Mater. Res. 7, **946(1992)**.
- [5] Syo **Matsumara**, T. Furuse and K. Oki, in "Diffusion in Ordered Alloys", edited by B. **Fultz**, R.W. Cahn and D. Gupta (TMS Proceedings of Symposium on Diffusion in Ordered Alloys and **Intermetallic Compounds**,1992).
- [6] O. **Beckman** and L. Lundgren, Compounds of Transition Elements with **Nonmetals**, in "Hand Book of Magnetic Materials", Vol.6, edited by K.H.J. Euschow (Elsevier, Amsterdam, 1991).
- [7] L. **Häggström**, J.Sjöström, A. **Narayanasamy** and F.R. Verma, Hyperfine **Interactions**,**23**, 109 (1985).
- [8] D.J. Chakrabarti, Metall. **Trans.B8**, 121 (1977).
- [9] "Ordering and Disordering in alloys", edited by A.R. Yavari (Elsevier, New York, 1992).
- [10] "Theory of Structural Transformations in **Solids**", A. **Khachaturyan** (John Wiley, New York, 1983).
- [11] P. Cenedese, F. **Bley** and S. Lefebise, Acta **Cryst.A40**, 228 (1984).

- [12] S. Hashimoto and H. Iwasaki, Radiation Effects and Defects in Solids, **124**, 147 (1992).
- [13] V. **Niculescu** and J.I. Budnick, Solid State Communications, 24, 631 (1977).
- [14] G. Athanassiadis, G. *he* Caer, J. Foot and **L. Rinlinger**, Phys. Stat. Sol.(a), 40, 425, (1977).
- [15] B. **Fultz**, H.H. **Hamdeh** and D.H. Pearson, Acta metall. 37, 2841 (1989), *ibid*; B. Fultz, Acta metall. 37, **823** (1989).
- [16] T.V.S.M. Mohan Babu and C. Bansal, **AIP** Proceedings, **286**, 294 (1992-93).
- [17] T.V.S.M. Mohan Babu and C. Bansal, A **Mössbauer** Effect Study of Chemical and Magnetic order in **Fe_{0.75} Mn Al_{0.25}** alloy system and Disorder-Order Kinetics in **Fe_{0.45}Mn_{0.3}Al_{0.25}**, **Physic: Status Solidi** (Submitted, **1995**).
- [18] H. Sato, K. **Gschwend** and R. Kikuchi, J. Physique **C7**, 357 (1977).
- [19] H. Sato and R. Kikuchi, Acta metall. 24, 797 (**1976**).
- [20] L. Anthony and B. Fultz, J. Mater. Res. 4, 1132 (1989).
- [21] **Z.C.** Gao and B. Fultz, Phil. Mag. B67, 787 (1993).
- [22] G.J. Nieuwenhuys, **B.H. Verbeck** and J.A. Mydosh, J. **Appl.** Phys. 50, 1685 (1979).
- [23] **I.A.** Campbell and S. Senoussi, Phil. Mag. B65, 1267 (1992).
- [24] D. Sherrington and S. Kirpatrick, Phys. Rev. Lett. 35, **1782** (1975).
- [25] M. Gabay and G. Toulouse, Phys. Rev. Lett. 47, 201 (1981).
- [26] **W.M.** Saslow and G. Parker, Phys. Rev. Lett. 56, 1074 (1986).
- [27] **S.N. Kaul**, J. Magn. Magn. Mater. 53, 5 (1985).

- [28] S. **Tomiyoshi** and H. **Watanabe**, J. Phys. **Soc. Japan.** 39, 295 (1975).
- [29] P. **Lecoq** and A. Michel, **Compt. Rend.** **258**, 1817 (1964).
- [30] S. Yoon and J.G. Booth, J. Phys. **F7**, 1079 (1977).
- [31] T.V.S.M. Mohan Babu, C. Bansal and S.N. **Kaul**, J. **Magn. Magn. Mater.** **140** - 144, 127, (1995).
- [32] A. Chakravarti, R. Ranganathan and S. Chatterjee, J. **Magn. Magn. Mater.** **138**, 329 (1994).
- [33] R.L. Mossbauer, Z. Physik 151, 124 (1958).
- [34] "**Mössbauer** Spectroscopy", edited by G. Gonser (Topics in Applied Physics, Vol.5, Springer Verlag, 1975).
- [35] "Introduction to Mossbauer Effect", edited by L. May (Plenum Press, New York, 1971).
- [36] "**Mössbauer** Effect - Principles and Applications", edited by **G.K. Wertheim** (Academic Press, New York, 1964).
- [37] "Chemical Applications of Mossbauer Spectroscopy", edited by V.I. Goldanskii and R.H. Herber (Academic Press, New York, 1968).
- [38] "Mossbauer Spectroscopy", edited by **N.N. Greenwood** and **T.C. Gibb** (Chapman and **Hell**, London, 1971).
- [40] "Applications **of** Mossbauer Spectroscopy", edited by R.L. Cohen (Vol.1, Academic Press, **1976**).
- [41] "Mössbauer Effect and its applications" edited by V.G. Bhide (TMH, 1974).
- [42] "Mössbauer Effect Methodology", edited by R.J. **Gruverman** (Vol. 1 - 11, Plenum Press, New York, 1965-1976).

- [43] **L.R. Walker, G.K. Wertheim** and **V. Jaccarino**, Phys. Rev. Lett. 6, 98 (1961).
- [44]** **R.V. Pound** and **G.A. Rebka Jr.**, Phys. Rev. Lett. 4, 274 (1960).
- [45] **B.D. Josephson**, Phys. Rev. Lett. **4**, 341 (1960).
- [46] **B. Fultz** in "**Mössbauer Spectroscopy Applied to Magnetism and Material Science**", edited by **Gary J. Long** and **F. Grandjean** (Vol.1, Plenum Press, New York, 1993).
- [47] **E. Ferni**, Z. Phys. 82, 729 (1933).
- [48]** **M.B. Stearns** and **J.M. Norbeck**, Phys. Rev. B20, 3739 (1979).
- [49] **W. Marshall** and **C.E. Johnson**, J. Phys. Radium 23, 773 (1962).
- [50] **S.S. Hanna**, **J. Heberle**, **G.J. Perlow**, **D.H. Vincent**, Phys. Rev. Lett. 4, 113 (1960).
- [51] **P.M. Sternheimer**, Phys. Rev. 80, 102 (1950); 84, 244 (1951); 130, 1423 (1963); **H.M. Foley**, **R.M. Sternheimer** and **D. Tycko**, Phys. Rev. **93**, 734 (1954); **R.M. Sternheimer** and **K.M. Foley**, Phys. Rev. **93** 95 (1954).
- [52] **K.D. Sen** and **P.C. Schmidt**, Phys. Rev. A23, 1026 (1981).
- [53] **J.H.E. Griffiths**, Nature, 150, 670 (1946).
- [54] "**Ferromagnetic resonance**", edited by **S.V. Vonsovskii** (**Pergamonpress**, London, 1966).
- [55] **S.N. Kaul** and **V. Siruguri**, J. Phys.: Condens. Matter 4, 505 (1992).
- [56]** **T.V.S.M. Mohan Babu**, M.Phil. Thesis, University of Hyderabad, India (Unpublished, 1988).

- [57] Z.Q. Gao, Ph.D. Thesis, California Institute of Technology, USA (Unpublished, 1994).
- [58] T.V.S.M. Mohan Babu and C. Bansal, Phys. Stat. Sol (b) **190**, 479 (1993).
- [59] D.H. Jack and **R.W.K. Honeycombe**, Acta **metall.** **20**, 787 (1972).

CHAPTER 2

EXPERIMENTAL TECHNIQUES

This chapter describes the experimental methodology of **Mössbauer** spectroscopy, Ferromagnetic resonance, and AC susceptibility measurements and the specific instruments employed to investigate the alloy systems using these techniques. Data analysis procedures for **Mössbauer** spectra are described in detail. The method of alloy preparation, heat treatments and characterisation are also given briefly.

2.1. **MOSSBAUER** SPECTROMETER

The **Mössbauer** spectra are recorded on a μP based **Mössbauer** spectrometer [1] in the standard transmission geometry in zero external magnetic field. The spectrometer operated in constant acceleration mode. A ^{57}Co in **Rh** matrix source is used. The block diagram of the spectrometer is shown in Fig. 2.1. It consists of the following basic blocks:

- a. Velocity Drive and Feedback System
- b. Gamma Ray Detection System
- c. μP based Data Acquisition System

These three blocks are described in detail as follows:

2.1.a. Velocity Drive and Feedback System

The velocity drive is an electromechanical transducer (Nuclear Electronics, Hyderabad) and is based on **Kankaleit** design [2]. The drive consists of a coil (**energising** coil) connected to a rod on which the radioactive source is mounted. An electronic

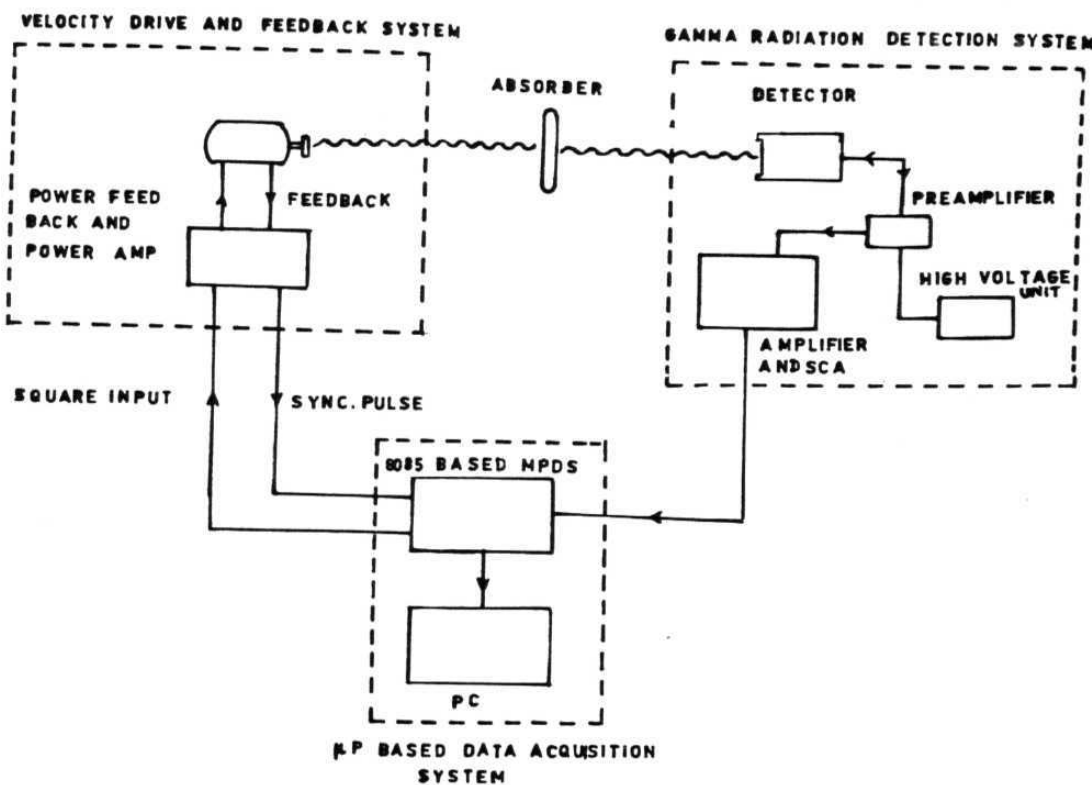


Fig.2.1. Block diagram of Mössbauer Spectrometer,

circuit generates triangular wave form from a square wave fed to it from multi-channel scalar(MCS). This coil carries the driving signal in a magnetic **field**, provided by the permanent magnets fixed in the **drive**. The rod is held with a spring to the body of the transducer on either side. The movement of the coil does not duplicate the driving signal due to the complicated response of the transducer. A pick-up coil is also connected rigidly to the rod. When the transducer moves, there is a change in the flux and produces an induced **emf**. This induced **emf** is proportional to the velocity of the drive. In other words the voltage in the pick-up coil gives a scaled replica of the velocity. This voltage is taken to the error stage of the feed back and power amplifier and is compared with a standard velocity wave form. The feedback loop set-up adjusts in such a way that the difference between the pick-up **signal** and reference signal is zero. A constant acceleration mode is used in which velocity wave form is either triangular or sawtooth.

2.1.b. Gamma Ray Detection System

To detect the gamma rays which are **transmitted** from the sample, a gas filled proportional counter (Ranger Scientific, Inc., USA, Model **PA-800**) is used. This has a gas filling of **97% Xenon - 3% CO₂** at 2 **atm.** pressure and a Beryllium entrance window of 0.01 inch thickness. The detector bias required is in the Kilo-volt range with small current capacity (**$\leq 1 \text{ mA}$**). A high voltage power supply (**ECIL**, India, Model HV 4286A) which operates in Kilo-volt range is used. The proportional counter has a very

high impedance (in **Mega-Ohms**). The input **impedance** of the **spectroscopy amplifier (ECIL, India, Model PA572)** is low and result in a drop in voltage at the input of the amplifier if the counter and amplifier are **connected** directly. To match the impedance, a preamplifier (EG&G **ORTLC**, USA, Model 142 PC) with low output impedance and high input impedance whose gain is of the order of unity is used. The spectroscopy amplifier amplifies the output of the preamplifier to a few volts. Wave shaping is also carried out at this stage. The output of the amplifier is given to single channel analyser (**ECIL**, India, Model SC 604). The single channel analyser is an energy **discriminator** i.e., it rejects all pulses which are outside the extremities of the set energy window. For **Fe Mössbauer** experiments we use 14.4 keV radiation of **⁵⁷Fe**. We have used single channel analyser window to cut the other X-rays and **gamma** rays so that signal-to-noise ratio can be improved. A pulse height spectrum is first recorded and the appropriate gamma energy (14.4 keV) is chosen by setting the window (setting lower level discriminator and upper level discriminator) of the single channel analyser.

2.1.c. μP based Data Acquisition System

The input to the data acquisition system is in the form of standard pulses which are generated at the output of the single channel analyser. The number of these pulses are a function of drive velocity and these can be stored in a conventional **multi-channel analyser (MCA)**, which works in the time mode or **multi-channel scaling (MCS)** mode. The MCS is a mode in which the counts

are stored at different times in different memory locations. **Here**, times means the times at which the drive remains between two velocities v and $v+dv$. The velocity of the drive is divided into small intervals of times (memory locations or channels) in which the counts are stored. Usually the number of channels are 256, 512 or 1024. We have chosen a 1024 channel spectrum (512+512) to record **Mössbauer** data using a home built data acquisition system based on a 8085 Intel microprocessor [1]. The important feature of this system is its low dead **time** (0.15 μ sec per channel). Dead time is the time required by the processor to get data from the buffer counter, to transfer it to the memory and then clear the buffer counter for fresh counts. A low dead time has been achieved by implementing the flow chart of Fig. 2.2 using the 8085 microprocessor. In this **algorithm** the 8253 counter of the microprocessor is loaded with a number. It is down counted at every input pulse from the detector. The difference in counts between the beginning and end of dwell time is the number of counts accumulated in that time. The counter is read at the beginning and end of dwell time very quickly (in half a clock pulse of **the** microprocessor) without resetting it by using "on the fly" instruction. The down counting goes on during the next dwell time but meanwhile the difference in counts accumulated in the previous dwell time is put in the appropriate memory location. Thus a very low dead time is achieved. Data is transferred to the PC through **RS 232** in the asynchronous mode. The data received at the PC is stored in an ASCII file after converting **the** hexadecimal values to decimal. The program to run the spectrometer, to collect and transfer data has been loaded on the EPROM.

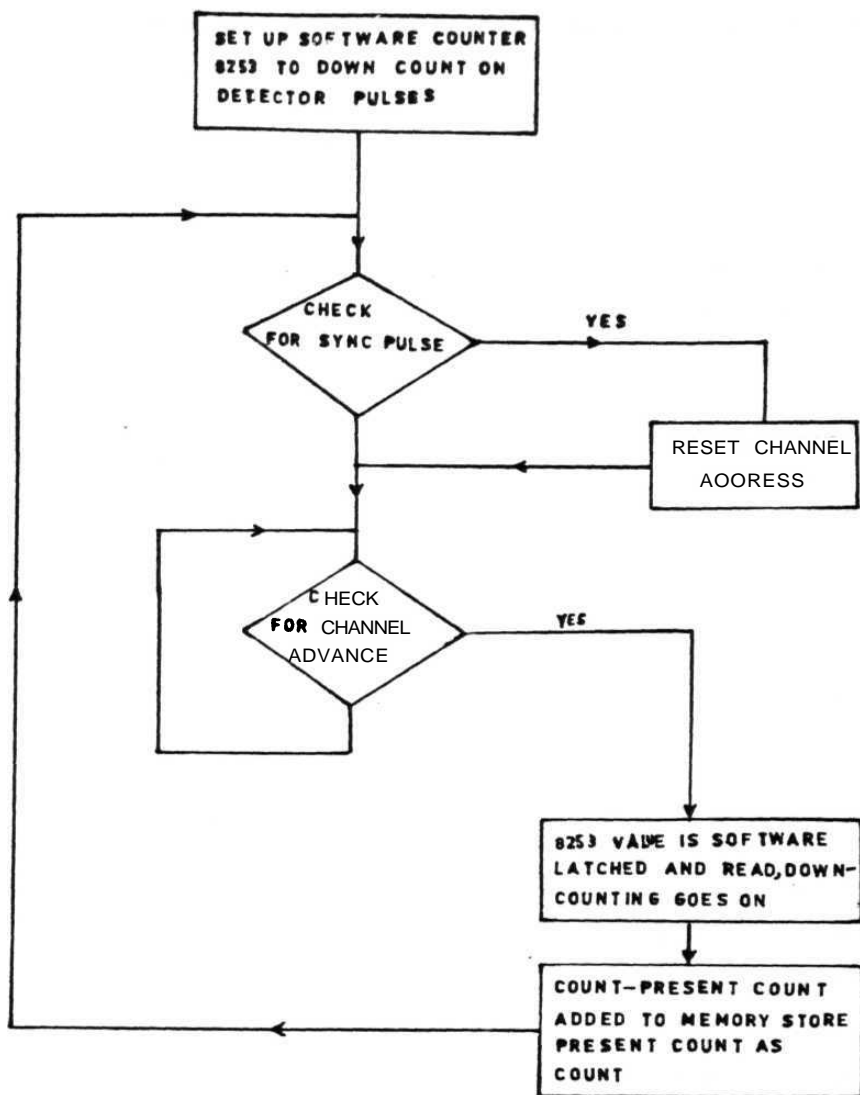


Fig.2.2. Flow chart to implement low dead time in data acquisition.

Everytime, whenever we run the spectrometer we copy this program on the RAM and run it.

2.1.d Low Temperature Measurements

The **Mössbauer** spectra in the temperature range 35 K - 300 K are recorded using a closed cycle variable temperature Mössbauer cryostat (Cryo Industries of America, Inc., USA, Model No. REF-399-D22). Fig. 2.3. shows the diagram of the cryostat. Vibration free bellows are provided to make the **sample** free from vibrations which are coming from the movement of the displacer. The flange **just** above the vibration free bellows is fitted to a rigid stand. This **stand** is fixed to a heavy table and table is isolated from any vibration on the floor by mounting on vibration free mountings. The whole cryostat is rigidly **clamped** on a concrete pillar. The sample is fixed to a hole in copper plate **which** is attached to one end of the **stainless** steel tube. This stainless steel tube is mounted in the cryostat such that the mylar windows and sample are in a line as shown in Fig. 2.3. The r-rays pass through the mylar windows and sample and are detected by the detector **on** the other side. The sample temperature is controlled with a temperature controller (Lake Shore Cryotronics, Inc., Model DRC 80C) using a silicon-diode sensor. The sample is heated with a heater which is wound just above the copper plate. Helium gas is used as exchange gas to make contact between the sample and cold head. The temperature stability is ± 0.5 K. Some of **Mössbauer** spectra at low temperatures (10 K - 300 K) are recorded at Low Temperature Physics Group Laboratory, **TIFR**, Bombay, using a continuous flow

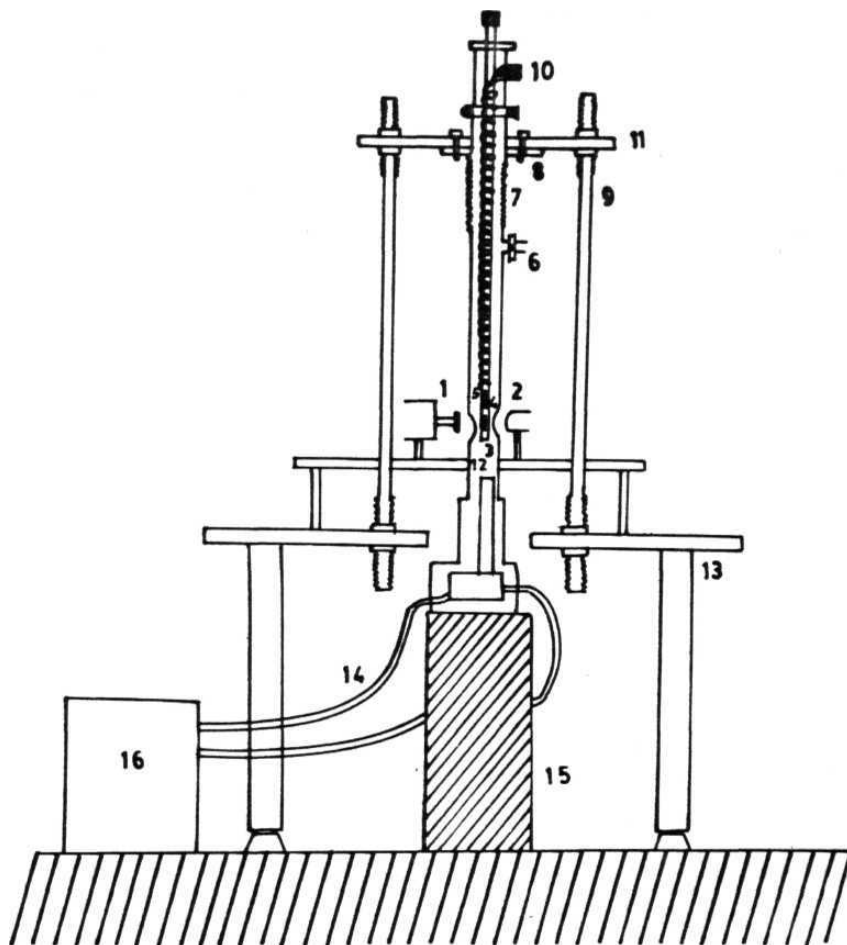


Fig.2.3. Set-up for Variable temperature Mössbauer experiments using closed cycle refrigerator (Model REF-399-D22, Cryo Industries). 1:Source mounted on the drive, 2:Detector, 3:Copper plate with sample, 4:Silicon diode sensor, 5:Heater, 6:Exchange gas inlet, 7:Bellows, 8:Flange, 9:Rigid stand, 10:Electrical feed-thru, 11:Heavy steel plate, 12:Cold head, 13:Heavy table, 14:Helium tubes, 15: Foundation, 16 :Compressor.

cryostat (Lake Shore Cryotronics, Inc., Model 310).

2.2. **MOSSBAUER** DATA ANALYSIS

For calibration runs and simple well resolved spectra a commercial Fast Fourier Transform (FFT) program (supplied by Ranger Corporation) is used to determine line positions, widths and intensities of the absorption peaks in the **Mössbauer** spectrum. When the spectrum consists of two or three sets of distinct hyperfine field split six line patterns at different field values, the FFT program can not be used due to the presence of several lines. For such complex spectra a stripping method is evolved which consists of the following steps for a spectrum arising **from** two hyperfine fields.

(i) In the first step, the approximate **value** of the outer field is estimated by a visual inspection of the experimental spectrum. The spectrum corresponding to outer field is subtracted from the overall experimental spectrum to get a single stripped spectrum corresponding to a lower field. This is fitted to a six line pattern using FFT program to get the line positions, widths, and intensities of the spectrum.

(ii) In the second step, the spectrum generated for the inner field using the parameters obtained in the first step is subtracted from the experimental spectrum to get the stripped spectrum for the outer field alone. This was again least square fitted using FFT program to get the fitted parameters for this

outer field.

(iii) The **spectrum** generated for the outer field using the fitted parameters in the step (ii) is once again subtracted from the experimental spectrum to get the spectrum for the inner field. This is least square **fitted** to get improved estimates of parameters for the inner spectrum. These improved parameters are used to get the stripped spectrum for the outer field.

(iv) This procedure is continued till the best fit parameters are obtained. Finally, the two stripped spectra are **combined** and the complete spectrum for the inner and outer fields is **generated**.

Spectra which consist of strongly overlapping and widely **distributed** fields are **analysed** using model independent field distribution analysis [3-6]. In Window's method the field distribution is expanded in a Fourier series

$$P(H) = \sum_{n=1}^N a_n [\cos(n\pi H/H_{\max}) - \cos n\pi] \quad (2.1)$$

The **Mössbauer** spectrum generated at velocity v due to this distribution is given by

$$S(v) = \int_0^{H_{\max}} P(H) L_6(v, H) dH \quad (2.2)$$

$$\text{where } L_6(v, H) = \sum_{i=1}^6 \frac{1}{\pi} \frac{\Gamma_i/2}{(\Gamma_i/2)^2 + (v - \alpha_i H)^2}$$

is the normalised shape function of the lines of a component spectrum for field H , Γ_i are the linewidths of the six lines of the component spectrum and $\alpha_i H$ are their positions. If the experimental spectrum is denoted by $W(v)$, the coefficients a_n of the field distribution are found by minimising the function

$$\phi = \sum_v [S(v) - W(v)]^2$$

with respect to the parameters a_n .

In the method proposed by Hesse and Rubertsch [5] and its modification by Le C  er and Dubois [6] the range of hyperfine field is divided into N equal intervals ΔH with $H_n = n \Delta H$ and the calculated spectrum is written as

$$S(v) = \sum_{h=0}^N P(H_h) L_6(H_h, v) \quad (2.5)$$

The probability for each field H_n is then obtained by minimisation of difference in calculated and experimental spectrum based on the procedure of Phillips [7] and Twomey [8]. The improvements in this procedure made by Le C  er and Dubois avoid problems of non-physical negative value of probability density which can sometimes arise if the background is not well defined.

It has been suggested [9] that one can assume the true dis-

tributions of hyperfine fields to be represented simply by a sum of **n** Gaussians

$$P(H) = \sum_{i=1}^n A_i \exp - \frac{[H - H_i]^2}{2\sigma_i^2} \quad (2.6)$$

with different positions (H_i), widths (σ_i) and weighting factors (A_i). This **seems** to work well because hyperfine field distributions obtained from model independent analysis are Gaussian shapes to a good approximation. The advantage is that less number of variables can be used in carrying out the fits, since usually two or three Gaussians suffice to fit the data. The optimised parameters of the Gaussians viz. position, intensity and width are obtained by minimising chisquare. A grid search method works **efficiently** once initial guesses of the parameters are obtained from some model independent field distribution **analysis** as outlined earlier.

2.3. FERROMAGNETIC RESONANCE SPECTROMETER

A commercial ESR spectrometer [JEOL FE-3X, Japan] operating in the X-band with a fixed microwave frequency of ≈ 9.23 GHz is used for **FMR** measurements. The block diagram of the ESR spectrometer is shown in Fig. 2.4. A klystron tube is used to generate the microwave radiation which passes as a linearly polarised beam through a wave guide. After traversing a ferrite isolator, which prevents the back reflections, and a variable attenuator, the beam is divided into arms 2 and 3 at a magnetic tee or hybrid tee

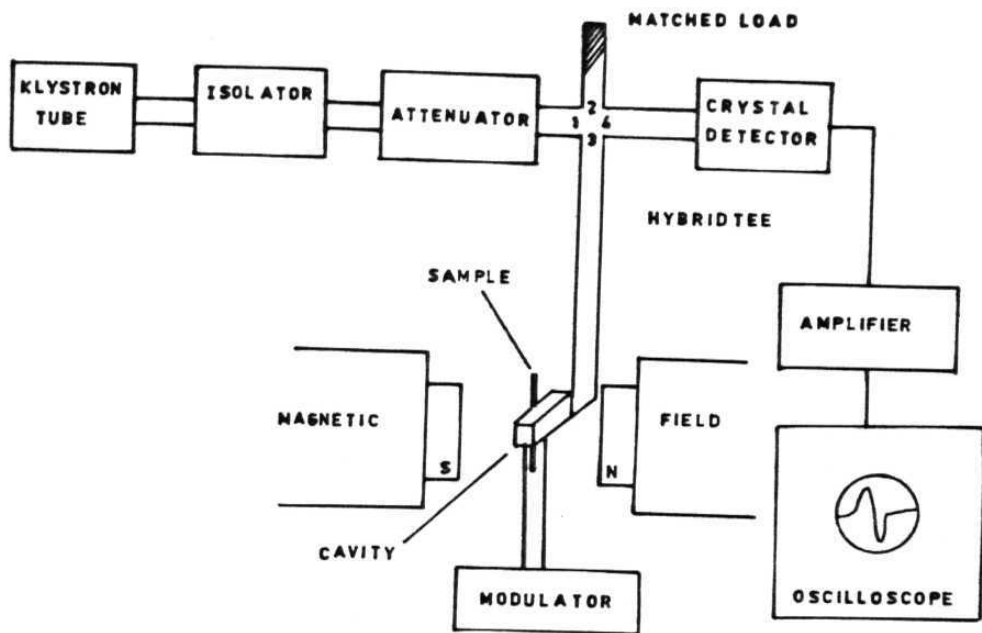


Fig.2.4. Block diagram of **FMR** Spectrometer used in the present work (JEOL, **FE-3X**).

so that there is no net **transmission** into arm 4 of the microwave **bridge**. The sample is placed in a cavity resonator that is positioned between the pole pieces of an electromagnet. The electromagnet produces a steady uniform magnetic field which can be swept at a constant rate. The sample is then exposed to a transverse microwave field of constant frequency. When the resonance condition is fulfilled, sample absorbs a part of the microwave energy and the **Q-value** of cavity resonator changes. The imbalance of the bridge occurs so that transmission into arm 4 takes **place**. The signal is detected by crystal detector, then amplified and displayed on an oscilloscope or graphic recorder. In the off-resonance condition, the reference wave is so **adjusted** to give a reflection equal in amplitude and opposite in phase to the reflection from the **sample** and cavity, sending zero power to arm 4. The magnetic field can be **modulated** with a low frequency (100 kHz) modulation which gives a first derivative representation of the microwave power with respect to the **field** (dP/dH).

The sample is mounted in **sandwiched** mode as shown in Fig. 2.5. The sample is first cleaned with **ethanol** and mounted in the groove of the flat surface of half-cut portion of the quartz rod at one end (Fig. 2.5a). The sample is sandwiched with a small flat quartz piece by placing on the sample. The **copper-constantan** thermocouple is attached to the quartz rod in such a way that the thermocouple bead could touch the sample (Fig. 2.5b). The whole assembly is slowly inserted in a quartz tube (Fig. 2.5c), which is then inserted into the cavity. The cavity is provided with a goniometer arrangement which enables the rotation and orientation

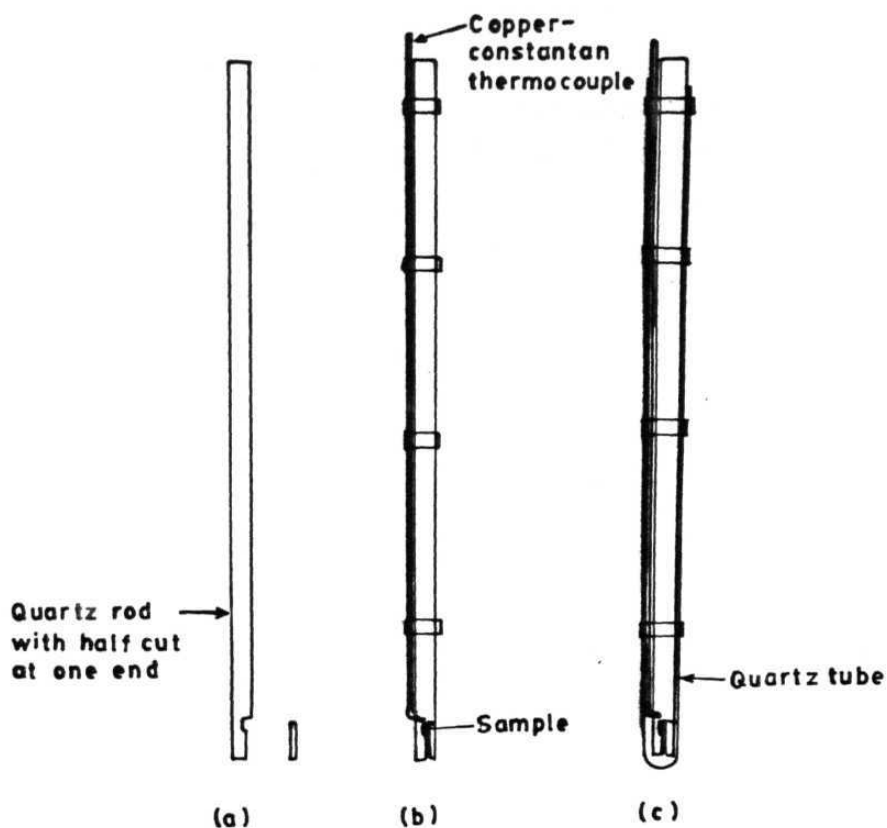
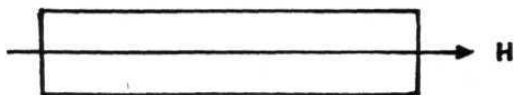


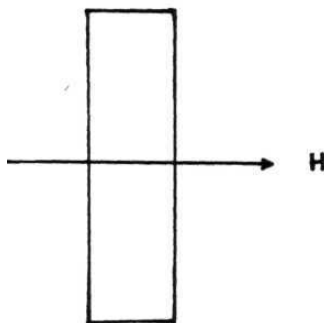
Fig. 2.5 a. Quartz rod with a half cut at one end and a groove to place the sample.
 b. Sample is sandwiched between the half cut end of the quartz rod and quartz piece. Copper-constantan thermocouple is attached to the quartz rod.
 c. The quartz rod with sample and thermocouple is pushed into a quartz tube.

of the **sample** plane at specific angles with respect to the external field. **FMR** measurements are carried out in two sample geometries (Fig. 2.6) - (i) horizontal-parallel (\parallel^h), in which the external field H lies in the sample plane and directed along the length of the sample, (ii) vertical-parallel (\parallel^v), in which H lies in the sample plane and is directed along the breadth of the sample. **FMR** spectra consist of recording the power absorption derivative (dP/dH) curves as a function of external static magnetic field H as shown in Fig. 1.10.

The low temperature (100 **K** - 300 **K**) **FMR** measurements are carried out with a variable temperature accessory. The sample is cooled with cold nitrogen gas, obtained by boiling liquid nitrogen, circulated through the cavity. The **temperature** outside the microwave cavity is **measured** with a **pre-calibrated** copper-constantan thermocouple at every set **temperature** by **regulating** the cold nitrogen gas flow. A proper gas flow regulation is achieved by controlling the power input to a heater, immersed in the liquid nitrogen container, with the help of **PID** controller. The accurate temperature of the sample is monitored with a pre-calibrated **copper-constantan** thermocouple in physical contact with the **sample**. The temperatures above room temperature (300 **K** - 500 **K**) are achieved by sending hot air through the cavity with the help of a compressor. The spectra at 77 **K** are recorded by immersing the sample in liquid nitrogen, contained in a tailed dewar, which had been inserted into the cavity.



(a)



(b)

- Fig.2.6** a. Horizontal-parallel ($||^H$) sample geometry in which the static magnetic field H lies in the sample plane and is directed along the length of the **sample**.
- b. Vertical-parallel ($||^V$) sample geometry in which the static magnetic field H lies in the sample plane and is directed along the breadth of the sample.

2.4. AC SUSCEPTIBILITY

AC susceptibility (ACS) **measurements** in the temperature **range** 10 K - 400 K are carried on the **same** samples which are used for **FMR** measurements. The mutual inductance technique at a fixed frequency of 33 Hz is used. AC magnetic field, $H = 0.5$ Oe without superimposed dc magnetic field is applied in the primary excitation coil. The resistance of the primary coil is 35 Ω . The secondary consists of two closely matched and oppositely wound coaxial coils. In **the** absence of the sample, the voltages induced at the two secondary coils cancel each other. The sample is placed in one of the coils and the difference between the voltages induced in the coils is measured using dual phase **lock-in-amplifier** (Model 5210 from PARC) in the A - B **mode**. The reference signal is derived from a 1 k Ω resistor in series with the primary **coil**. The in-phase and quadrature phase signals give the loss (χ'') and inductive (χ') components of the complex ac susceptibility $\chi = \chi' - i\chi''$. The sample is cooled to 10 K with a closed cycle refrigerator (APD Cryogenics Inc., USA, Model **HC-2**). The cold head tip temperature is controlled using a small heater present on it and silicon diode sensor near to it. The sample temperature is controlled with a silicon diode sensor present near the sample. The cold head and sample temperature are controlled with a microprocessor based temperature controller (5500 series from Scientific Instruments Corporation). The temperature stability is ± 30 mK. To obtain the accurate value of the sample signal, background (without sample) signal is measured throughout the temperature range and subtracted from the actual signal.

2.5. SAMPLE PREPARATION

The alloys studied in this thesis work are prepared by melting in an arc melting furnace (Materials Research Corporation, USA, Model AF-82C). To prepare the alloys of required composition, grade I purity iron powder (JMC Puratronic), m3N7 purity manganese chips, m3N5 aluminium shots, m3N nickel powder, m3N5 silicon powder and m3N5 chromium powder (Alfa Division) are used. The elements in the powder form are mixed thoroughly in a mortar and pestle and compressed into a pellet applying a pressure of $8 - 10 \text{ tons/cm}^2$ using a hydraulic press. The pellet and chips and/or shots are kept together in a groove in the copper hearth of the furnace. The entire lower surface of copper hearth is cooled with a water flow of 2 gpm. The chamber is first evacuated to a pressure of 30 inches of Hg and flushed three times with argon gas to remove the residual gases. Finally, chamber is filled with argon gas at a pressure of 20 to 25 inches of Hg. Then the arc is generated from the tip of a water cooled movable tungsten electrode and is directed on to the materials kept in the groove and melting is done. The melt is reversed and melted again to ensure the homogeneity. The weight loss in melting process is calculated. The typical weight loss is approximately 2 - 5%.

The alloy ingots are sealed in quartz tubes under a pressure
-4

of 10 torr after flushing three times with argon gas and homogenised at required temperature for sufficient time. To prepare Mossbauer absorbers, a part of homogenised alloy ingot is filed

into coarse powder and subsequently ground into finer powder using mortar and pestle. The powders are sealed in quartz tubes under a pressure of 10^{-3} torr after flushing three times with argon gas and annealed for sufficient time at required temperature to relieve strains. Mössbauer absorbers are prepared from annealed powders after mixing with boron nitride powder and pressing into pellets. For FMR and AC susceptibility measurements, samples of typical dimension $2 \times 1 \times 1$ mm are cut from the homogenised alloy ingots.

To prepare the disordered alloys of Fe_3MnAl alloys, the alloy ingots are homogenised and quenched from 1000°C in liquid nitrogen. Some of the homogenised ingots of $\text{Ni}_3\text{Fe}_1\text{Si}$ alloys are splat quenched in an Edmund Bühler ultra quenching apparatus. Powder is prepared from the quenched ingot of $\text{Fe}_1\text{Mn}_1\text{Al}$ alloy and annealed at 300°C for different periods of time to study the kinetics of disorder-order transformations.

2.6. CHARACTERISATION OF SAMPLES

The samples are characterised by powder diffraction on a Siefert Isodetyeflex Model 2002 X-ray diffractometer using CuK radiation. Some of the samples are also characterised using CoK and MoK $_{\alpha}$ radiations. 2θ values are measured from the diffraction patterns. Then the d values, hkl values and lattice parameter(a) are calculated. In the case of $\text{Fe}_{1-x}\text{Ni}_x\text{Si}$ alloys, a previously available computer program [10] is used to calculate the lattice parameters and other parameters. In the case of $\text{Ni}_3\text{Fe}_1\text{Si}$

alloys, lattice **parameter** (a) values **are** calculated using Bragg's law and Jay plots [11]. The value of ' a ' is calculated for each line in the x-ray diffraction pattern with indexed **hkl** values and **are** plotted against $\cos^2 \theta$. By the extrapolation of a vs. $\cos^2 \theta$ plot to $\theta = 90^\circ$, the intercept on the ordinate gave the exact value of **a**.

REFERENCES

- [1] J.T.T. **Kumaran** and C. Bansal, Nucl. **Instrum.** and Methods in Physics Research **B61**, 357 (1991).
- [2] E. **Kankeleit**, "Mössbauer Effect Methodology", Vol.1, edited by **I.J. Gruverman** (Plenum press, New York, **1985**).
- [3] C. Bansal, Bull. Mater. Sci., 6, 1047 (**1984**).
- [4] B. Window, J. Phys. E4, 401 (1971).
- [5] J. Hesse and A. Rubertsch, J. Phys. **E7**, 526 (1974).
- [6] G. Le **Câer** and J.M. Dubois, J. Phys. E12, **1083** (1979).
- [7] **D.L.** Phillips, J. Ass. **Comput. Mach.**, 9, 84 (1962).
- [8] S. **Twoney**, J. Ass. Comput. Mach., **10**, 97 (1963).
- [9] D.G. Rancourt and J.Y. Ping, Nucl. Instrum. and Methods in Physics Research **B58**, 85 (1991).
- [10] "An Interactive x-ray powder Diffraction Data Interpretation and Indexing program", Version 2.2, E.Wu, Flinders University of South America, Australia.
- [11] "**X-ray** Diffraction Procedures" by H.P. **Klug** and **L.E.** Alexander (Wiley, New York, 1974).

CHAPTER 3

MAGNETIC BEHAVIOUR IN $Fe_{3-x}Mn_xSi$ ALLOYS

3.1. INTRODUCTION

The properties of the quasi-binary alloy system Fe_3MnSi have been extensively studied and there is a considerable interest in understanding the unusual magnetic behaviour of the system. Fe_3Si is a **ferromagnet** ($T_C = 810 \text{ K}$) whereas Mn_3Si is an antiferromagnet ($T_N = 25.8 \text{ K}$) [1] and the state of magnetic order in $\text{Fe}_{3-x}\text{Mn}_x\text{Si}$ changes from ferromagnetic for $x < 0.75$ to a complex one for $x \geq 0.75$ due to the presence of mixed **ferromagnetic** and antiferromagnetic exchange interactions [2]. Single phase alloys in this system are formed in a wide concentration range $0 \leq x \leq 1.8$ with the end members Fe_3Si and Mn_3Si both existing as stable DO_3 ordered phases. The DO_3 structure is shown in Fig. 3.1 and consists of four interpenetrating sublattices labelled A, B, C, and D, shifted along the body diagonal and having origins at $(0,0,0)$, $(1/4, 1/4, 1/4)$, $(1/2, 1/2, 1/2)$ and $(3/4, 3/4, 3/4)$. In DO_3 ordered Fe_3Si , A, B, and C sites are occupied by Fe and the D sites are occupied by Si. A and C sites have **identical** first near neighbour environment (4 Fe atoms at B site and 4 Si atoms at D site) whereas the B site Fe atom have 8 iron neighbours belonging to the A and C sites. Table 3.1 shows the near neighbour (nn) **configuration** of Fe_3Si . Alloying of Fe_3Si with other 3d metals led to a remarkable finding [2] that the metals to the left of Fe in the periodic table substitute **preferentially** at B sites whereas the ones to the right of Fe have a preference for A and C sites. This substitutional behaviour permits study of host-impurity interaction at high impurity concentrations because as seen from Table 3.1, impurity-impurity atoms come only as third

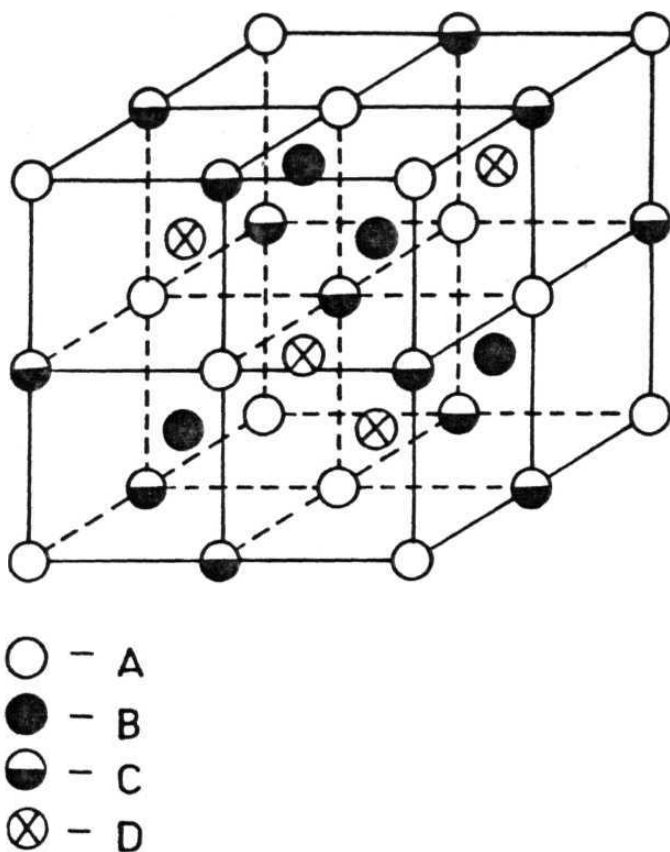


Fig.3.1. DO_3 structure with A, B, C, and D sublattices having origins at $(0,0,0)$, $(1/4,1/4,1/4)$, $(1/2,1/2,1/2)$ and $(3/4,3/4,3/4)$ along the body diagonal.

Table 3.1. Near neighbour **configurations** of (AC), B and D sites in the **DO₃** structure. The near neighbour distance in units of lattice constant a .

Shell No. Site	1	2	3	4	5	6	7	8
AC	4B 4D	6AC	12AC	12B 12D	8A	6A	12B 12D	24A
B	8AC	6D	12B	24AC	8D	6B	24AC	24D
D	8AC	6B	12D	24AC	8B	6D	24AC	24B
nn distance r/a_o	0.433	0.5	0.707	0.829	0.866	1.0	1.09	1.118

neighbours. It was observed that in Fe_3Si based alloys the magnetic moments and hyperfine fields are sensitive only to the nearest neighbour **configurations** and a local environment model was found to explain the magnetic behaviour of these alloys [2].

Magnetisation and neutron diffraction studies on concentrated $\text{Fe}_{3-x}\text{Mn}_x\text{Si}$ alloys [3] show that the average magnetic moment falls approximately linearly with Mn concentration for $x \leq 0.75$. Only Fe at B sites are substituted by Mn upto this concentration [3]. The magnetic moment of Fe at B sites (all 8 Fe neighbours at AC sites and no Mn nearest neighbours) stays nearly constant at about $2.2 \mu_B$ whereas the AC site moment decreases linearly with Mn concentration to $0.4 \mu_B$ as these sites have four B site near neighbours which have been substituted by Mn. Beyond $x = 0.75$, the AC sites also start getting occupied by Mn atoms and the B site moment also decreases rapidly due to the presence of Mn first neighbours. Since there are no more changes of the AC site environment the moment at this site stays constant at about $0.4 \mu_B$.

Although a fair degree of understanding exists for the saturation moments and corresponding hyperfine fields at the different sites based on this local environment approach [4-6], the temperature dependent behaviour and the nature of magnetically ordered phases in the system in the compositions regions $x \geq 0.75$ is neither well studied nor understood. An extensive temperature dependent study of AC susceptibility (ACS), Ferromagnetic resonance (FMR), and hyperfine fields by **Mössbauer** spectro-

scopic measurements was carried out on the $\text{Fe}_{3-x}\text{Mn}_x\text{Si}$ system in $0.75 \leq x \leq 1.2$ concentration region. These studies show **interesting** re-entrant spin glass behaviour and an attempt is also made to understand these properties in the light of existing **models** for re-entrant spin glasses [7-9].

3.2. EXPERIMENTAL

Four alloy samples of compositions $\text{Fe}_{3-x}\text{Mn}_x\text{Si}$ ($x = 0.75, 0.9, 1.0$ and 1.2) were prepared by arc melting. **Mössbauer** effect studies in the temperature range $10 \text{ K} - 300 \text{ K}$ were performed on these samples in powder form. **FMR** studies in the temperature range $77 \text{ K} - 480 \text{ K}$ were carried out using cuboid shaped (dimensions $2\text{mm} \times 1\text{mm} \times 1\text{mm}$) alloy samples in the **horizontal-parallel** and vertical-parallel geometries. AC susceptibility measurements in the temperature range $10 \text{ K} - 400 \text{ K}$ were also carried out on the same samples at a frequency of 33 Hz and $H = 0.5 \text{ Oe}$. Other details of experimental methods are given in chapter 2.

3.3. RESULTS

3.3.a. AC Susceptibility

Fig. 2a shows the measured temperature dependence of AC susceptibility for the four alloy samples. The data show very clearly a drop in AC susceptibility from the demagnetisation factor limited value at two temperatures T_C and T_{RE} . This behaviour is usually considered as a canonical signature for re-entrant spin

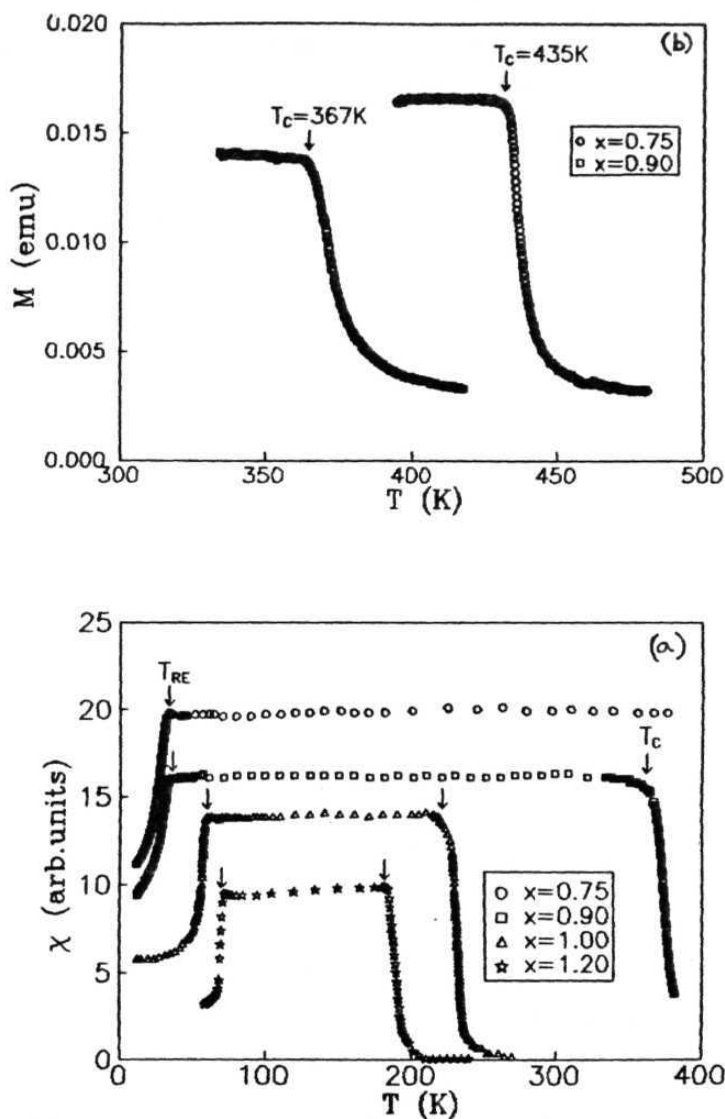


Fig.3.2 a. Variation of AC susceptibility (χ) with temperature (T) for $\text{Fe}_{0.3}\text{Mn}_x\text{Si}_{1-x}$ alloys. T_{RE} denotes the reentrant spin glass temperature and T_c is the ferromagnetic to paramagnetic transition temperature.

b. Variation of dc magnetisation (M) with temperature (T) for $x = 0.75$ and $x = 0.90$ alloy compositions. T_c values are indicated.

glass systems. The AC susceptibility measurements have been carried out in a low demagnetisation factor geometry (H parallel to surface of the sample and along its length). The calculated demagnetisation factor [10] for this geometry and sample dimensions is 0.1. The experimentally measured susceptibility is given by [11]

$$\chi_e = \frac{1}{1/\chi_i + D} \quad (3.1)$$

where χ_i is the internal susceptibility and D is the demagnetisation factor. For $\chi_i \gg D$ as in ferromagnetic region, χ_e reduces to the demagnetisation limited constant value of D . It was pointed out by Rakers and Beck [11] that in a low demagnetisation factor geometry, the susceptibility does not show demagnetisation limited behaviour in $\text{Au}_{82}\text{Fe}_{17.5}$ alloy and thus the transition at T_c is not to a true ferromagnetic phase in the AuFe system. In our alloy system, the existence of demagnetisation limited behaviour even for low demagnetisation factor shows that the internal susceptibility is large as compared to $D = 10$ which is a substantially large value as compared to susceptibility of paramagnetic or superparamagnetic systems. The transition at T_c therefore corresponds to formation of a ferromagnetic state. Evidence from specific heat measurements [12] show only a broad step like anomaly at the ferromagnetic transition and distinct cusp shape peaks are seen at T_{RE} only. The change in magnetic entropy at T_c is very small ($2-3 \text{ J mole}^{-1} \text{ K}^{-1}$) as compared to the value $3R \ln 2 = 17.3 \text{ J mole}^{-1} \text{ K}^{-1}$ expected for ordering of 3N magnetic spins with $S = 1/2$. This shows that all spins are not ordering

below the ferromagnetic transition at T_c and this behaviour will be analysed in more detail later in terms of the unusual structure and site occupation by Fe and Mn atoms in the structure. From dc magnetisation measurements (Fig. 2b), T_c value for $x = 0.75$ alloy composition was measured, and T_c value for $x = 0.9$ alloy composition was confirmed. T_c and T_{RE} values are given in Table 3.2.

3.3.b. Ferromagnetic Resonance

Fig. 3.3 shows the observed dP/dH (Power absorption derivative) with H for $x = 1.0$ alloy composition in the horizontal-parallel ($||$) geometry for a few selected temperatures. These are representative of vertical-parallel ($||^V$) geometry also and of alloys of other compositions in $||$ and $||^V$ geometries. The equations representing the theoretical lineshape for dP/dH has been presented by Kaul and Siruguri [13] and a least squares fit of the experimental data to this line shape gives a g value of 2.07 ± 0.02 which is temperature independent and gives the accurate values of resonance field (H), linewidth (ΔH) and saturation magnetisation (M_s). The details of line shape analysis are given in chapter 1 (See Eqs. 1.38 and 1.39).

The temperature dependence of resonance field (in $||$ geometry) and saturation magnetisation, M_s , are shown in Figs. 3.4 and 3.5 respectively. The observed temperature dependence of magnetisation is now used to distinguish between localised and itinerant electron models. The variation of spin wave stiffness coefficient with temperature is different for the two models [14] being given

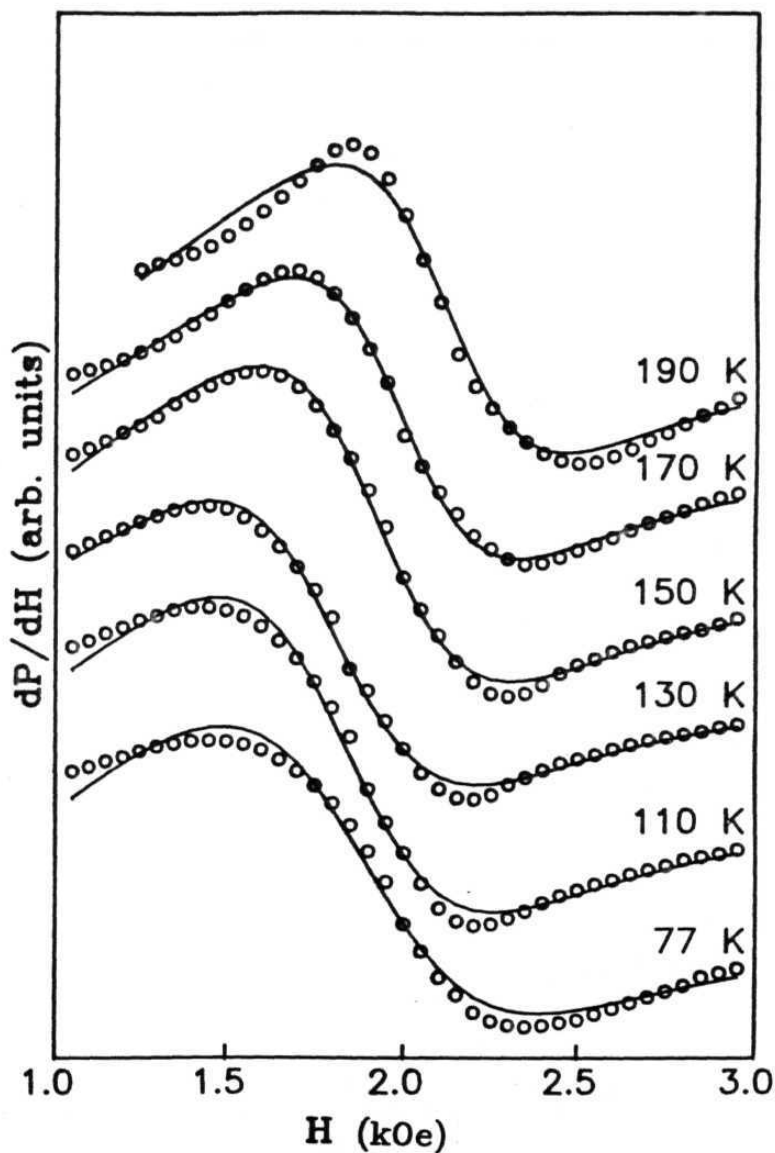


Fig.3.3. FMR power absorption derivative spectra at different temperatures for Fe_2MnSi alloy. The solid line indicates the fit to the experimental spectrum based on Eqs. 1.38 and 1.39.

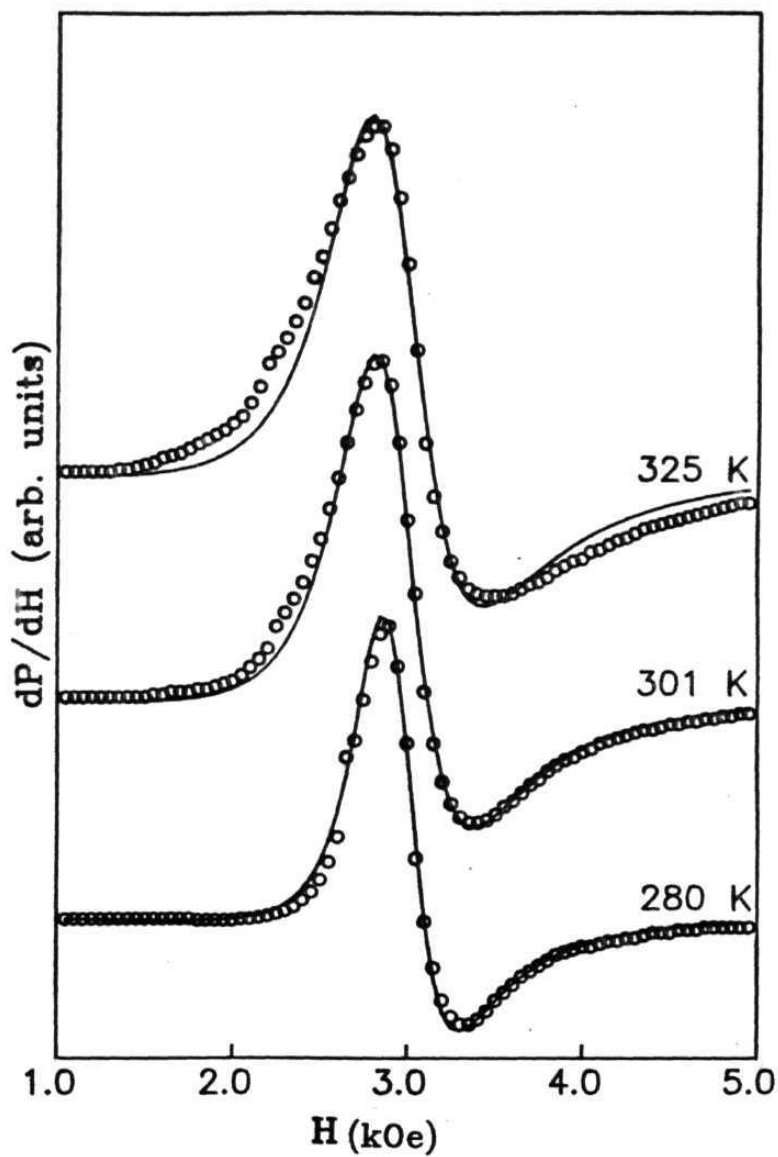


Fig.3.3. Continued.

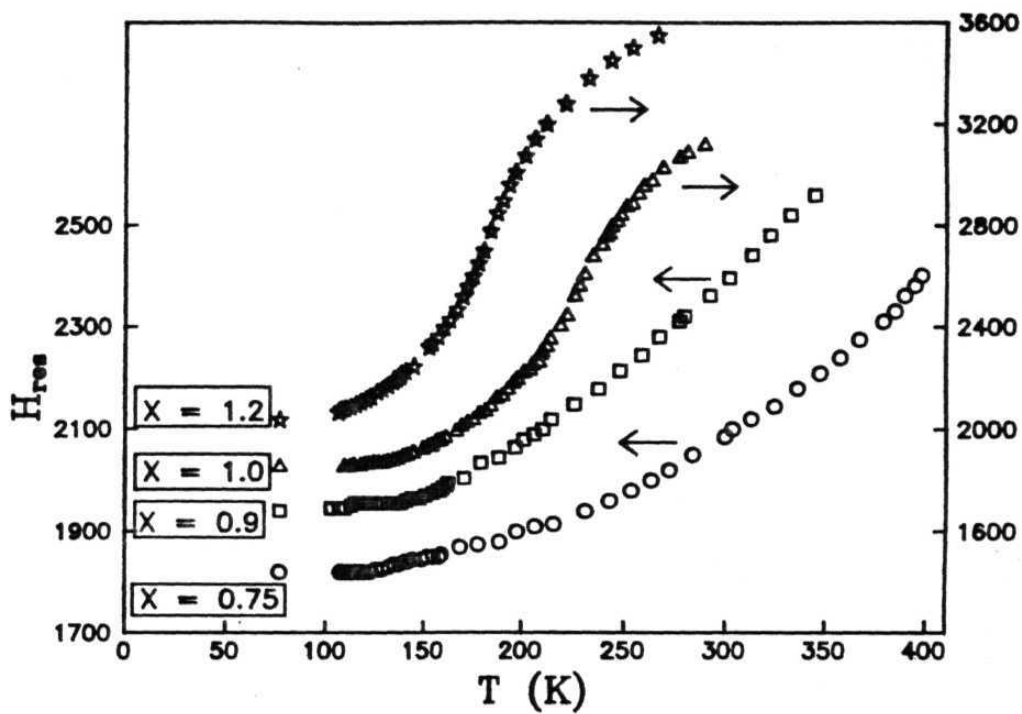


Fig.3.4. Variation of the FMR resonance field (H_{res}) with temperature (T) in Fe-Mn-Si alloys.

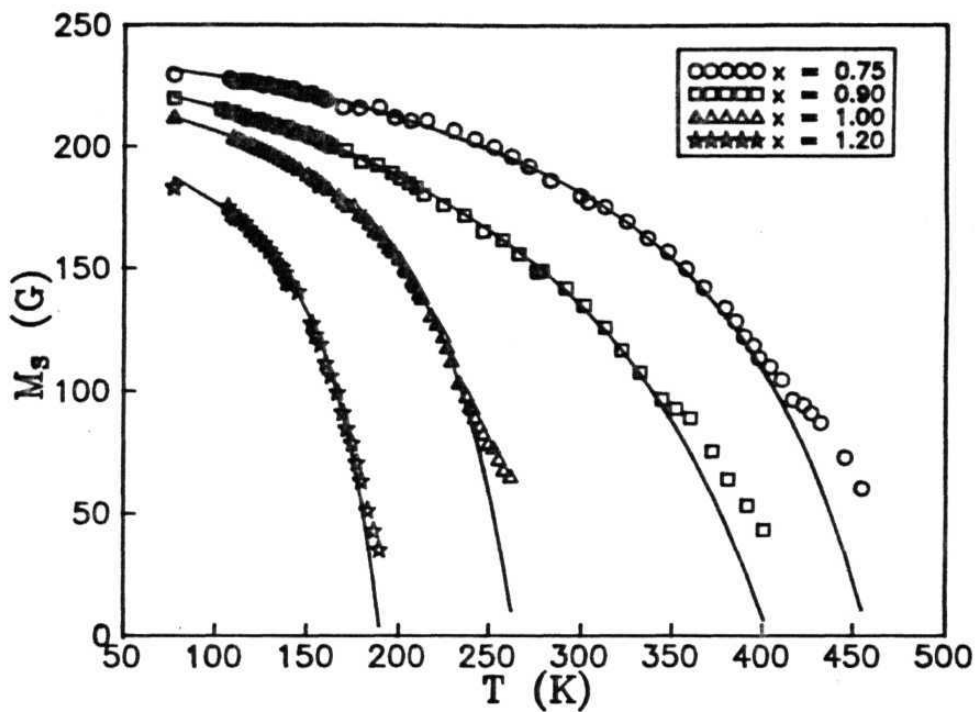


Fig.3.5. The dependence of saturation magnetisation (M_s) on temperature (T) for $\text{Fe}_{3-x}\text{Mn}_x\text{Si}$ alloys. The solid line indicates the fit to the data using the spin wave relation [Eq. 3.4].

by

$$D(T) = D(0)[1 - D_2 T^2] \quad (3.2)$$

and

$$D(T) = D(0)[1 - D_{5/2} T^{5/2}] \quad (3.3)$$

for the itinerant- and **localised-electron** models respectively. The dependence of **magnetisation** on temperature and spin wave stiffness coefficient is theoretically given by [15,16]

$$M_S(T) = M_S(0) - g\mu_B Z(3/2, t_H) \left[\frac{k_B T}{4\pi D(T)} \right]^{3/2} \quad (3.4)$$

where $Z(3/2, t_H)$ denotes the Bose-Einstein integral function

$$Z(s, t_H) = \sum_{n=1}^{\infty} n^{-s} \exp(-nt_H) \quad (3.5)$$

and

$$t_H = T_g/T = \frac{g\mu_B H_{eff}}{k_B T} \quad (3.6)$$

The factor Z in **Eq. 3.4** arises because there is an energy gap $\Delta = g\mu_B H_{eff}$ in the spin wave spectrum in the presence of the effective field

$$H_{eff} = H - 4\pi NM + H_k \quad (3.7)$$

where M is the magnetisation, N is the demagnetisation factor and H_k is the anisotropy field.

Fits to magnetisation data were carried out using **Eq. 3.4** and for the two forms of $D(T)$ given by **Eqs. 3.2** and **3.3**. The tem-

perature dependence of $D(T)$ for the **localised-electron** model (Eq. 3.3) gave much better fits than those for itinerant-electron model. As a **further** check, a plot of $\left\{ \frac{[M_S(0) - M_S(T)](D(T))^{3/2}}{Z(3/2, t_H)} \right\}$ vs. $T^{3/2}$ with $D(T)$ from 3.3 gives a straight line passing through origin (Fig. 3.6) for all compositions.

Table 3.2 gives the values of $D(0)$ and $D_{5/2}$ for alloys of different **Mn** concentrations. The validity of Eq. 3.3 in the present case implies that the **localised-electron** model adequately describes $D(T)$. Moreover the ratio $D(0)/T_C$ of about $0.6 \text{ meV}^2 \text{K}^{-1}$ is obtained for all the compositions. This ratio is related to the mean square range of the exchange interaction [17]

$$\frac{D(0)}{T_C} = \left[\frac{k_B}{2(S+1)} \right] \langle r^2 \rangle$$

and gives $\langle r^2 \rangle \cong 0.9 a_0^2$ (where a_0 is lattice constant) and implies a range of the exchange interactions extending upto fifth nearest neighbours (Table 3.1)

The temperature variation of **FMR** linewidths is shown in Fig. 3.7. The linewidth first goes through a minimum at lower temperature followed by a maximum at higher temperature (Fig. 3.7). The linewidth increase below T_c extends over a very large temperature region. This increase in linewidth is typical of re-entrant spin glass systems [13,18] and can be described by an empirical relation [19]

Table 3.2. Magnetic transition temperatures and spin wave parameters for $\text{Fe}_{3-x}\text{Mn}_x\text{Si}$. Numbers in brackets indicate errors.

x at X	T_C K	T_{RE} R	$M_S(0)$ G	$D(0)$ meVÅ ²	$D_{5/2}$ 10 ⁻⁷ K ^{-5/2}	$D(0)/T_C$ meVÅ ² /K	$\langle r^2 \rangle$ Å ²
0.75	435(1)	32(1)	237(10)	225(10)	1.15(10)	0.52(2)	24.138
0.90	370(1)	35(1)	230(10)	160(10)	1.20(20)	0.43(3)	19.961
1.00	230(1)	58(1)	222(10)	150(10)	5.00(50)	0.65(5)	30.173
1.20	190(1)	72(1)	203(10)	115(10)	11.50(50)	0.61(3)	28.316

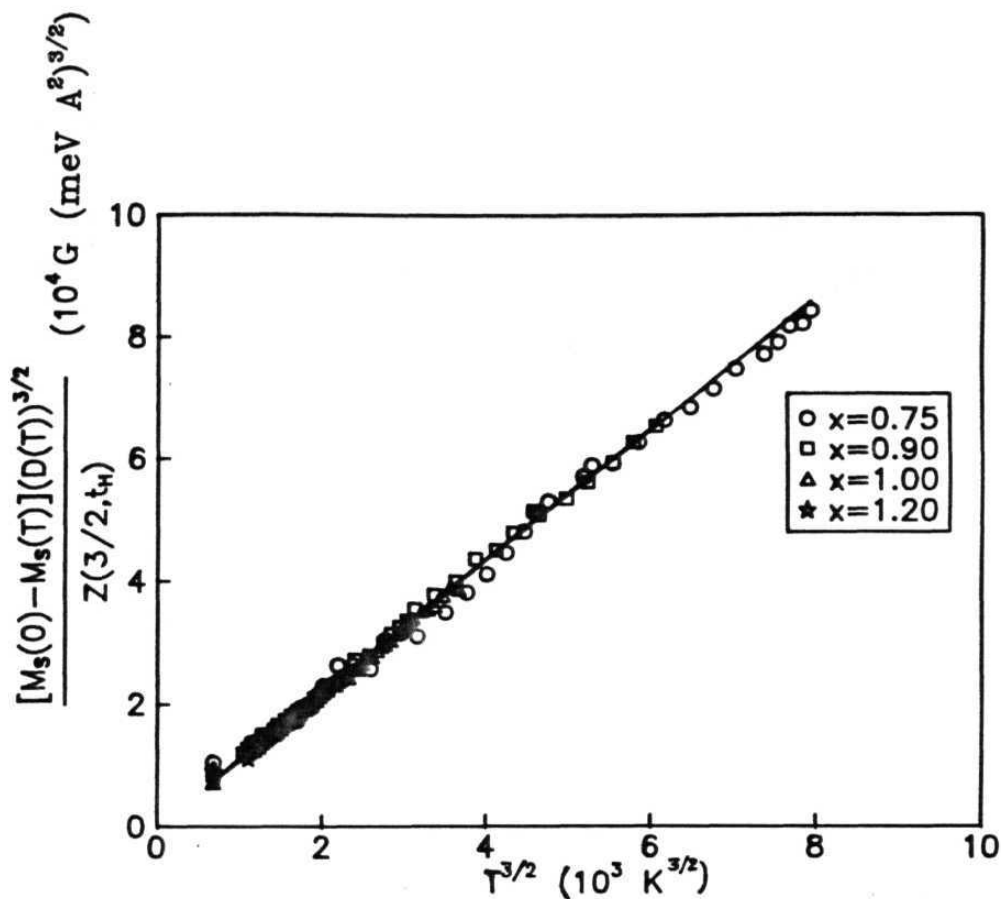


Fig.3.6. Variation of $\frac{[M_S(0) - M_S(T)](D(T))^{3/2}}{Z(3/2, t_H)}$ with $T^{3/2}$ in $\text{Fe}_{3-x}\text{Mn}_x\text{Si}$ alloys. The straight line passing through origin shows that the **localised-electron** model [Eq. 3.3 and 3.4] describes the temperature dependence of saturation magnetisation (M_S).

$$\Delta H_{pp} = \Gamma_0 + \Gamma_1(T/T_0)\exp(-T/T_0) \quad (3.9)$$

where for a given Mn concentration and microwave frequency, Γ_0 , Γ_1 and T_0 are constants. The observed temperature dependence of linewidth was fitted to Eq. 3.9 and the fits are also shown in Fig. 3.7. In **re-entrant** spin glass systems there is a region of constant linewidth below T_c and the linewidth rises below about $T \cong 2 T_{RE}$ and follows the empirical form given by Eq. 3.9 [13]. In the **Fe₂ Mn Si** system however the increase in linewidth starts at a very high **temperature** (in fact just below T_c for $x = 1.0$ and 1.2 compositions) and follows the form given by **Eq. 3.9** in a very wide temperature range.

3.3.c. Mössbauer Spectroscopy

The temperature dependence of Mossbauer absorption spectra for $x = 0.75$ composition is shown in Fig. 3.8. The hyperfine magnetic field distribution derived from the spectra using Le **Câer's** method (Chapter 2) are also shown. The assignment of the higher fields in the region 300 kOe to Fe atoms at B sites (8 AC near neighbours) and the lower fields (200 kOe and lower) to AC sites (B and D site neighbours) has been established quite uniquely by several experiments and analysis procedures, not only for **Fe₃Si** based systems [4-5, 20] but for other **DO₃** ordered **A₂B** alloys as well [21-23]. The magnetic moment for the B site atom (both Fe and Mn) is about $2 \mu_B$ for Mn concentration upto 0.75 whereas the AC site moment falls from $1.5 \mu_B$ to $0.4 \mu_B$ with Mn concentration due to substitution of Mn neighbours in their nn environment

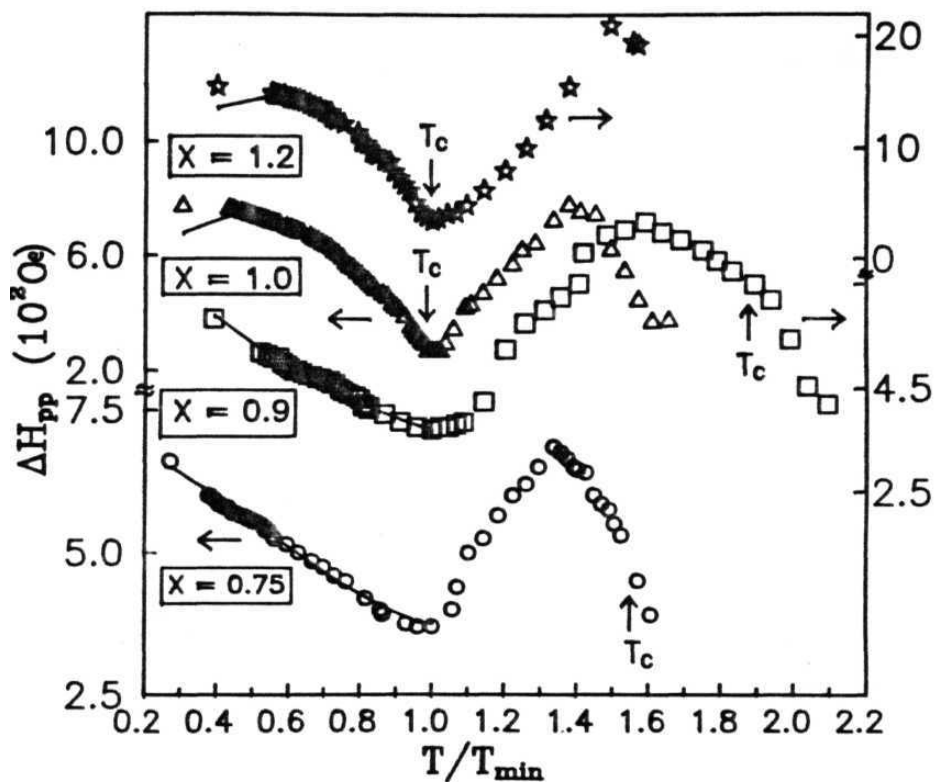


Fig.3.7. Variation of FMR linewidth (ΔH) with temperature in $\text{Fe}_x\text{Mn}_{1-x}\text{Si}$ alloys. T_c is the temperature at which linewidth goes to a minimum. T_c values from AC susceptibility measurements are indicated. The solid line through the data points in low temperature region is the fit to the data using Eq. 3.9.

[24]. For low Mn concentration, the Mn atoms go to occupy only the B site exclusively but at $x = 0.75$ although all B sites have not been filled, some Mn atoms start filling the AC sites as well [24]. This gives a wide variety of environments and the field distributions in Fig. 3.8 clearly depicts this situation. The field distributions below 200 kOe peaked at different field values arise due to Fe (AC) sites with different numbers of Mn neighbours, the lower field values corresponding to higher number of Mn neighbours. The correlation between hyperfine field (at 80 K), Fe(AC) moment and number of Mn . ($n = 0 - 4$ as there are always 4 Si D neighbours to this site) neighbours is shown in Fig. 3.9. The observed linear correlation gives us a good deal of confidence in our assignment of peaks in the field distribution to the number and type of B site near neighbours around Fe (AC) sites. The fields originating from B site Fe atoms also have a distribution at 300 kOe which arises predominantly from variations in Mn occupation in third neighbour shell (Table 3.1) and also from Mn first neighbours substituting at AC sites. The field changes are not easily resolvable in the distributions. However they approximately correspond to Fe atoms with (8Fe, 0Mn), (7Fe, 1Mn) etc. **configurations**.

The temperature dependence of hyperfine field for each of these **configurations** is shown in Fig. 3.10. The decrease in hyperfine field with temperature is faster for the higher Mn configurations. This behaviour is further analysed for the $x = 0.9$ alloy sample for which data were recorded in a wider temperature range of 10 K - 300 K.

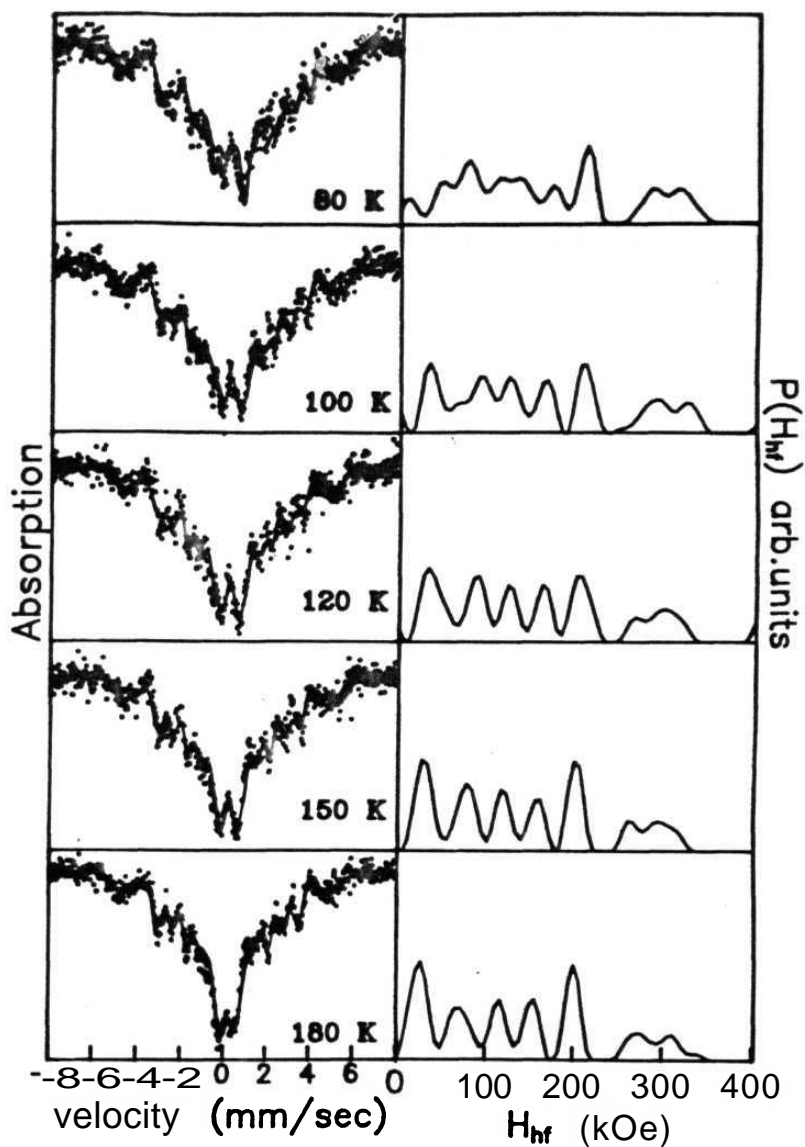


Fig.3.8. Mössbauer spectra and their hyperfine field distributions (calculated using model-independent Le Cœur program) at different temperatures for $\text{Fe}_{2.25}\text{Mn}_{0.75}\text{Si}$ alloy.

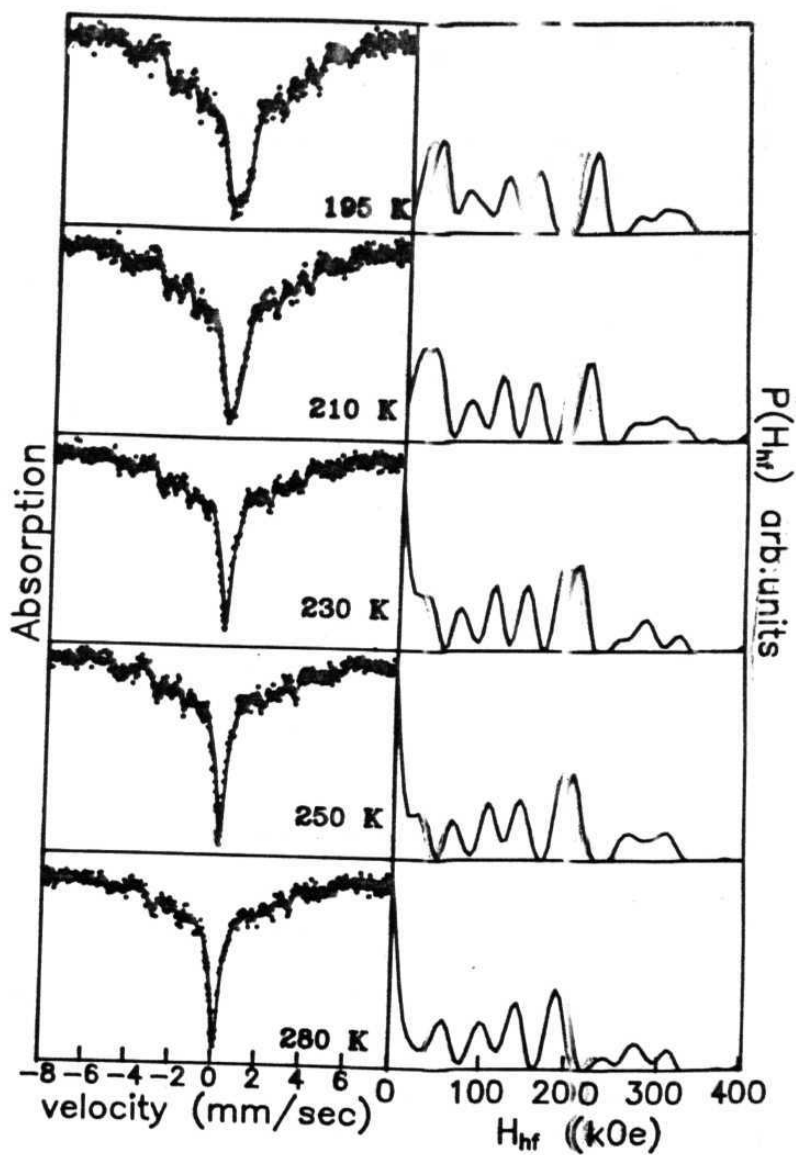


Fig.3.8. Continued.

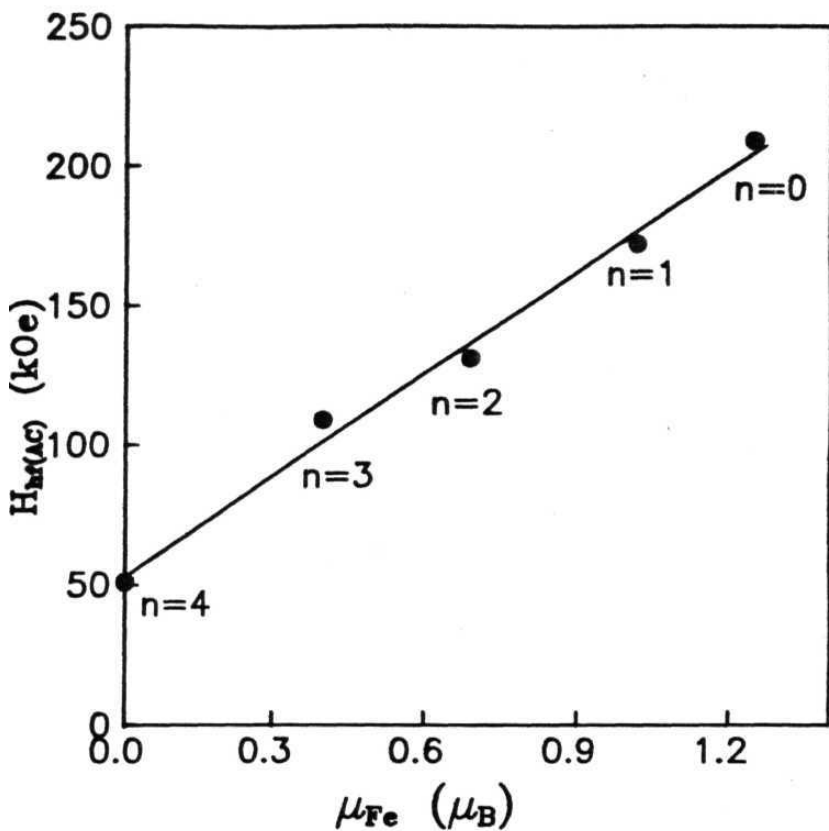


Fig.3.9. Correlation between Fe hyperfine field and magnetic moment (μ_{Fe}) for AC site Fe atoms. The number of *tin* nn atoms for these sites is indicated by n .

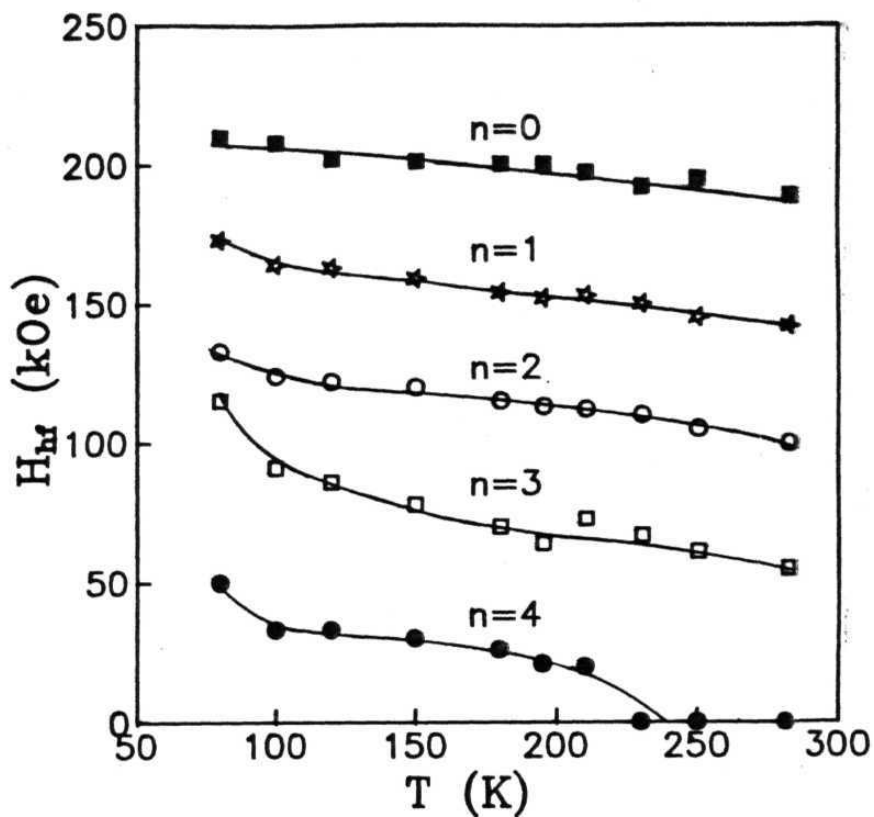


Fig. 3.10. Temperature dependence of hyperfine field (H_{hf}) for Fe(AC) atoms having different number of Mn near neighbours (n) for $\text{Fe}_{2.25}\text{Mn}_{0.75}\text{Si}$ alloy.

Fig. 3.11 shows the temperature dependence of **Mössbauer** spectra for $x = 0.9$ composition in the temperature range 10 K - 300 K. The assignment of peaks in the field distributions to various Hn neighbours of AC site Fe atoms is done as discussed earlier for $x = 0.75$ composition. Fig. 3.12 shows the temperature dependence of hyperfine field for each of the **Fe(A,C)** sites with different Hn first neighbours. The temperature dependence is clearly more pronounced for the **configurations** with higher number of Mn near neighbours. This behaviour can be attributed to the weaker Fe-Mn exchange interaction relative to Fe-Fe exchange. Neutron scattering studies at lower Mn concentration [25] give $J_{F-F} = 25.4$ meV, $J_{F-M} = 8.2$ meV and a very small or negative value for J_{Mn-Mn} . The faster decrease in hyperfine field for the Fe **configuration** with higher number of Mn neighbours is then due to a smaller exchange interaction with its neighbours. Jaccarino et. al [26] proposed a phenomenological model to take into account the exchange coupling at a solute site in the host matrix. He gave a modified Brillouin function to express the temperature dependence of reduced hyperfine field at the solute atom in terms of the reduced magnetisation $M(T)/M(0)$ of the host, and an exchange coupling parameter, ξ .

$$\frac{H_{hf}(T)}{H_{hf}(0)} = B_J \left[\frac{3J}{J+1} \xi \frac{M(T)/M(0)}{T/T_C} \right] \quad (3.10)$$

$$\text{where} \quad B_J(x) = \frac{2J+1}{2J} \coth \frac{2J+1}{2J} x - \frac{1}{2J} \coth \frac{x}{2J} \quad (3.11)$$

For $\xi = 1$, the reduced hyperfine field follows the same tempera-

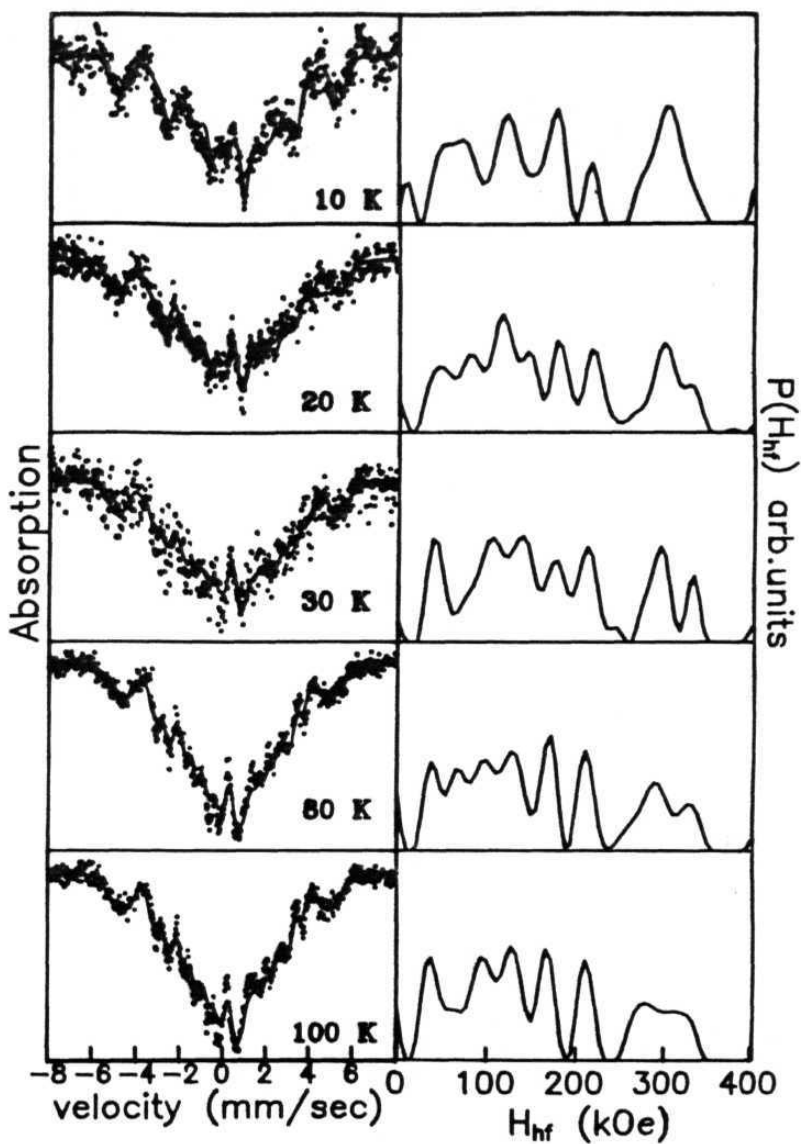


Fig.3.11. Mössbauer spectra and their hyperfine field distributions (calculated using model-independent Le Cœur program) at different temperatures for $\text{Fe}_{21}\text{Mn}_9\text{Si}$ alloy.

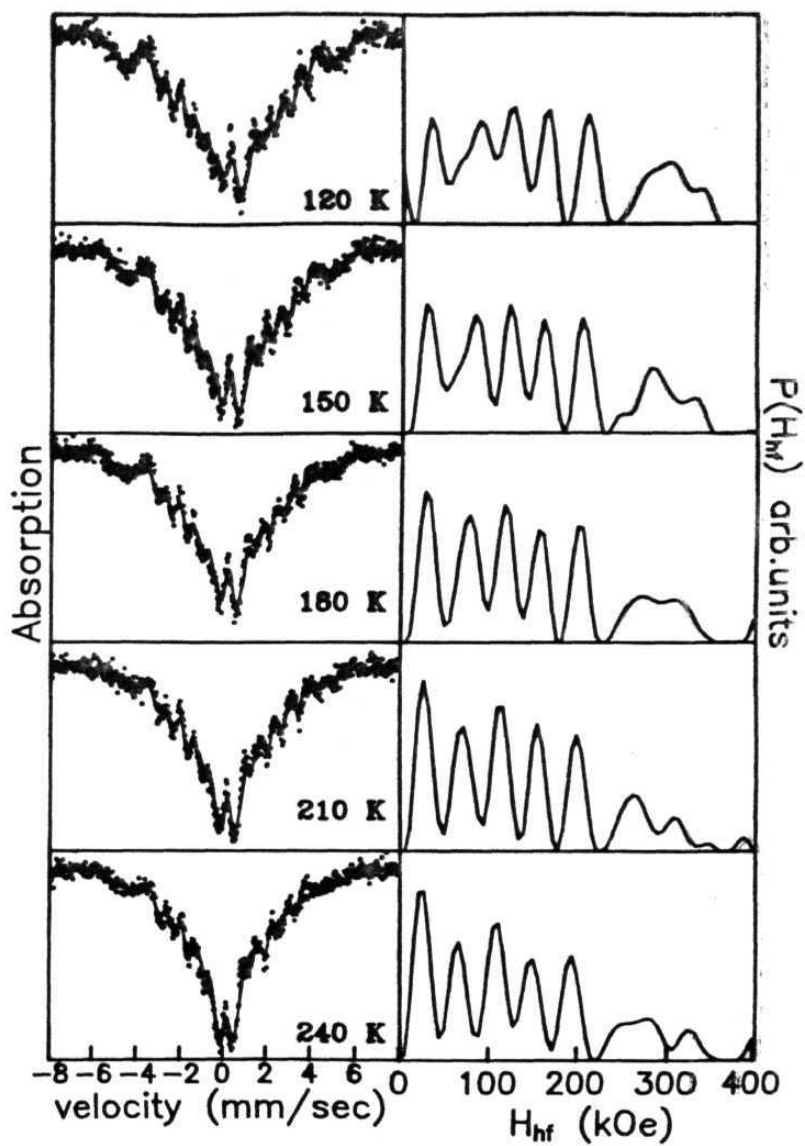


Fig. 3.11. Continued.

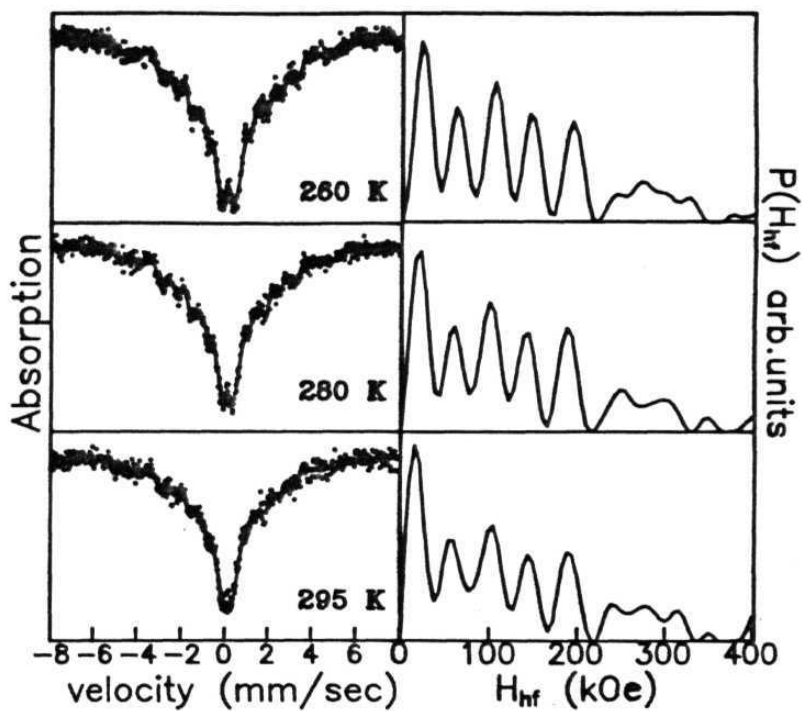


Fig.3.11. Continued.

ture **dependence** as the host magnetisation whereas for $\xi < 1$, the reduced hyperfine field decreases faster than the host magnetisation. This model gave a very good description of hyperfine field at impurity Fe atoms in nickel and manganese hosts [27]. The difference in temperature **dependence** of hyperfine field at Fe(A,C) site for different number of Mn near neighbours can be described by an extension of this model, if we choose different values of the coupling parameter, ξ , for the different configurations. Fig. 3.12 shows the fits to the hyperfine field data using **Eq. 3.10**. The reduced hyperfine field for the **configuration** with 8 Fe near neighbours was used to represent the reduced **magnetisation**.

For the Fe(AC) **configurations** with no manganese neighbours we get $\xi = 1$, whereas for **configuration** with more Mn neighbours ξ decreases and we get $\xi = 0.4$ for the **configuration** with the largest number of Mn neighbours ($n = 4$). This provides a good **evidence** that Mn near neighbours to Fe sites decrease the effective exchange interaction at these sites. The small entropy change at T_C mentioned earlier is also consistent with this because there is a large thermal disorder at these sites and only a partial ordering of spins even much below T_C .

The average hyperfine field H_{hf} and the **isomer** shift correlation parameters A and B defined by [23]

$$\delta(H_{hf}) = A\bar{H}_{hf} + B \quad (3.12)$$

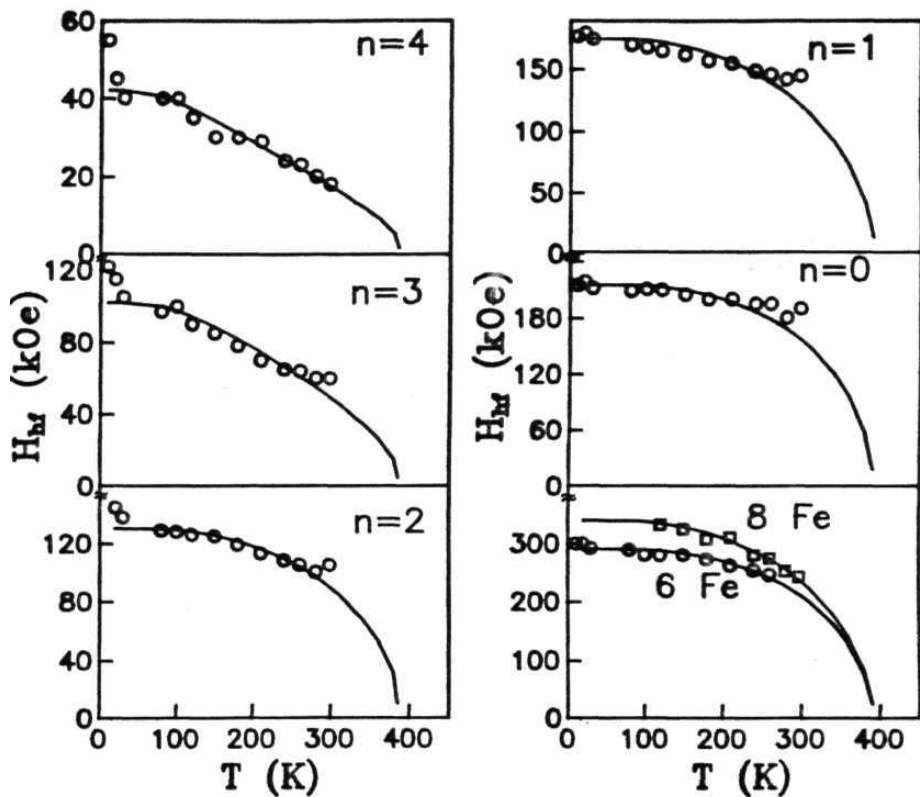


Fig.3.12. Temperature dependence of hyperfine field (H_{hf}) for Fe(AC) atoms having different number of Mn near neighbours (n), and Fe(B) atoms with 8 Fe and 6 Fe near neighbours for $Fe_{21}Mn_9Si$ alloy. The solid line indicates the fit to the data using Eg. 3.10.

are shown in Fig. 3.13 for the $x = 0.9$ alloy composition. This correlation was introduced in the field distribution fits carried out using the **Le Cæer** program. This enables us to determine a unique **isomer** shift value for each **configuration** and to follow its temperature dependence. Fig. 3.14 shows the temperature dependence of isomer shift for the $n = 0$ to 5 (number of **Mn** first neighbours to Fe(AC) sites) **configurations**. These plots show a pronounced increase below the re-entrant temperature. The physical origin of the isomer shift **increase** is because of either a loss of 3d charge or 3d spin at the neighbouring solute site [28]. But since we are observing a temperature dependent effect, the loss of 3d spin rather than 3d charge seems to be the likely cause for the isomer shift increase. Thus although the average hyperfine field does not show a change in behaviour at **T_{re}** (Fig. 3.13) the individual isomer shifts at the sites do show an effect related to the change in the near neighbour Mn moment. A slight increase in hyperfine field for individual Fe(AC) **configurations** having 2-4 Mn near neighbours can also be observed at **low** temperatures.

In the higher concentration region $x > 0.9$, the individual hyperfine field **configurations** become difficult to resolve and we have therefore fitted the spectra to only two sets of Gaussian distributions peaked at two different values. Initial estimates of the hyperfine field values were obtained from model independent **LeCæer** fits. The **Mössbauer** spectra and field distributions are shown in Fig. 3.15 and Fig. 3.16 for $x = 1.0$ and 1.2 compositions. For $x = 1.0$, the Gaussian field distribution peaked at the

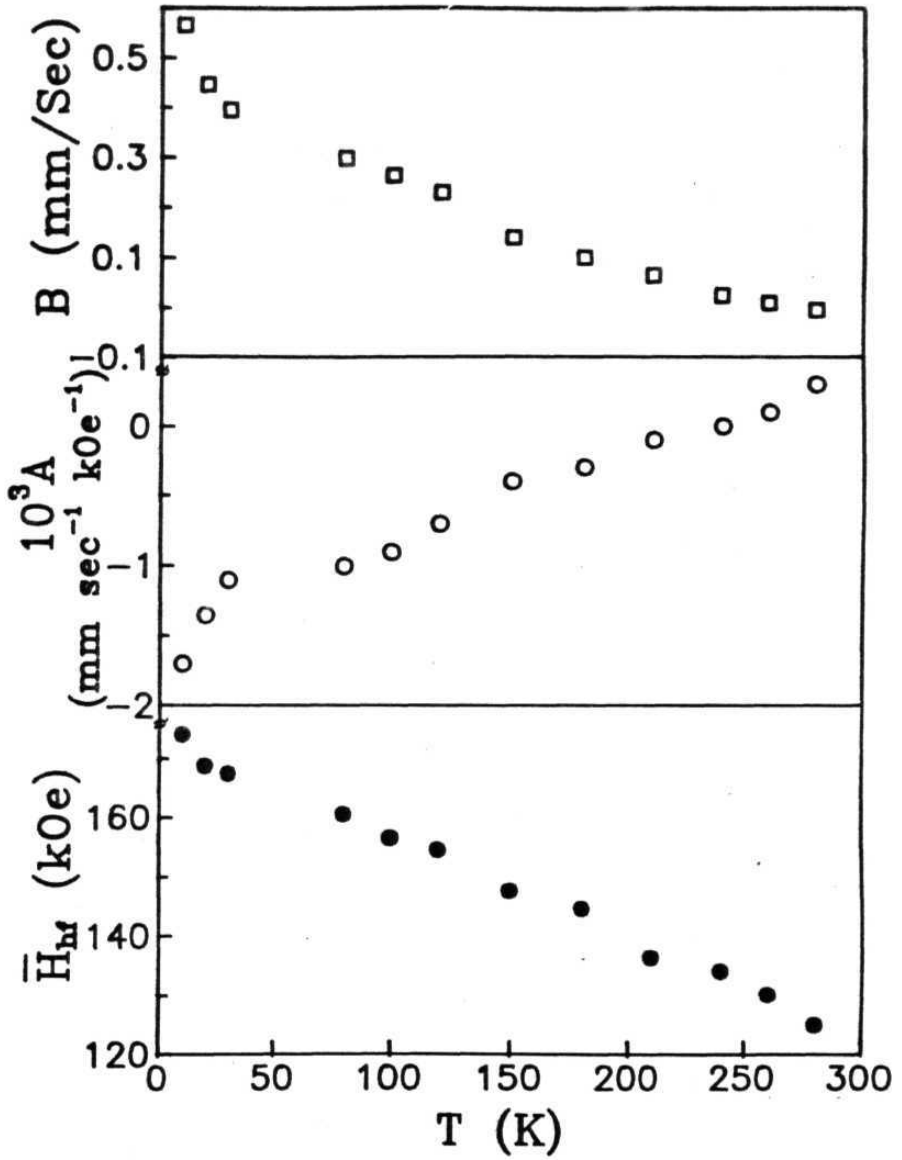


Fig.3.13. Variation of mean hyperfine field (H_{hf}) and isomer shift parameters (A and B defined in Eq. 3.12) with temperature (T) for $\text{Fe}_{21}\text{Mn}_{89}\text{Si}$ alloy.

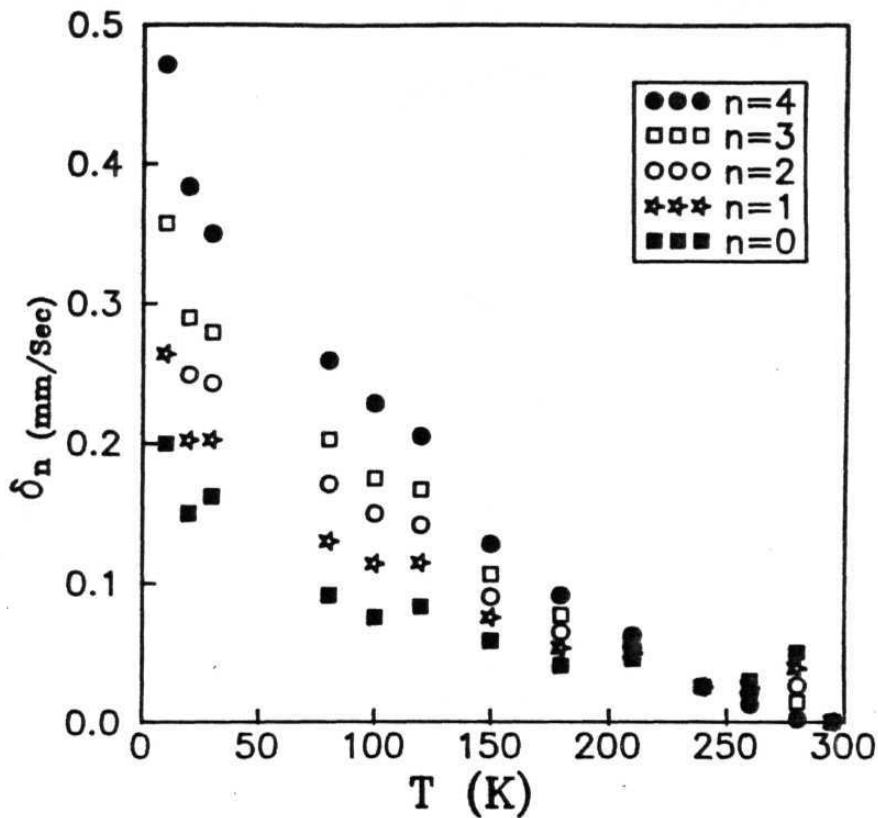


Fig.3.14. Temperature dependence of isomer shift (δ) for Fe(AC) atoms having different number of Mn near neighbours (n) for $\text{Fe}_{2-1}\text{Mn}_0$ gSi.

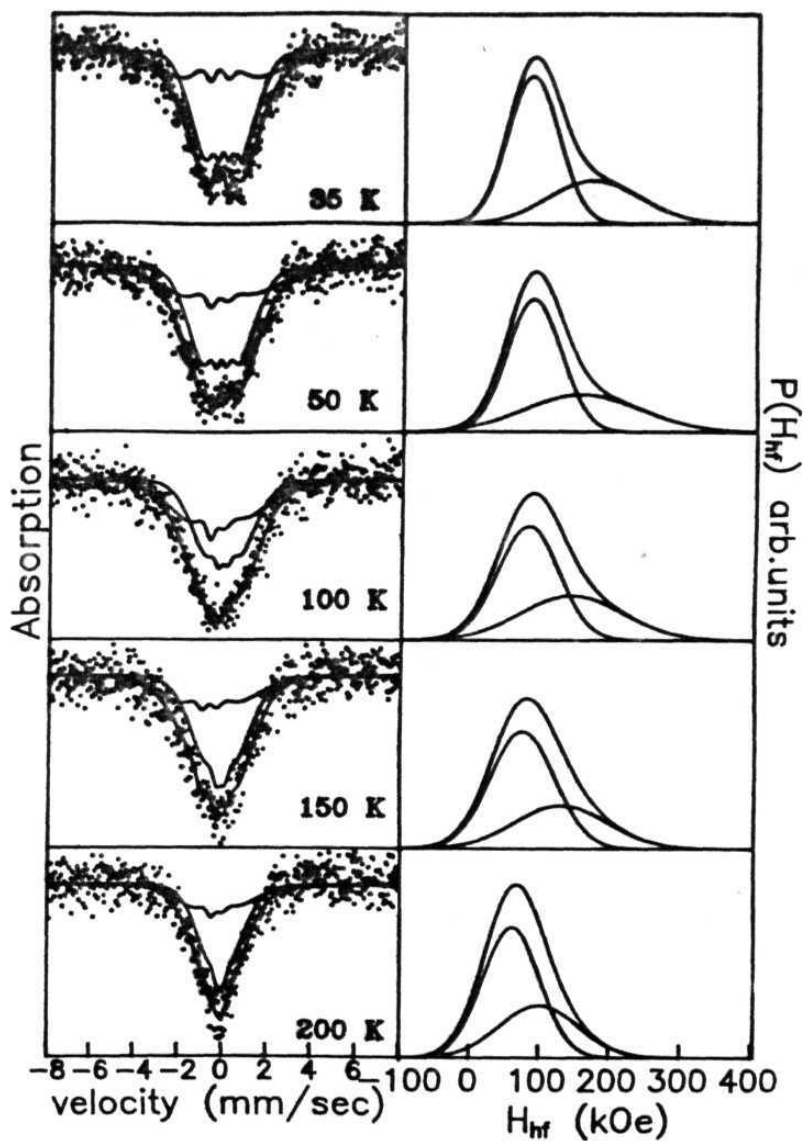


Fig.3.15. Mössbauer spectra and their hyperfine field distributions (fitted to two Gaussians) at different temperatures for Fe_2MnSi alloy.

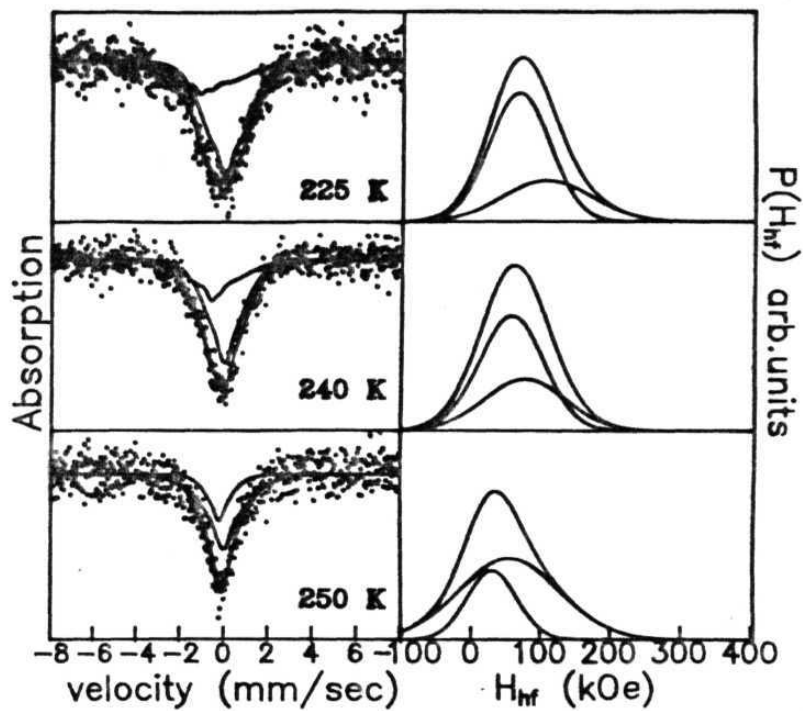


Fig.3.15. Continued.

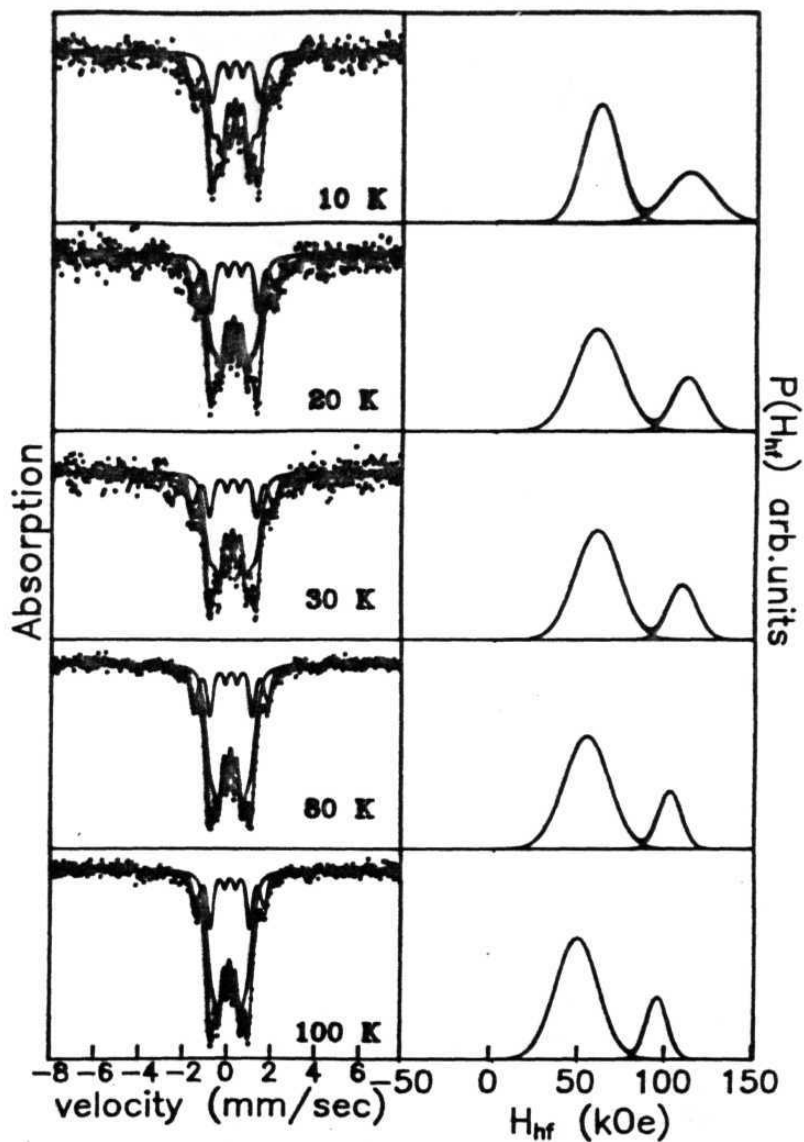


Fig.3.16. Mössbauer spectra and their hyperfine field distributions (fitted to two Gaussians) at different temperatures for $\text{Fe}_{18}\text{Mn}_{12}\text{Si}$ alloy.

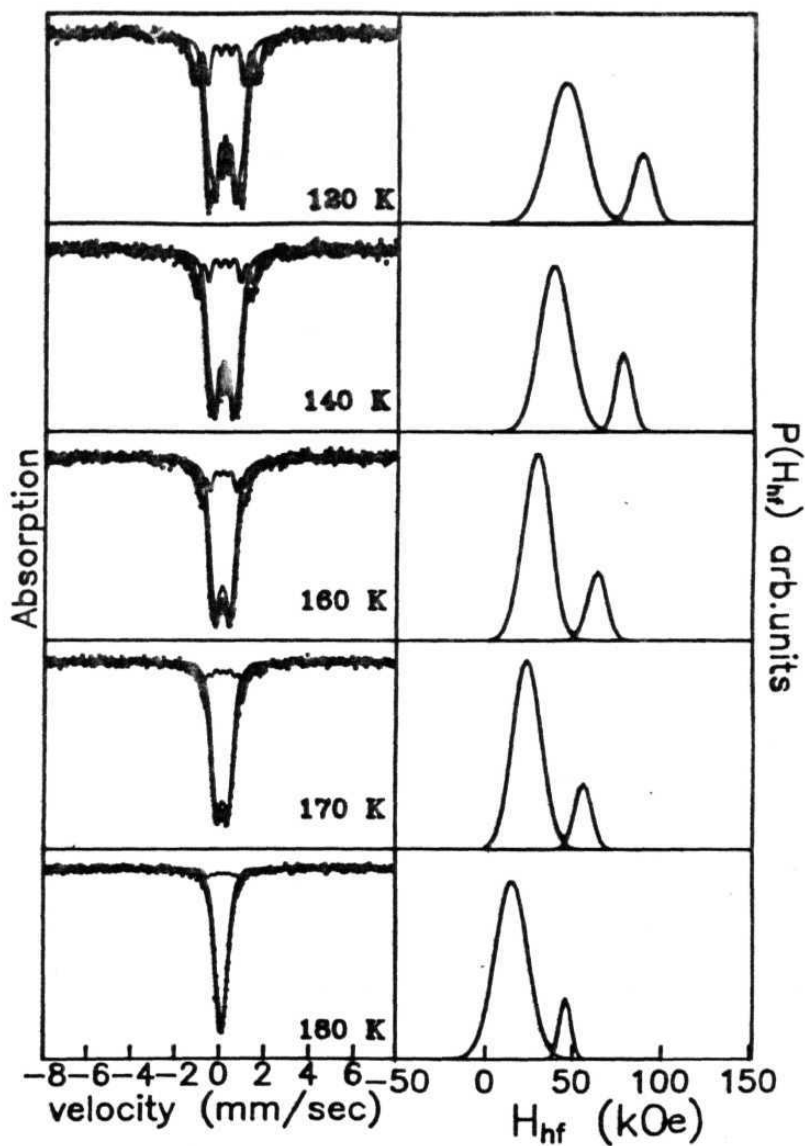


Fig.3.16. Continued.

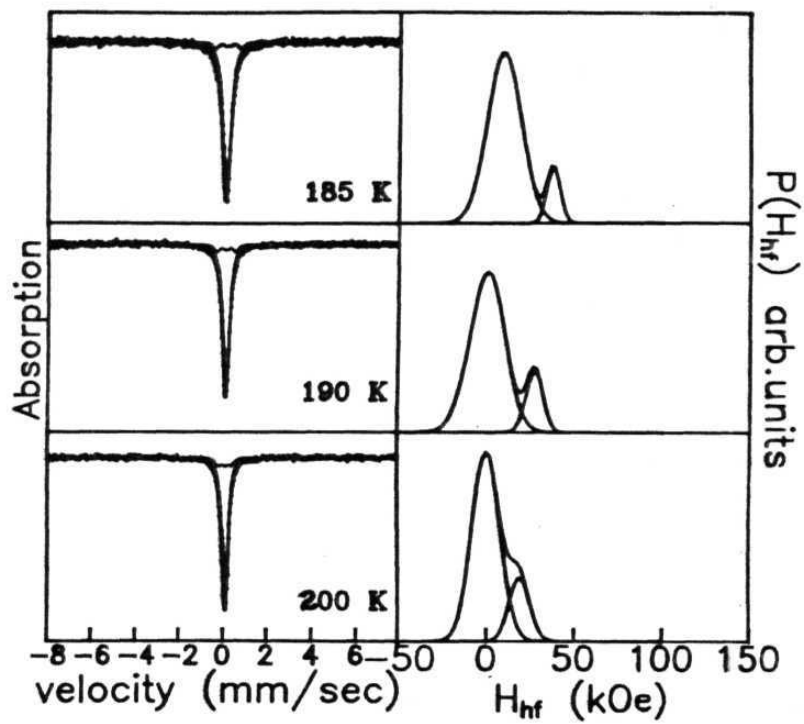


Fig.3.16. Continued.

higher value corresponds to $n = 2$ and the lower field value corresponds to $n = 3$ **configurations**. The fraction of these two configurations (as obtained from area under the two distributions) is consistent with the probability for substitution of the B sites by Mn atoms [24]. Similarly for $x = 1.2$ composition the higher field peak (lower fraction) corresponds to $n = 3$ configuration whereas the lower field peak (higher fraction) **corresponds** to $n = 4$ **configuration**. The temperature dependence of hyperfine fields and fraction of the peaks as shown in Figs. 3.17 and 3.18 respectively for $x = 1.0$ and 1.2 compositions.

3.4. DISCUSSION

The experimental findings of AC susceptibility, **FMR** and **Mössbauer** studies on the $\text{Fe}_{3-x}\text{Mn}_x\text{Si}$ alloys ($0.75 \leq x \leq 1.2$) together with earlier experimental results can be summarised as follows:

- (i) The transition at T_C is from a paramagnetic to ferromagnetic state.
- (ii) The temperature dependence of hyperfine field at the Fe sites with different Mn neighbours is strongly dependent on the first near neighbour Mn atoms. The exchange interaction between Fe and Mn is ferromagnetic but much weaker as compared to Fe-Fe exchange.
- (iii) The FMR linewidth begins to increase **just** below T_C and shows a behaviour characteristic of re-entrant spin glass systems.

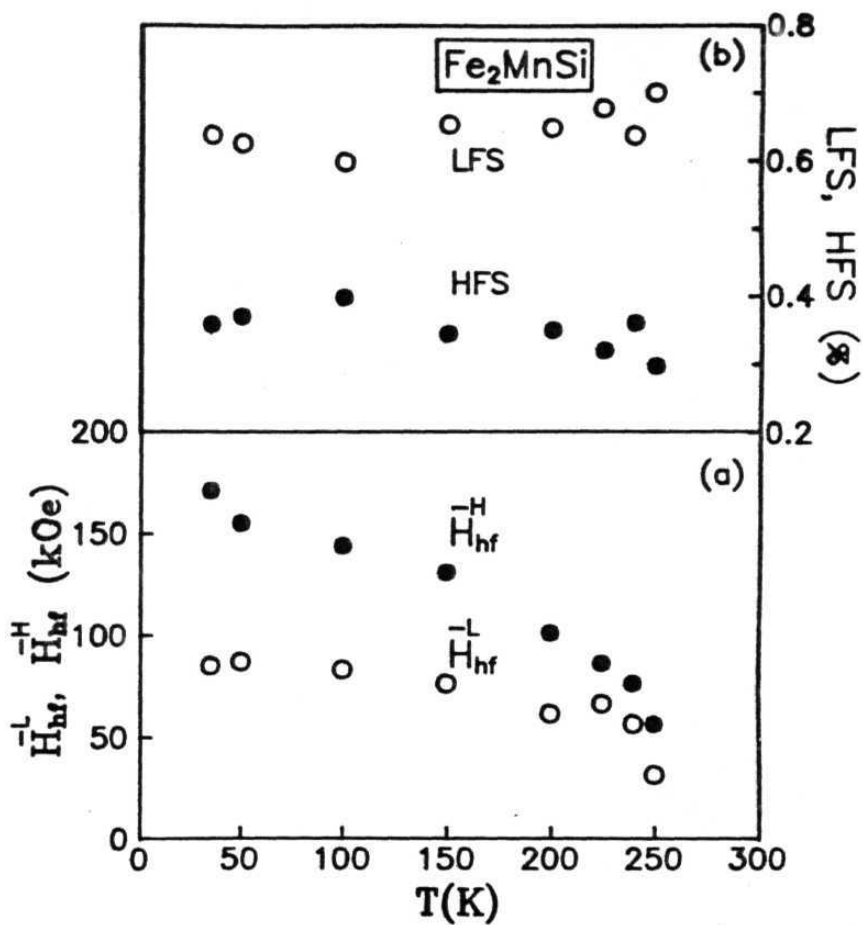


Fig.3.17 a. Temperature dependence of hyperfine field H_{hf}^L (lower field) and H_{hf}^H (higher field) for Fe_2MnSi alloy.
 b. Variation of area under low field peak (LFS) and high field peak (HFS) for Fe_2MnSi .

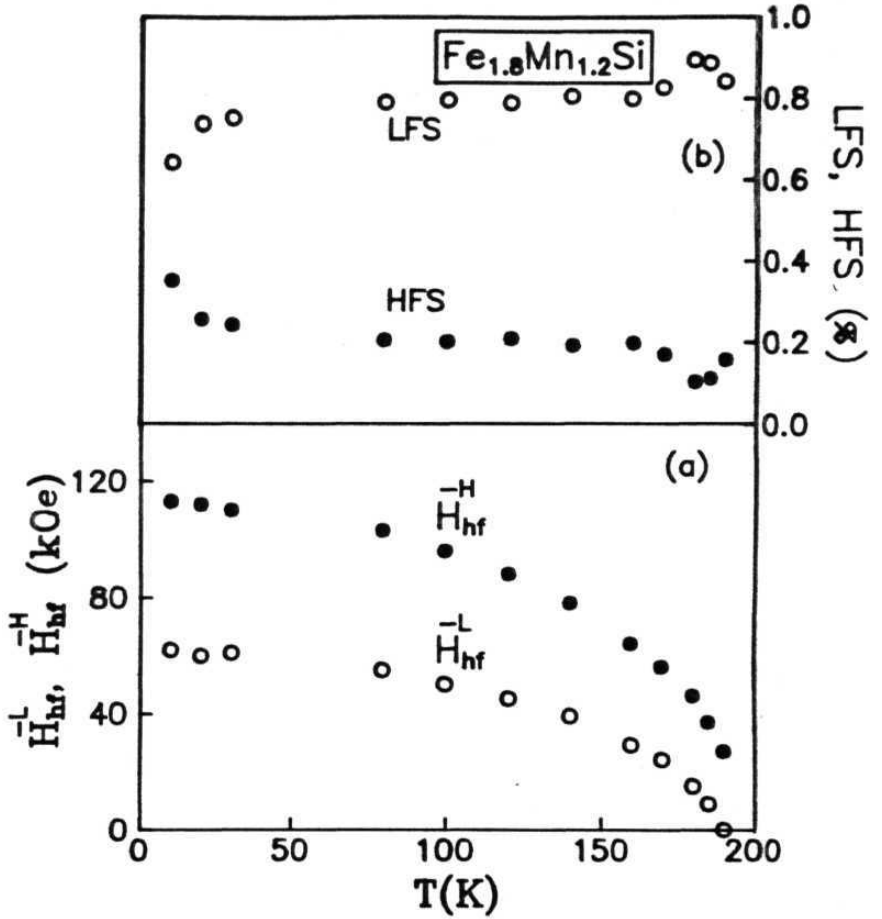


Fig.3.18 a. Temperature dependence of hyperfine field H_{hf}^L (lower field) and H_{hf}^H (higher field) for $Fe_{1.8}Mn_{1.2}Si$ alloy.
 b. Variation of area under low field peak (LFS) and high field peak (HFS) for $Fe_{1.8}Mn_{1.2}Si$.

- (iv) The system is described by localised exchange interactions upto fifth neighbour shells.
- (v) There is a lower transition temperature T_{RE} (which depends on Mn concentration) and there are pronounced changes in hyperfine interactions (magnetic hyperfine field and isomer shift behaviour) below this temperature.
- (vi) The exchange interactions between second neighbour manganese sites is weak and negative as measured from neutron inelastic scattering measurements [25] at low temperatures and gives rise to an **antiferromagnetic** ordering of moments at Mn sites as observed from neutron diffraction [29,30] determination of magnetic structure.

3.4. a. Effect of Preferential Substitution of Mn on Exchange Interactions

Based on these findings a simple model is proposed to describe the magnetic properties of the $Fe_{3-x}Mn_xSi$ alloy system. The DO_3 structure (Fig. 3.1) and the preferential occupation of B sites by Mn atoms in this structure gives rise to the following distinct magnetic behaviour of Fe and Mn moments occupying these sites (see Table 3.1)

- (i) Fe at (A,C) sites with a moment of $0.4 \mu_B$ having a first near neighbour environment of predominantly B site Mn moments ($\mu = 2 \mu_B$) and D site Si atoms ($\mu = 0$). These Fe moments have a weak local ferromagnetic first neighbour exchange with Mn neighbours which depends on the number of Mn neighbours and becomes **weaker with** more Mn neighbours.

- (ii) A very small number of Fe atoms at B sites are with a magnetic moment of $2 \mu_B$ and a first neighbour exchange with its Fe(AC) neighbours which is ferromagnetic. For Mn concentrations ($x \geq 1$) however these B sites are almost fully occupied by Mn and we need not consider the B site Fe atoms.
- (iii) Mn atoms of magnetic moment ($\cong 2 \mu_B$) at the B sites which have an antiferromagnetic exchange with the other B site Mn atoms and these Mn-Mn sites are third neighbours. Around $x = 0.75$ composition and beyond, the AC sites are also occupied by Mn and this gives rise to first neighbour Mn-Mn exchange also.
- (iv) A small number (less than number at B site) of Mn atoms of magnetic moment about $0.4 \mu_B$ at AC sites which have predominantly Mn and Si near neighbours at B and D sites.

A schematic representation of the various configurations is shown in Fig. 3.19. Since Fe atoms at (A,C) sites and Mn atoms at B sites are the majority atoms in the system we consider the magnetic behaviour of the system by a consideration of these sites. The behaviour of Mn (AC) and Fe(B) sites are also consistent with this behaviour.

3.4.b. Spin Canting and Magnetic Structure

Saslow and Parker studied analytically [31] a Heisenberg spin system on square and simple cubic lattice when antiferromagnetic bonds are substituted for ferromagnetic host nearest nei-

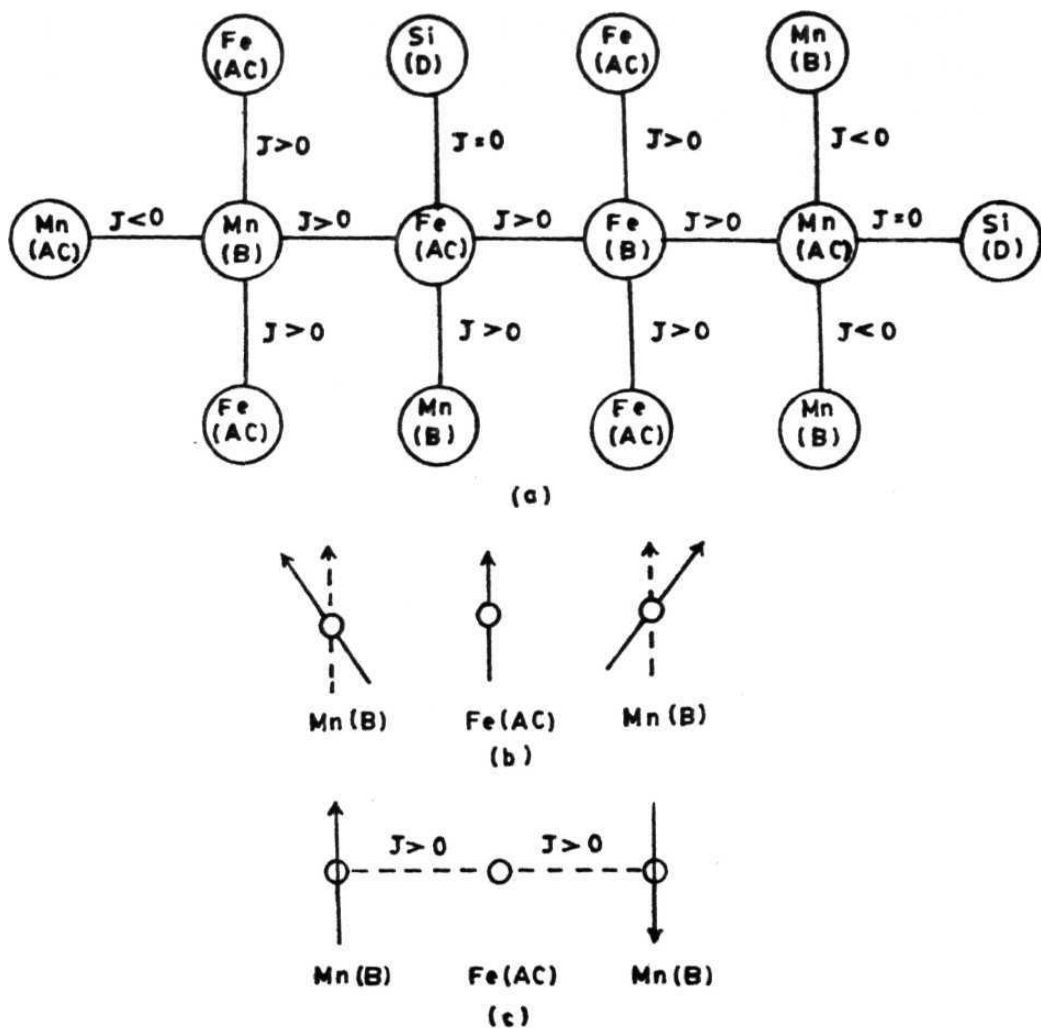


Fig.3.19 a. Schematic representation of Fe and Mn atomic moments on AC and B sites and their exchange interactions with neighbours.
 b. Canting of Mn spins at low temperatures.
 c. Frustration at Fe(AC) site due to antiferromagnetic ordering on B sublattice.

ghbcur exchange bonds. The same situation applies to **Mn(B)** sites where the ferromagnetic Mn-Fe bonds are substituted by antiferromagnetic **Mn-Mn** bonds. Saslow and Parker's results show that for such a system there is a spin canting at low temperatures but at higher temperatures there is ordinary ferromagnetic behaviour. In our system the other site viz. the Fe(AC) site has always a ferromagnetic exchange with Fe or **Mn** neighbours and it is only the Mn(B) site which shows a canting at low temperatures. Fig. 19b depicts the magnetic structure in the canted state. This canted spin structure is also physically understandable in terms of the frustration that sets in at the Fe(A,C) site. For an **anti**-ferromagnetic ordering at **Mn(B)** sublattice, the ferromagnetic Fe-**Mn** exchange interaction, gives a conflicting Fe(A,C) ordering due to the two **Mn(B)** neighbouring spins (Fig. 19c). The canting of Mn spins as shown in Fig. 19b gives a stable ground state for the system. The neutron diffraction data of Yoon and Booth [3,29] are also consistent with this Mn spin canting as they observed an antiferromagnetic component on the B sublattice perpendicular to the magnetisation direction. Yoon and Booth observed additional superlattice lines from spins in other planes but no superlattice reflection from (1/2,1/2,1/2) planes which are also expected for antiferromagnetic spin structures in **(111)** planes.

We therefore associate the lower transition temperature to a spin canting of the Mn moments and the magnetic phase diagram is shown in Fig. 3.20. It has also been predicted in all models for re-entrant spin glasses [7-9] that a replica symmetry breaking state (marked by onset of irreversibility) is obtained at low

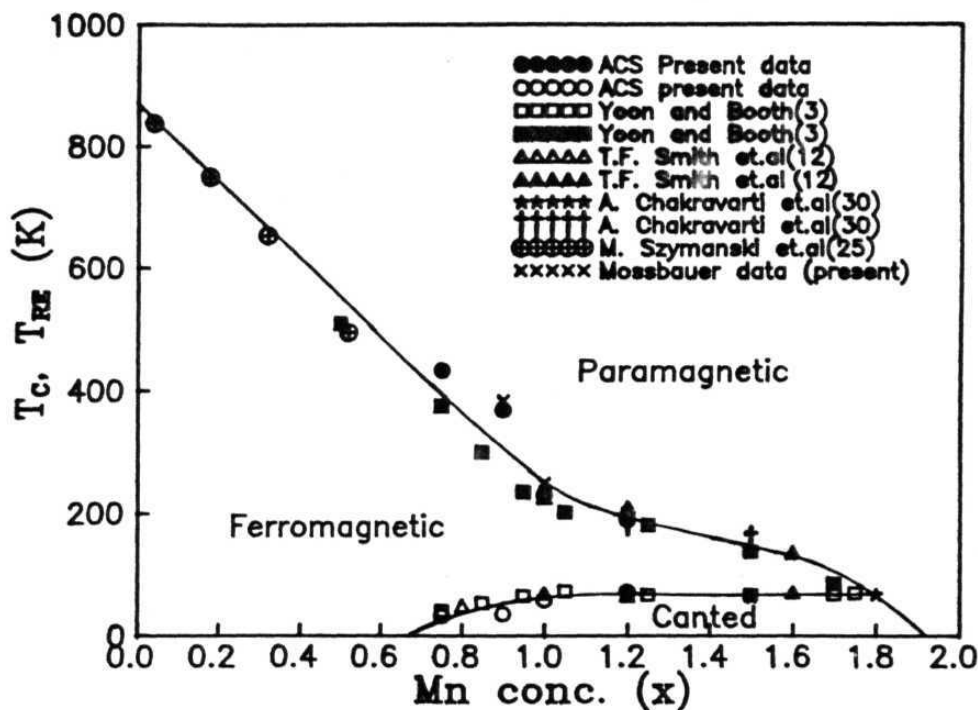


Fig.3.20. Magnetic phase diagram for $\text{Fe}_{1-x}\text{Mn}_x\text{Si}$ alloy system.

temperatures **below** the canted state. A careful external field **de-**pendent study is required to confirm this for our system but the hyperfine fields do show an increase at low temperatures (Fig. 3.12) and suggest a re-entrant phase formation.

3.5. CONCLUSIONS

In conclusion we find that a combined AC susceptibility, **FMR**, and Mossbauer effect study of the complex **Fe_{1-x}Mn_xSi** **magne-**
tic alloy system shows that there is a strong effect of near neighbour environment on the exchange interactions and corresponding magnetic behaviour of the system. AC susceptibility and magnetization studies show magnetic transitions clearly at two temperatures (**T_C** and **T_{RG}**) whereas FMR studies show a spin glass type increase in linewidth just below ferromagnetic **T_C**. Mossbauer hyperfine magnetic field and **isomer** shift variations from site to site depending on Mn neighbours suggest the importance of near neighbour effects. A magnetic structure consisting of canted Mn spins due to **antiferromagnetic** Mn-Mn exchange interactions is suggested.

REFERENCES

- [1] O. Becknan and L. Lundgren in "Ferromagnetic **materials**", Vol. 6 (edited by **K.H.J. Buschow**, North-Holland, Amsterdam, 1991) p. **264**.
- [2] V.A. Niculescu, T.J. **Burch**, J.I. Budnick, J. **Magn. Magn. Mater.** 39, **223(1983)**.
- [3] S. Yoon and J.G. Booth, J. Phys.:F7, 1079(1977).
- [4] T.J. Burch, J.I. Budnick, V.A. Niculescu, K. Raj and T. Litrenta, Phys. Rev. **B24**, **3866(1981)**.
- [5] J.T.T. **Kunaran** and C. Bansal, Solid State **Commun.** 69, 779(1989).
- [6] T. Goto, A. Kashiwakura and H. **Ido**, J. **Appl. Phys.** 69, 4636(1991).
- [7] M. Gabay and G. Toulouse, Phys. Rev. Lett. 47, 201(1981).
- [8] **W.M. Saslow** and G. Parker, Phys. Rev. Lett. 56, 1074(1986).
- [8] **I.A.** Campbell and S. Senoussi, Phil. Mag. **B65**, 1267(1992).
- [10] M.L. Spano and S.M. Bhagat, J. Magn. Magn. Mater. **24**, 143(1981).
- [11] L.D. Rakers and Paul A Beck, Phys. Rev. B36, 8622(1987).
- [12] T.F. Smith, G.K. Bristow, C.V. Boughton and P.R. Hudson, J. **Phys.F: Met. Phys.**, 101, 2867(1980).
- [13] S.N. **Kaul** and V. Siruguri, J. Phys.: Condense Matter 4, 505(1992).
- [14] S.N. Kaul, J. Phys.: Condense Matter 3, 4027(1991).
- [15] F. Reefer, "**Encyclopedia** of Physics", Vol. XVIII, ed. H.P.J. **Wojn** (Springer, **Berlin**, 1966) p. 1.
- [16] J. Mathon and E.P. **Wohlfarth**, **Proc. R. Soc.** A302, 409(1968).

- [17] **S.N. Kaul** and P.D. Babu, Phys. Rev. **B50**, 0308(1894).
- [18] D.J. Webb and **S.M. Bhagat**, J. Magn. Magn. Mater. 42, **109(1984)**.
- [19] S.M. Bhagat, D.J. Webb and M.A. Manheimer, J. Magn. Magn. Mater. 53, 209(1985).
- [20] M.B. Stearns, Phys. Rev. 129, **1136(1963)**.
- [21] B. **Fultz**, Z.Q. Gao and H. **Hamdeh**, Hyp. Inter. 54, 521(1990).
- [22] Z.Q. Gao and B. Fultz, Phil. Mag. B67, 787(1993).
- [23] B. Fultz, Z.Q Gao, H. Hamdeh and S.A. Oliver, Phys. Rev. B49, 6312(1994).
- [24] J.G. Booth in "Ferromagnetic materials", Vol.4 (edited by E.P. Wohlfarth and **K.H.J. Buschow**, North-Holland, Amsterdam, 1988) p. 211.
- [25] M. **Szymanski**, H. **Jankowski**, L. Dobrzynski, A. **Wisniewski** and S. Bednarski, J. Phys.: Condense Matter 3, 4005(1991).
- [26] V. Jaccarino, **L.R. Walker** and **G.K. Wertheim**, Phys. Rev. Lett. 13, 752 (1964)
- [27] M.B. Stearns and J.M. Norbeck, Phys. Rev. **B20**, 3739 (1979).
- [28] S. Yoon and J.G. Booth, Phys. Lett. 48A, 381(1974).
- [29] **K.R.A. Ziebeck** and P.J. Webster, Phil. Mag. 34, 973(1976).
- [30] A. Chakravarti, R. Ranganathan, **A.K. Raychaudhuri**, J.T.T. **Kunaran** and C. Bansal, Solid State **Commun.** 77, 17(1991).

CHAPTER 4

SITE SUBSTITUTION BEHAVIOUR AND SOLUBILITY LIMIT IN $Fe_{3-x}Cr_xSi$ ALLOYS

4.1. INTRODUCTION

In chapter III, it was discussed how addition of Mn to Fe_3Si in the quasi-binary system $\text{Fe}_{3-x}\text{Mn}_x\text{Si}$, gave rise to changes in magnetic ordering behaviour of the system. There was a wide concentration range $0 \leq x \leq 1.8$ in which these alloys were formed which enabled such a study. However for the Cr substituted system, $\text{Fe}_{3-x}\text{Cr}_x\text{Si}$, the situation is not so favourable and there is a limited composition range for which single phase alloys are formed in this quasi-binary system. Moreover there are conflicting evidences for the maximum concentration (x) of Cr for which there exist single phase alloys. Anderson and Jette [1] reported single phase structure upto $x = 1$, whereas Niculescu and Budnick [2] observed an extra phase beyond $x = 0.5$. Similarly the site occupation of Cr in the A, B, C or D sites is also not well understood. Earlier neutron scattering data [3] for $\text{Fe}_{2.88}\text{Cr}_{0.12}\text{Si}$ alloy showed a preference of B site by Cr similar to that of Mn and V. Although Cr magnetic resonance was not observed in Cr based alloys, the Fe(B) site NMR data were similar to those of Mn and V based alloys and this also gave a preferential B site occupation by Cr. However recent measurements [4] have been interpreted on the assumption that Cr substitutes randomly at all the three Fe sites viz. A, B, and C, although there was also some evidence [5] that twice as many Cr atoms enter B sites as compared to A or C sites.

This chapter discusses ^{57}Fe Mössbauer spectroscopy studies carried out in $\text{Fe}_{3-x}\text{Cr}_x\text{Si}$ system prepared in the composition

range $0 \leq x \leq 1.0$ to understand the site substitution behaviour and solubility limit of Cr in this alloy system.

4.2. EXPERIMENTAL AND DATA ANALYSIS PROCEDURE

Alloys of composition $\text{Fe}_{3-x}\text{Cr}_x\text{Si}$ in the concentration range $0 \leq x \leq 1$ were prepared by arc **melting**. Requisite quantities of **4N** purity iron, chromium and silicon powders were mixed and pressed into pellets. They were melted under argon atmosphere in an arc furnace **with** a water cooled copper hearth. Repeated melting was done to ensure homogeneity. Typical weight loss in melting process was 5 percent. The alloy ingots were homogenised at 800°C for 4 days after sealing them in quartz tubes under a pressure of 10^{-4} torr. A part of the homogenised alloys were made into coarse powder by filing and subsequently made into finer powder by grinding in mortar and pestle. The powders were annealed in vacuum sealed quartz tubes (10^{-4} torr) for 4 days at 400°C . Mossbauer absorbers having natural Fe content of **25 mg/cm²** were prepared from alloy powders after mixing with boron nitride.

The samples were characterised by powder diffraction on a Siefert Isodebyeflex Model 2002 X-ray **diffractometer** using **CuK α** radiation. Mossbauer spectra were recorded on a **μP** based spectrometer [6] in transmission geometry. A ^{57}Co in Rh matrix source was used.

For $x = 0$ alloy, the **Mössbauer** spectrum was fitted using a stripping procedure [7]. The spectrum consists of two resolved six line patterns and the six line pattern due to the lowest field is about double the intensity of the pattern due to the higher field. The detailed analysis of the spectra using the stripping procedure is as follows: In the first **step**, the approximate value of the outer field was estimated by a visual **inspection** of the experimental spectrum and the spectrum corresponding to this field was subtracted from the overall experimental spectrum to get a single stripped spectrum corresponding to the lower field. This was least square fitted to a six line pattern to get the line positions, widths and intensities of the spectrum. In the second step, the spectrum generated for the inner field using the parameters obtained in the first step was subtracted from the experimental spectrum to get the stripped spectrum for the outer field alone. This was again least square fitted to get the fitted parameters for this outer field. The spectrum generated for the outer field using the fitted parameters in step 2 was once again subtracted from the experimental spectrum to get the spectrum for the inner field. This was least square fitted to get improved estimates of parameters for the inner spectrum. These improved parameters were used to get the stripped spectrum for the outer field. This procedure was continued till the best fit parameters were obtained. Finally, the two stripped spectra were combined and the complete fitted spectrum for the inner and outer fields was generated. The fitted spectrum for $x = 0$ using this stripping procedure is shown in Fig. 4.1.

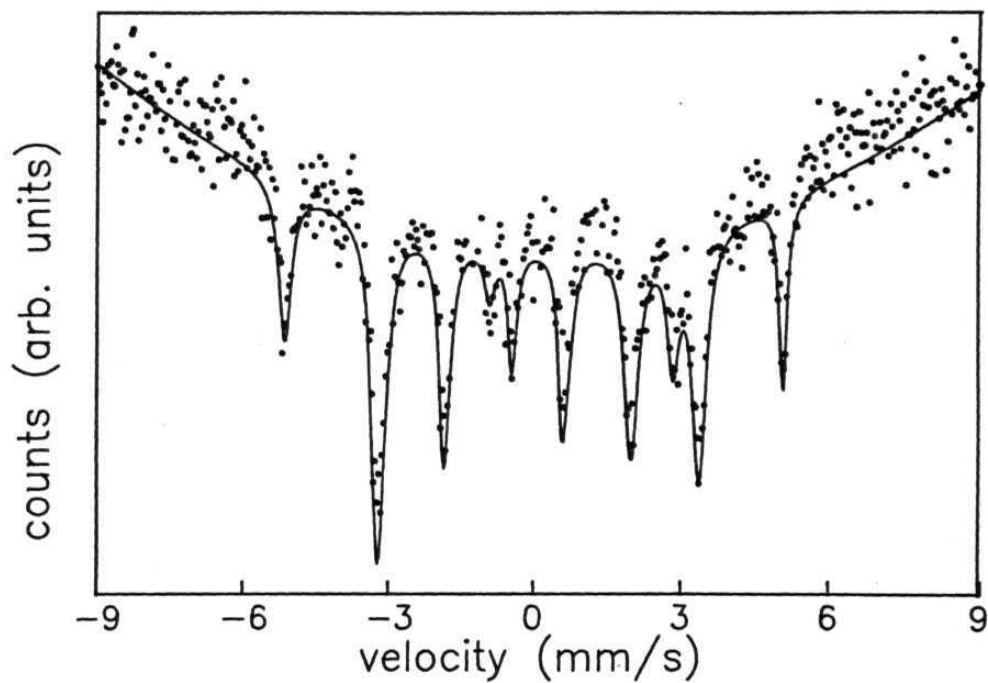


Fig.4.1. The complete fitted spectrum for Fe_3Si using the stripping procedure as discussed in Section 4.2.

The spectra for alloys with Cr additions are **more** complex and more than two unique fields are indicated. These spectra were first fitted using a model independent field distribution program [8]. This field distribution consists of peaks at various field values and was fitted to Gaussian field distributions at each of the peaks. Approximate center of the Gaussians, their standard deviations and intensities are therefore known. A field **distribu-**tion consisting of sum of these Gaussians in the form [7,8]

$$P(H) = \sum_{i=1}^n a_i \exp - \left[\frac{1}{2} (H - H_i)^2 / \sigma_i^2 \right] \quad (4.1)$$

with H_i , a_i and σ_i **representing** the central field, intensity, and standard deviation respectively is then assumed to be the field distribution to fit the **Mössbauer** spectra. The parameters H_i , a ,
2

and σ are then optimised by minimising χ^2 employing a grid **search** method. 4 to 5 Gaussian peaks were required to fit the **spectra**. Besides these parameters for the Gaussians, the following additional parameters were also optimised [9].

- i) The intensity ratios of the component lines in the form 3:b:1:1:b:3
- ii) The Lorentzian linewidth of the component lines (Γ).
- iii) Parabolic correction to the base line (**AQ**).
- iv) Correlation between **isomer** shift and hyperfine field (**GIS**).

Table 4.1 shows the final values of these parameters.

Table 4.1. The final values of parameters b , Γ , AQ , and GIS as functions of x in $Fe_{1-x}Cr_xSi$.

x	b	Γ (BB/S)	AQ	GIS (BB/s/kOe)
0.25	2.0	0.261	5.7e-02	5.60e-04
0.50	2.0	0.275	5.5e-02	5.56e-04
0.60	2.0	0.285	4.5e-02	5.56e-04
0.75	2.0	0.271	5.1e-02	5.22e-04
0.90	1.8	0.271	7.0e-02	5.29e-04
1.00	1.9	0.268	6.9e-02	5.64e-04

4.3. RESULTS AND DISCUSSION

4.3.a. Solubility Limit of Cr

The X-ray powder diffraction patterns for alloys of composition $0.5 \leq x$ could be indexed to a single phase of cubic unit cell ($a = 5.67 \text{ \AA}$) whereas for $x > 0.5$ a two phase mixture was observed. The patterns were indexed to two cubic phases with $a = 5.69 \text{ \AA}$ and $a = 4.57 \text{ \AA}$. The latter phase is identified as a **Cr₃Si** rich phase as the lattice parameter is very close to the reported value [10] for **Cr₃Si** ($a = 4.56 \text{ \AA}$). Our results thus show that a single phase region exists in Cr substituted system upto $x = 0.5$ only in agreement with the results of Niculescu and Budnick [2] who also tried to correlate the solubility limit and average electron concentration. From the analysis of the limits of formation of **DO₃** structure in **Fe_{1-x}(Si,Al)_x** alloys, a value of average electron concentration per atom (e/a) in the range $6.25 \leq e/a \leq 7.5$ was indicated for formation of single phase alloys of the type **Fe_{3-3x}T Si_x**. For Cr alloying, the average electron concentration of outer (s+p+d) electrons changes from 7 in **Fe₃Si** to 6.75 in **Fe_{2.5}Cr_{0.5}Si**. The average electron concentration for Mn and V substituted alloys at the solubility limit ($x = 1.8$ and $x = 1$ respectively) are 6.55 and 6.25. Thus this simple picture of considering all the spd electrons outside the closed shell for computing average electron concentration and associating a critical value of average electron concentration at the solubility limit, appears to break down. This point is further discussed while looking at our isomer shift data.

4.3.b. Hyperfine Fields and Local Environment Model

The Mössbauer spectrum of Fe_3Si fits well with two well defined hyperfine field values of 314 kOe and 202.6 kOe using the stripping procedure outlined earlier. These field values are consistent with the well ordered DO_3 structure of Fe_3Si and the higher hyperfine field value is attributed to Fe(B) site which has 8 Fe(A,C) first neighbours and a magnetic moment of $2.2 \mu_B$ [11]. The lower field is due to AC sites which have 4 Fe(B) and 4 Si(D) neighbours and a magnetic moment of $1.35 \mu_B$. The area ratio observed for the (AC) to (B) site fields from the Mössbauer spectra corresponding to these fields is 66.3:33.7 which is in excellent agreement with the ratio expected for two equivalent AC sites to one B site in ordered Fe_3Si .

For $x = 0.25$ composition ($\text{Fe}_{2.75}\text{Cr}_{0.25}\text{Si}$) the spectrum obtained after stripping the B site or AC site field is not a simple six line spectrum expected for a unique field (Fig. 4.2a and 4.2b). This indicates the presence of field contributions besides the ones present in fully ordered DO_3 . The spectra for this composition and for higher Cr concentration alloys were therefore analysed using a field distribution consisting of Gaussian peaks centered at various fields. The field distribution derived by fitting the spectrum (Fig. 4.2c) is shown in Fig. 4.2d and it consists of five Gaussian peaks. These can be understood if the substitution of Cr takes place preferentially at the B site. The highest field value of 287 kOe corresponds to the Fe(B) site and the other four fields corresponds to Fe(AC) sites which have

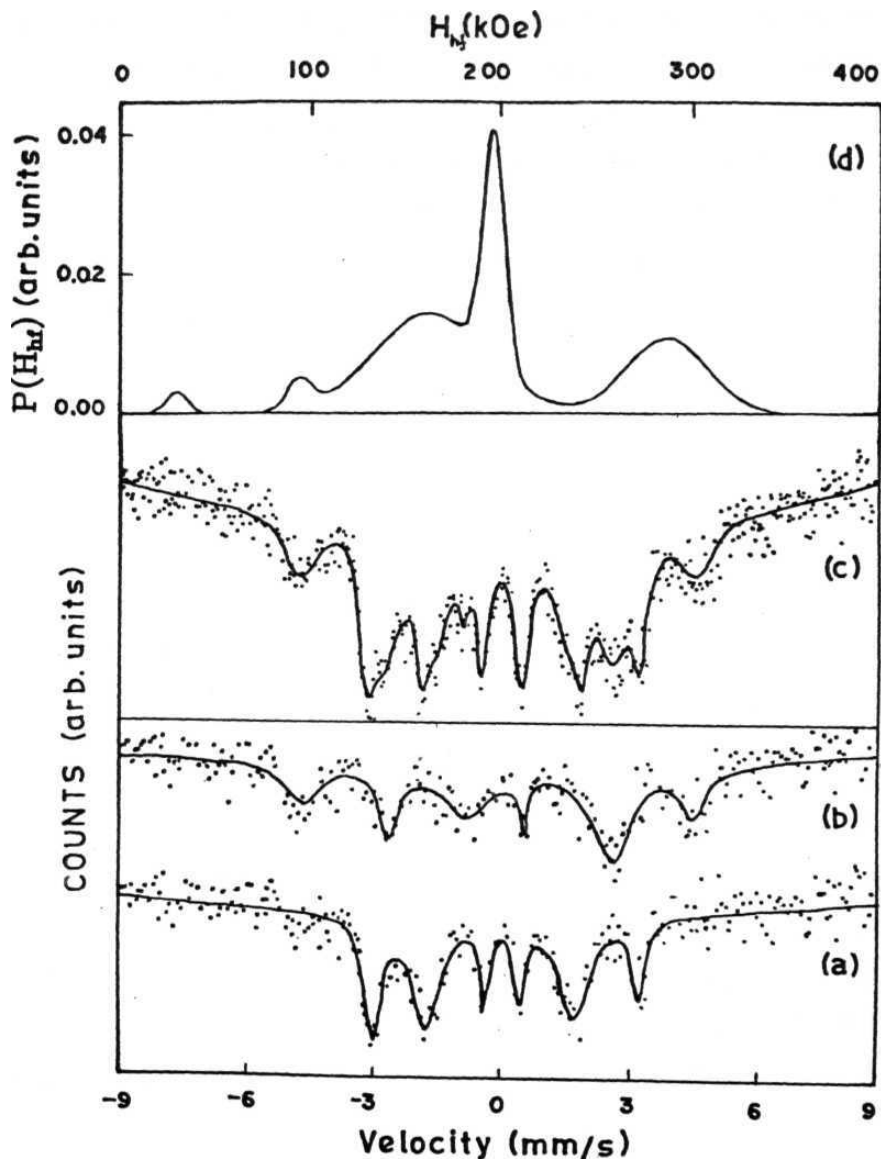


Fig.4.2. (a) and (b) are the residual spectra for $\text{Fe}_2\text{75Cr025Si}$ after stripping B and AC fields respectively. The Mössbauer spectrum fitted with a field distribution comprising of five gaussians is shown in (c) and the corresponding field distribution is shown in (d).

different near neighbour(nn) **configurations** due to substitution of Cr at the B site (Table 4.2). To understand the observed hyperfine fields in $\text{Fe}_{3-x}\text{Cr}_x\text{Si}$ alloys a local environment description was presented by **Niculescu et.al.,[12]**. The internal field at a site is assumed to arise from (i) the polarisation of s shells (inner s shells as well as **conduction s** electrons) and (ii) transferred conduction electron spin polarisation due to moments in the neighbouring shells. The first contribution is proportional to the on-site moment and it is further **assumed** that only the 1 nn shell contributes **significantly** to the second term and this is given by

$$H_{sp} = A_{4s} n p \langle \mu \rangle_{1nn} \quad (4.2)$$

where A_{4s} is the hyperfine coupling constant in units of kOe/μ_B , n is the number of 4s electrons and p is the polarisation of the 4s electrons due to the 1 nn moments. This approach has been used to explain the field behaviour at Fe(B), Fe(AC) and T sites in both Mn and V substituted system [12]. A self consistent **explanation** of the fields at B site as well as AC sites in $\text{Fe}_{3-x}\text{Cr}_x\text{Si}$ alloys can also be given based on this model. From the field values at Fe(B) site we first estimate the np value as defined in **Eq. 4.2** and then use it to determine the Fe(AC) fields for various nn **configurations**.

The first contribution to the Fe(B) internal field is proportional to the on-site Fe moment ($\mu_{Fe} [B] = 2.2\mu_B$). Using a proportionality constant of $93.18 \text{ kOe}/\mu_B$ [12] this contribution is

Table 4.2. Hyperfine fields and magnetic moments for different nn configurations in $\text{Fe}_{3-x}\text{Cr}_x\text{Si}$ alloys.

inn configuration	$\mu(\text{Fe}[\text{A},\text{C}])$ μ_B	$H(\text{Fe}[\text{A},\text{C}])$ kOe	$\mu_{\text{Fe } 93,18}$ kOe	$H_{\text{sp}}(\text{expt})$ kOe	μ_B	$H_{\text{sp}} = A_{4s} n_p \langle \mu \rangle_{\text{inn}}$ kOe
4 FeCB) 4 SiCD)	1,35	197	125,8	71,2	1,10	88,4
3 FeCB) 1 CrCB) 4 SiCD)	1,02	163	95,0	66,0	0,83	66,7
2 FeCB) 2 CrCB) 4 SiCD)	0,68	94	63,4	30,6	0,55	44,2
1 FeCB) 3 CrCB) 4 SiCD)	0,34	30	31,7	-1,7	0,28	22,5

205 kOe. The remaining contribution $H_{\text{meas}}[\text{Fe(B)}] \sim 205 \text{ kOe} = 82 \text{ kOe}$ arises from the second term H defined in Eg. 4.2. This contribution is proportional to the average 1 nn moment which comes from the 8 Fe(A,C) atoms. The Fe(A,C) moment depends on the number of Fe(B) neighbours only because Cr substitutes at B site with zero magnetic moment. A zero or very small Cr moment is supported by non-observation of Cr resonance in $\text{Fe}_{1-x}\text{Cr}_x\text{Si}_x$ also a very small internal field (10 kOe) at Cr in pure Fe [13]. This behaviour is very similar to that of V which also substitutes at B site with a small magnetic moment of 0.02μ [14]. For $x = 0.25$, the Fe(A,C) sites have on an average one Fe(B) near neighbour substituted by Cr(B) and hence a magnetic moment corresponding to 3 Fe(B) and [1Cr(B)+4Si(D)] near neighbours. The value of magnetic moment for this configuration is $1.02 \mu_B$ [11] and hence $\langle \mu_{\text{Fe(AC)}} \rangle_{1\text{nn}} = 1.02 \mu_B$ with $H_s = 82 \text{ kOe}$ and $A_{4s} = 51.78 \text{ MOe/s electron}$ [9] we get $n_p = 45 \times 10^{-3} \mu_B^{-1}$ using Eq. 4.2.

The other four hyperfine field values can now be assigned to Fe(AC) sites with different 1 nn configurations as shown in Table 4.2. With the proportionality constants obtained from B site fields the calculated AC site fields (column 7 of Table 4.2) show the correct trend and approximate agreement with experimental values (column 5 of Table 4.2).

The Mössbauer spectra and their hyperfine field distributions for alloys with $x \geq 0.5$ are shown in Fig. 4.3. The hyperfine fields for various configurations as a function of Cr concentration are shown in Fig. 4.4. For $x \geq 0.5$ the field values do not

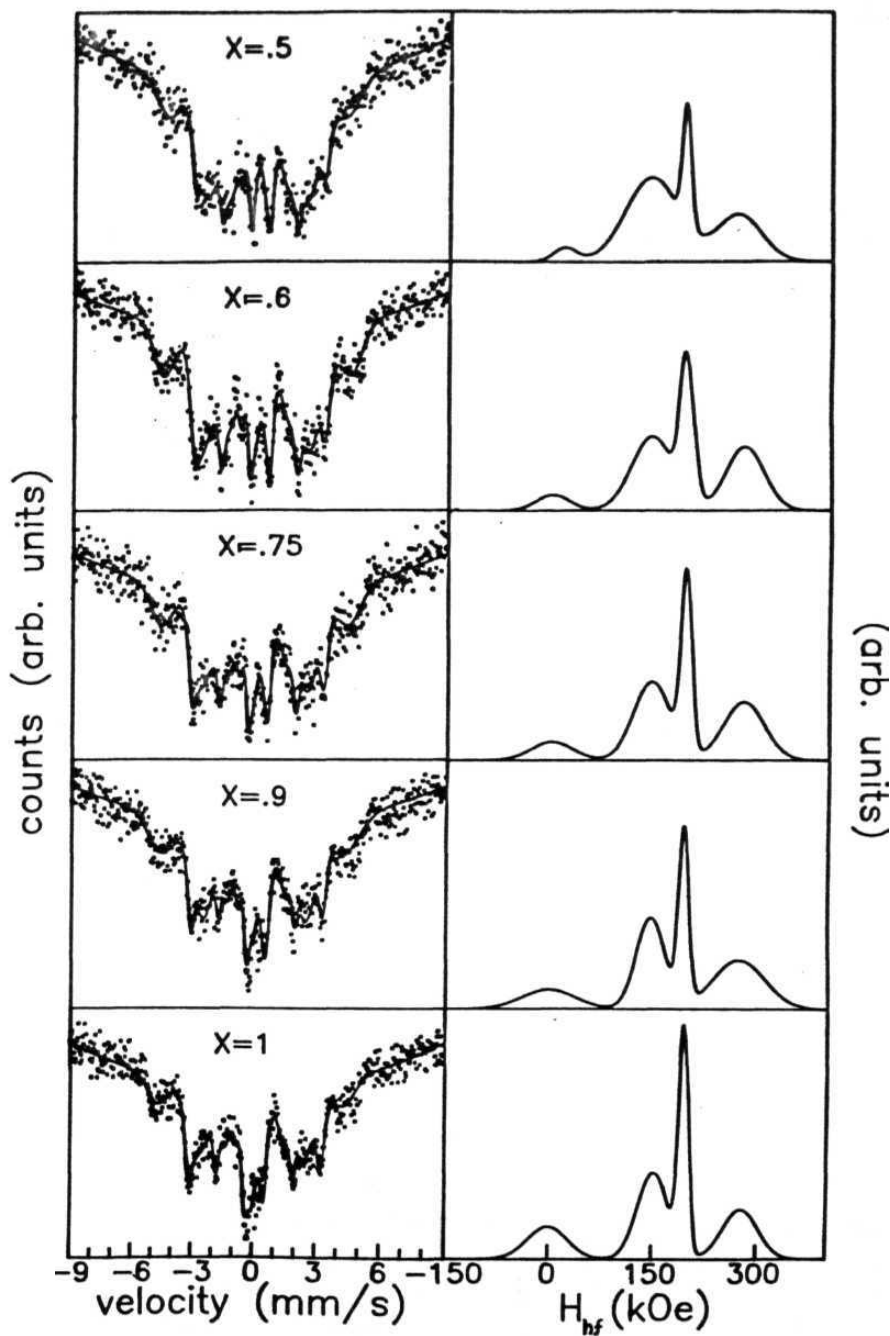


Fig. 4.3. Mössbauer spectra of $\text{Fe}_{3-x}\text{Cr}_x\text{Si}$ alloys for $x > 0.5$, fitted to a field distribution consisting of a **superposition** of four Gaussian peaks (Eq. 4.1) and the corresponding hyperfine field distributions.

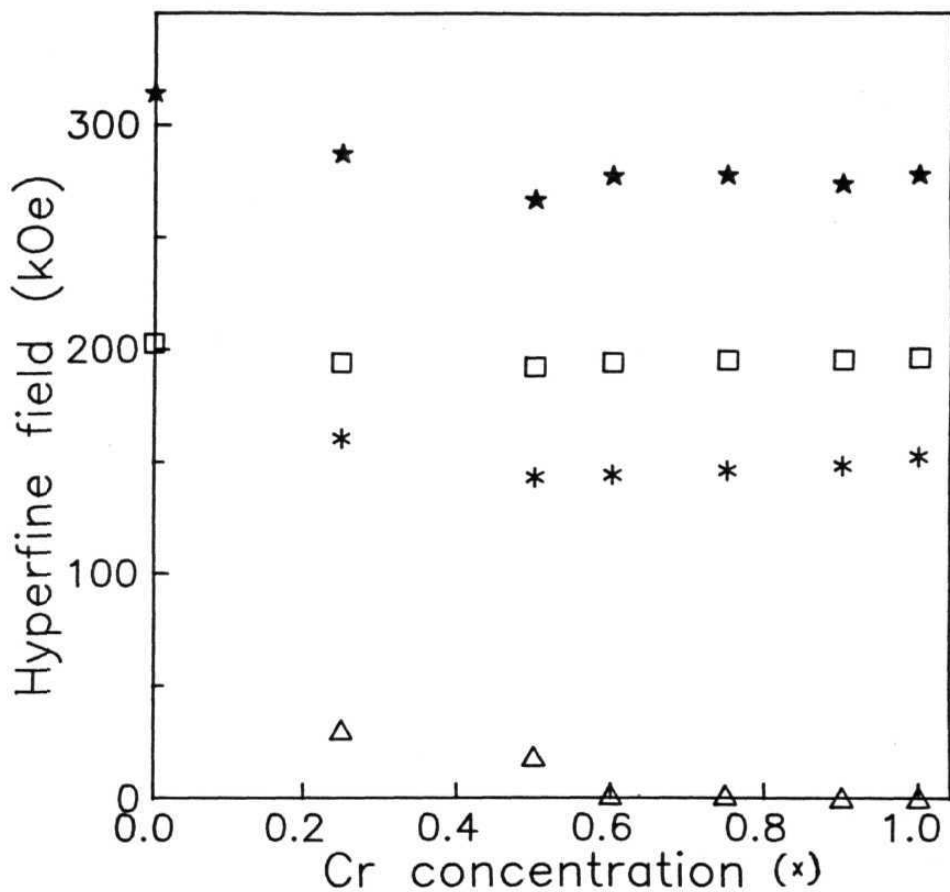


Fig.4.4. Variation of hyperfine fields with Cr concentration for different nn configurations (★: B site with 8 Fe nn, □, *, A: AC sites with 4 Fe 4 Si, 3 Fe 1 Cr 4 Si, and 1 Fe 3 Cr 4 Si nn respectively).

show a change with Cr concentration. The lowest field peak tends to a value of zero field for $x \geq 0.6$. This reflects the formation of a Cr solubility limited phase of approximate composition $x \approx 0.5$ in agreement with our observation of Cr_3Si phase in X-ray diffraction studies for alloys with $x \geq 0.6$. Fig. 4.5 shows the probability for the low field peak as a function of Cr concentration as obtained from the area under the low field peak in the field distribution (Fig. 4.3). There is an increase in the peak area with increase in Cr concentration. This peak includes contribution from Fe(AC) sites with 3 or 4 Cr neighbours also which would lead to Fe(AC) atoms with 1 and 0 Fe atoms. These sites are not distinguishable from dilute Fe dissolved in Cr_3Si phase and the increase in low field probability is therefore mainly associated with increased precipitation of Cr_3Si phase.

4. 3. c. Chemical Ordering and Kinetic Path Approach

The total probabilities for occurrence of Fe(AC) sites with 4 Fe and 3 Fe neighbours are similarly found by integrating the probability under the peaks for the fields of these configurations. The occurrence of these configurations depends on the type of chemical order present as well the effect of Cr substitution on the ordered state. The degree of order achieved in the sample is dependent on the vacancy concentration as well as its mobility. These quantities and their dependence at Cr concentration are not known. To obviate the need of these parameters, Gao and Fultz [15,16] adopted a "kinetic path" approach to study the kinetics of ordering in Fe_3Al . In this method, the development of one order

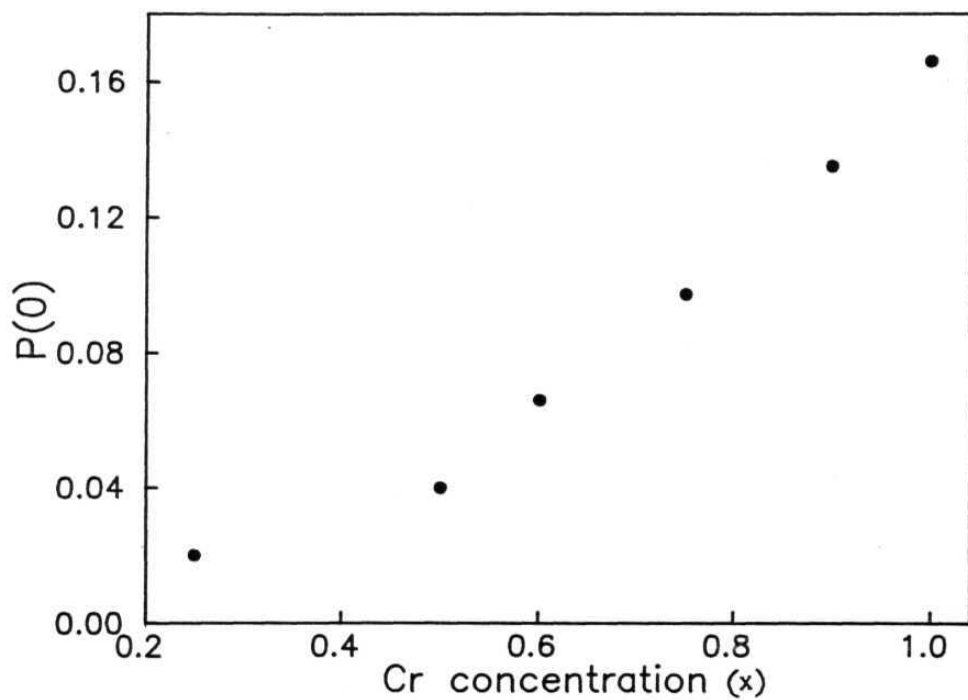


Fig.4.5. Probability of low field peak, $P(0)$, as a function of Cr concentration.

parameter against another is plotted and this "kinetic path" is independent of vacancy concentration and mobility. In our alloys of varying Cr concentration, the same ordering treatment was given to all the samples but different degrees of short range order is produced depending on concentration and mobilities of the vacancies present. Thus we can adopt the "kinetic path" approach to study the effect of Cr on ordering probability of 8 Fe 1 nn vs. 4 Fe 1 nn as obtained from the field distributions. These two 1 nn **configurations** correspond to Fe(B) (with 8 Fe(AC) neighbours) and Fe(AC) site (with 4 Fe and 4 Si neighbours), respectively, for a DO_3 ordered state. With Cr substituting at the B site the probability for occurrence 4 Fe 1nn's can be calculated using a binomial distribution for the nn **configurations** of Fe(AC) site

$$P(n) = {}^4C_n x^n (1-x)^{4-n} \quad (4.3)$$

The calculated probabilities based on Cr substitution at the B site in DO_3 structure is also shown in Fig. 4.6. The presence of DO_3 ordered structure for Cr substituted Fe_3Si alloys is therefore indicated.

The probability of 3 Fe nn of the (A,C) site Fe atoms, $P(3)$ is also calculated using Eg. 4.3 which is based on the assumption that Cr substitutes at the B site in the DO_3 structure. For $x = 0.25$ this probability should be about 1.3 times the probability for 4 Fe nn environment, $P(4)$. The experimentally observed probability for $x = 0.25$ is greater than 2. For $x = 0.5$ composi-

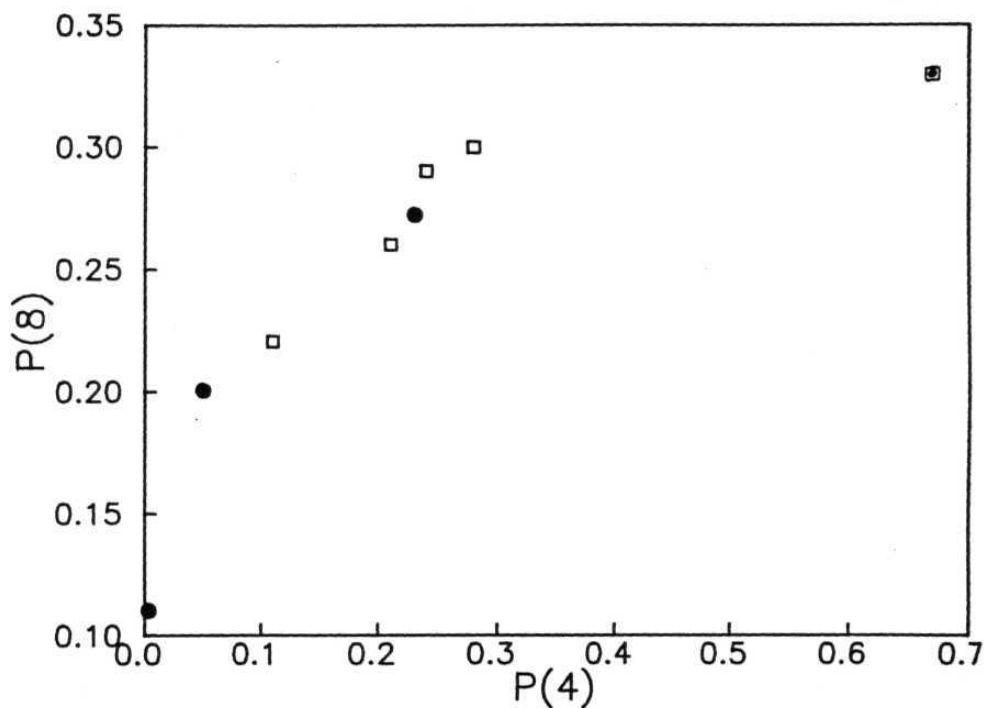
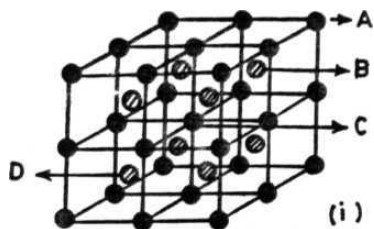


Fig.4.8. Probability of Fe(B) sites with 8 Fe 1nn, $P(8)$, vs. probability of Fe(AC) sites with 4 Fe 1nn, $P(4)$, obtained from the field distributions (a). The calculated probabilities based on Cr substitution at the B site in DO_3 structure are also shown (●).

tion also this ratio is greater than the expected value. The field distributions reported in [5] also show probabilities corresponding to fields of 5 and 6 Fe nn. This was attributed to the substitution of Cr at A and C sites also in addition to B sites. **However**, it is also possible to obtain these **configurations** if B2 or B32 order is present in the system. These ordered **structures** possible in the **bcc** alloys (Fig. 4.7a) were analysed by Richards and Cahn [17]. In the B2 structure the B and D sites have random occupancy of Fe and Si atoms whereas in the B32 structure the C and D sites are randomly occupied by Fe and Si atoms. Although the DO_3 structure is the equilibrium structure, the B32 structure has also been reported in Fe-20 at % Al [18] and also appears transiently during ordering in Fe-Al [15]. In the Fe-Cr-Si alloy system it has also been reported that the mobility of Si is reduced in the presence of Cr and well ordered DO_3 domains do not form [19]. The B32 structure can therefore arise in this Cr containing alloy system as this structure can also be viewed as a anti-phase domain boundary between DO_3 ordered domains [15].

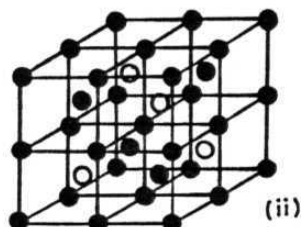
The nn **configurations** of the three ordered structures are shown in Fig. 4.7b. As compared to the DO_3 structure which has only 8 Fe nn and 4 Fe nn of Fe atoms, the other structures have large probabilities of 3 Fe or 5 and 6 Fe nn's. The probability of 3 Fe nn as observed in our field distribution can be attributed to the presence of B2 order or the 5 and 6 Fe nn **configuration** observed by [5] can also arise due to B32 type ordering.

A: Fe
B: Fe, Si
C: Fe
D: Fe, Si



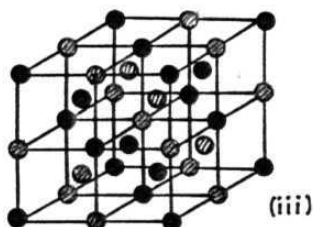
B2

A: Fe
B: Fe
C: Fe
D: Si



DO3

A: Fe,
B: Fe
C: Fe, Si
D: Fe, Si



B32

● Fe, ○ Si, ⊙ Fe or Si
(a)

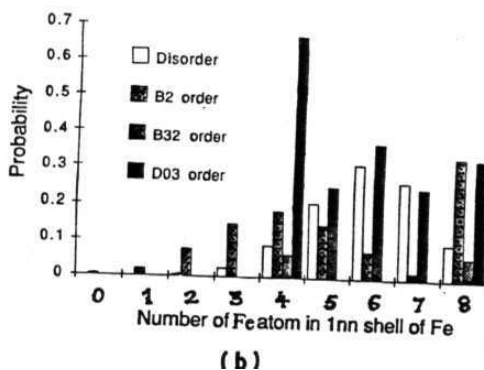


Fig.4.7 a. The possible ordered structures in **bcc Fe₃Si** (i) B2; (ii) DO₃; (iii) B32.

b. Calculated probabilities of Fe atoms with different **number** of Fe atoms in 1 nn shell for these structures.

4.3.d. Isomer Shift Behaviour

The observed isomer shift is also found to depend on the number of Fe neighbours of a given Fe atom (Fig. 4.8). The isomer shift values (relative to $\alpha\text{-Fe}$) fall into two groups. The isomer shift for Fe(AC) sites with 3 and 4 Fe neighbours lie in the region of 0.1 mm/sec whereas for Fe(B) site which has 8 Fe(AC) neighbours the isomer shift value is negative (-0.1 mm/sec). These are different from the values observed for Fe(AC) site (≈ 0.2 mm/sec) and Fe(B) site (0.1 mm/sec) for pure Fe_3Si . The decrease in isomer shift values for $\text{Fe}_{3-x}\text{Cr}_x\text{Si}$ alloys as compared

to Fe_3Si shows that the number of (3d+4s) electrons added per Cr atom is more than Fe and the average electrons per atom (e/a) increases as to reach to a solubility limit for low Cr concentration [2]. This accounts for the anomalous behaviour of Cr as compared to Mn and V substitutions which decrease the (e/a) values lower than Fe_3Si .

4.4. CONCLUSIONS

The solubility of Cr in $\text{Fe}_{3-x}\text{Cr}_x\text{Si}$ alloys is limited to $x = 0.5$ and a Cr_3Si phase is found beyond this composition. The hyperfine field values depend on the number of Fe first neighbours of a given Fe atom and the complex spectra are resolved into Gaussian peaks arising from each of these configurations. The fields for the sites can be consistently explained in terms of a local environment model proposed by Niculescu et.al. [12] to understand the general behaviour of $\text{Fe}_{3-x}\text{Cr}_x\text{Si}$ alloys. The probability of occurrence of various 1 nm configurations can be partly accounted for by assuming a preferential Cr substitution at the

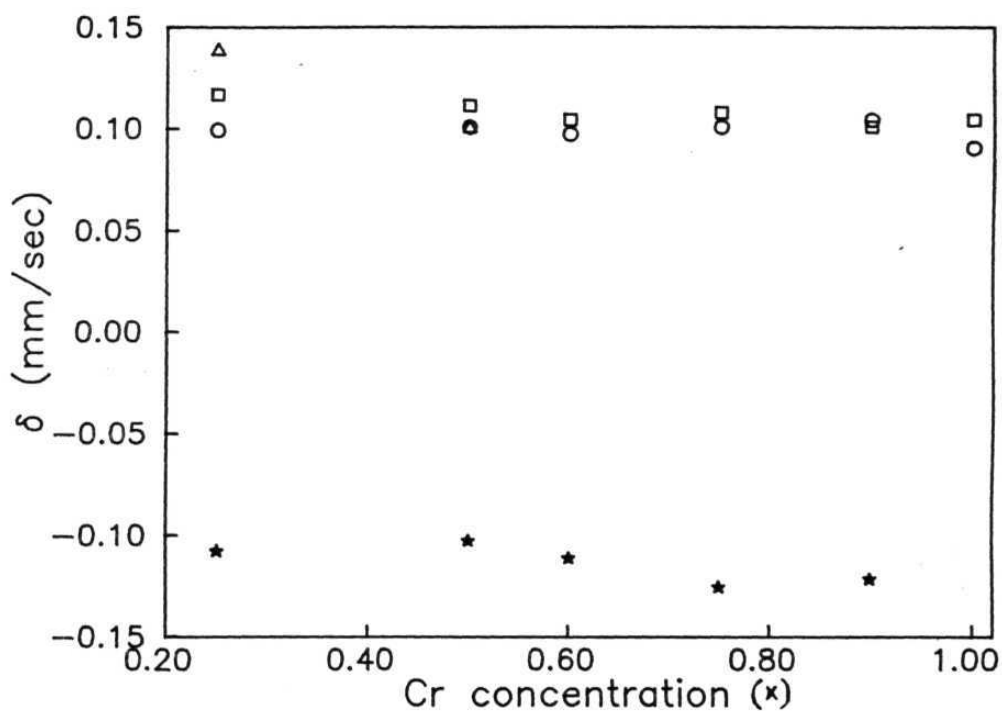


Fig.4.8. Dependence of isomer shift δ (relative to α - Fe) on Cr concentration for various nn configurations (* B site with 8 Fe, Δ - AC site with 2 Fe, \square - AC site with 3 Fe, o - AC site with 4 Fe).

Fe(B) site in the DO_3 structure but presence of other ordered structures besides DO_2 is also indicated. The **isomer** shift **behaviour** shows increase of e/a ratio with Cr addition which is different as compared to Mn and V and can lead to an approach to solubility limit for low Cr concentrations.

REFERENCES

- [1] **A.G.H.Anderson** and E.R.Jette, Trans. **Amer. Soc. Met.****24**, 375 (1936).
- [2] V.Niculescu and J.I.Budnick, Solid State **Commun.****24**, 631 (1977).
- [3] E.J.D.Garba and R.Jacobs, J. Phys.F: Met. **Phys.****16**, 1485 (1986).
- [4] J. **Waliszewski**, L. Dobrzynski, A. **Malinowski**, D. Satula, **K. Szymanski**, W. Prandl, Th. **Brückel** and O. **Schärf**, J. Magn. Magn. Mater. 132, 349 (1994).
- [5] D. Satula, **K. Szymanski**, L. Dobrzynski and J. Waliszewski, J. Magn. Magn. Mater. 119, 309 (1993).
- [6] J.T.T.Kumaran and **C.Bansal**, **Nucl. Instrum. Methods in Physics Research**, **B61**, 357 (1991).
- [7] J.T.T.Kumaran and C.Bansal, Solid State **Commun.****69**, 779 (1989), Solid State **Commun.****74**, 1125 (1990).
- [8] D.G.Rancourt and J.Y.Ping, **Nucl.Inst.Meth.** in Physics Research B58, 85 (1991).
- [9] J.Y.Ping, D.G.Rancourt and R.A.Dunlap, **J.Magn.Magn.Mater.****103**, 285 (1992).
- [10] E.A. Brandes (Ed.), Smithells metals Reference Book, 6 edition (Butterworth, London, 1983) **p.6**.
- [11] W.A.Hines, A.H.Menotti, J.I.Budnick, T.J.Burch, **T.Litrenta**, V.Niculescu and **K.Raj**, Phys. Rev.B13, 4060 (1976).
- [12] V.A.Niculescu, T.J.Burch and J.I.Budnick, J. Magn. Magn. Mater. 39, 223 (1983).

- [13] S.A. **Wedner**, L.Kerzthelyi and **J.A.Canneron**, J. Phys. **57**, 827 (1976).
- [14] **T.J.Burch**, **C.A.Weiler**, **K.Raj**, **J.I.Budnick**, **V.Niculescu**, **G.C.Papaefthymiou** and R.B.Frankel, J. Magn. Magn. Mater. **27**, 55 (1982).
- [15] **Z.Q.Gao** and B.Fultz, Phil. Mag. 67, **787** (1993).
- [16] **B.Fultz**, **Z.Q.Gao** and **H.Hamdeh**, Hyp. Inter.**54**, 521 (1990).
- [17] M.J.Richards and **J.W.Cahu**, Acta. Metall.**19**, 1263 (1971).
- [18] **W.Scheveika**, Mat. Res. Soc. Symp. Proc.**166**, 249 (1990).
- [19] **W.P. Wostrikow**, **W.J. Goldstein** and **A.A. Salvinska**, Fiz. Met. Metalloved, 61, 1144 (1986).

CHAPTER 5

EFFECT OF CHEMICAL ORDER ON THE MAGNETIC
PROPERTIES OF $Fe_{3-x}Mn_xAl$ ALLOYS AND KINETICS OF
ORDERING IN $Fe_{1.8}Mn_{1.2}Al$

5.1. INTRODUCTION

Al and Si are neighbours in the periodic table and as solutes in bcc Fe have many similarities. Equilibrium DO_3 order develops in both Fe_3Si and Fe_3Al . However the critical temperature for ordering is much higher in Fe_3Si (1105° C) as compared to Fe_3Al (550° C) and it is therefore easier to get disordered Fe_3Al by quenching and follow the changes in magnetic properties and hyperfine fields induced by chemical ordering. The Fe-Al phase diagram also has a region of B2 order between 550° C and 800° C at Fe_3Al composition. It was observed that at low annealing temperatures there was a tendency to develop B2 order as DO_3 order evolved [1-3].

Ternary additions to Fe_3Si have been studied extensively as discussed in Chapters 3 and 4 but there is relatively less experimental work done so far on ternary additions to Fe_3Al . Tuszynski et. al. [4] investigated disordered $Fe_{1-x}V_xAl$ alloys in the concentration range $0 \leq x \leq 0.8$. They observed a decrease of average hyperfine field, Curie temperature and average magnetic moment with x and a nonmagnetic state (at 300 K) was obtained for $x > 0.8$. From Mössbauer hyperfine field distributions the state of chemical order developed in $Fe_{2/3}V_{1/3-4x}Al_x$ was deduced to be B2 type for $x = 1$ and 1.4 and DO_3 for $x = 0.7$ composition [5]. In the Cr substituted alloy system $Fe_{3-x}Cr_xAl$, the hyperfine field was found to decrease non-linearly with Cr concentration and a quadratic dependence of hyperfine field on the number of nearest neighbour (nn) iron atoms was postulated [6].

The pseudo-binary alloy system **Fe₂ Mn Al** is also of considerable interest because of its possible applications as a **stainless steel** as well as its basic magnetic and structural properties that arise due to substitution of Fe by Mn in the binary **Fe₃Al** system. Several questions such as dependence of Fe moment on Mn substitution, formation of moment on Mn site, effect of Mn substitution on magnetic and chemical order in this alloy system, have been addressed and attempts are made to explain the **observed** behaviour of the alloy system. Previous experimental work has been carried out using Neutron diffraction, Magnetization, **NMR** and **Mössbauer** spectroscopic measurements. Magnetic diffuse neutron scattering in the **disordered** alloy system with Mn concentration upto 13.9 atomic percent showed that both Fe and Mn atoms have a localized moment ($\approx 2.2 \mu_B$) which decreases with increasing Mn concentration [7]. Further work on the system [8] was carried out after inducing atomic order by a heat treatment of 5 h at 575° C. The distribution of Mn on the three sublattices of **Fe₃Al** (as discussed earlier two of the sublattices A and C are equivalent, the others being designated as B and D) in the ordered state showed a preference of Mn for D and B sublattices which have predominantly Fe neighbours on AC sites, but the AC sites were also found to be occupied with half to one third concentration. The observed decrease of magnetic moment with increasing Mn concentration was explained by assuming that an increasing number of magnetic moments are oriented antiparallel to the resulting magnetic moment with increasing Mn content.

In a recent study [9] the magnetic properties of FeMnAl alloys were studied in the disordered phase and the magnetic phase diagram and hyperfine magnetic fields were explained by an extension of the site diluted **Ising** Model for the **Fe-Al** system wherein the addition of Mn was assumed to dilute the system **just** like **Al**.

In this work we study the $\text{Fe}_{3-x}\text{Mn}_x\text{Al}$ alloy system in a wide concentration range ($0 \leq x \leq 1.5$) both in the chemically ordered and disordered state and also report the kinetic approach to equilibrium from disorder to order for the alloy of composition $\text{Fe}_{0.8}\text{Mn}_{1.2}\text{Al}$ which shows dramatic changes in its magnetic properties as a result of chemical order-disorder.

5.2. EXPERIMENTAL

Alloys of composition $\text{Fe}_{3-x}\text{Mn}_x\text{Al}$ in the concentration range $0 \leq x \leq 1.5$ were prepared by arc melting. Requisite quantities of JMC Puratronic grade I iron powder, m3N7 purity manganese chips and m3N5 purity aluminium shots were taken. The alloys were prepared by arc melting under argon atmosphere in an arc furnace with a water cooled copper hearth. Melting was done repeatedly to ensure homogeneity. The typical weight loss in the **melting process** was about 5 X. The alloy ingots were homogenised at 1000°C for 48 hours after sealing them in quartz tubes under a pressure of **10** torr. Then the ingots were quenched from 1000°C in liquid nitrogen to get disordered alloys. A part of the homogenised and quenched alloys was filed into coarse powder and subse-

quently ground into finer powder in mortar and pestle. The powders were annealed in vacuum sealed quartz tubes ($\approx 10^{-4}$ torr) for 24 hours at 400° C to get the ordered samples. The Fe- $_{8}\text{Mn}_{12}\text{Al}$ powder was annealed at 300° C for different periods of time to study the kinetics of disorder-order transformation.

2

H6ssbauer absorbers with a natural Fe content of 25 mg/cm were prepared from the sample powders after mixing with boron nitride and pressing them into pellets.

5.3. RESULTS AND DISCUSSION

The compositions of the alloys prepared by us are shown in the phase diagram (Fig. 5.1) reported by Chakrabarti [10] for ternary FeMnAl alloys quenched from 1000° C. The powder X-ray diffraction patterns show the formation of single phase bcc alloys for composition upto $x = 1.2$ and a small amount of second phase in addition to the bcc phase for the alloy with $x = 1.5$ composition. For $x = 1.8$ composition the X-ray diffraction showed intense lines corresponding to the second phase. This phase was indexed to a close packed hexagonal(ϵ) phase with $c = 4.04$ Å, $a = 2.46$ Å. Although the equilibrium phase diagram of Chakrabarti [10] at 1000° C shows the β -Mn phase in this region, the ϵ phase has also been found for quenched FeMn and AlMn systems due to a martensitic transformation [11]. The lattice parameter in the bcc phase region does not show any change with Mn concentration which is in agreement with the observation of Alcazar et. al [9] and which is attributed to a similar size of Mn in relation to Fe.

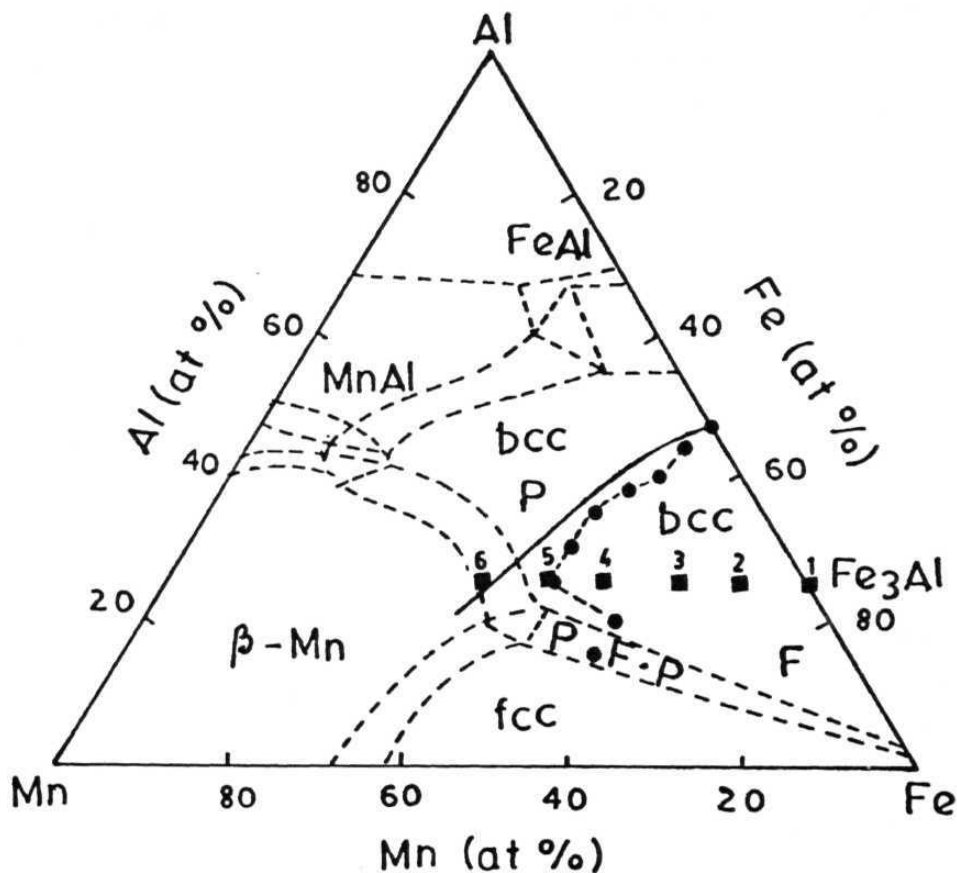


Fig.5.1. Phase diagram for disordered **Fe-Mn-Al** alloy system [9]. The solid squares 1 to 6 represent the samples in the present study ($\text{Fe}_{3-x}\text{Mn}_x\text{Al}$ for $x = 0, 0.3, 0.6, 0.9, 1.2, 1.5$). The solid line represents the ferromagnetic(F) to paramagnetic(P) boundary according to site diluted Ising model [9].

5.3.a. Hyperfine Fields in Disordered Alloys

Fig. 5.2. shows the room temperature Mössbauer spectra for disordered $\text{Fe}_x\text{Mn}_{1-x}\text{Al}$ alloys together with the magnetic hyperfine field distributions evaluated from the data by model independent analysis of Le Cœur and Dubois [12]. With increasing Mn concentration there is a shift in the field distribution towards lower hyperfine field values and an increase in the asymmetry of the distribution. The probability in the low field regions is seen to increase relative to the probability in high field region. The spectra are qualitatively similar to those reported earlier [9] but the decrease observed in our field distributions is slower as compared to the data of Alcazar et. al [9], who observed a large zero field component at $x = 1.0$ and a transition to paramagnetic state at $x = 1.2$ composition. This trend is more clearly seen in the average hyperfine field H_{hf} (Fig. 5.3) plotted as a function of Mn concentration together with the data of Alcazar et. al. The transition from ferromagnetic to paramagnetic state at room temperature is seen to occur at $x = 1.5$ composition. Alcazar et. al extended the site diluted Ising model earlier proposed by them to explain the magnetic properties of Fe-Al alloys [13]. Mn was assumed to produce a dilution of the concentration of magnetic Fe atoms similar to the effect of non magnetic Al in Fe-Al alloy system. The exchange interactions between Fe and Al or Fe and Mn were assumed to be zero. The calculated dependence of H_{hf} on Mn concentration (shown in Fig. 5.3a) shows a change to non magnetic state near $x = 1.6$. Although our data also show a change to non-magnetic state at $x = 1.5$ in agreement with this, the actual de-

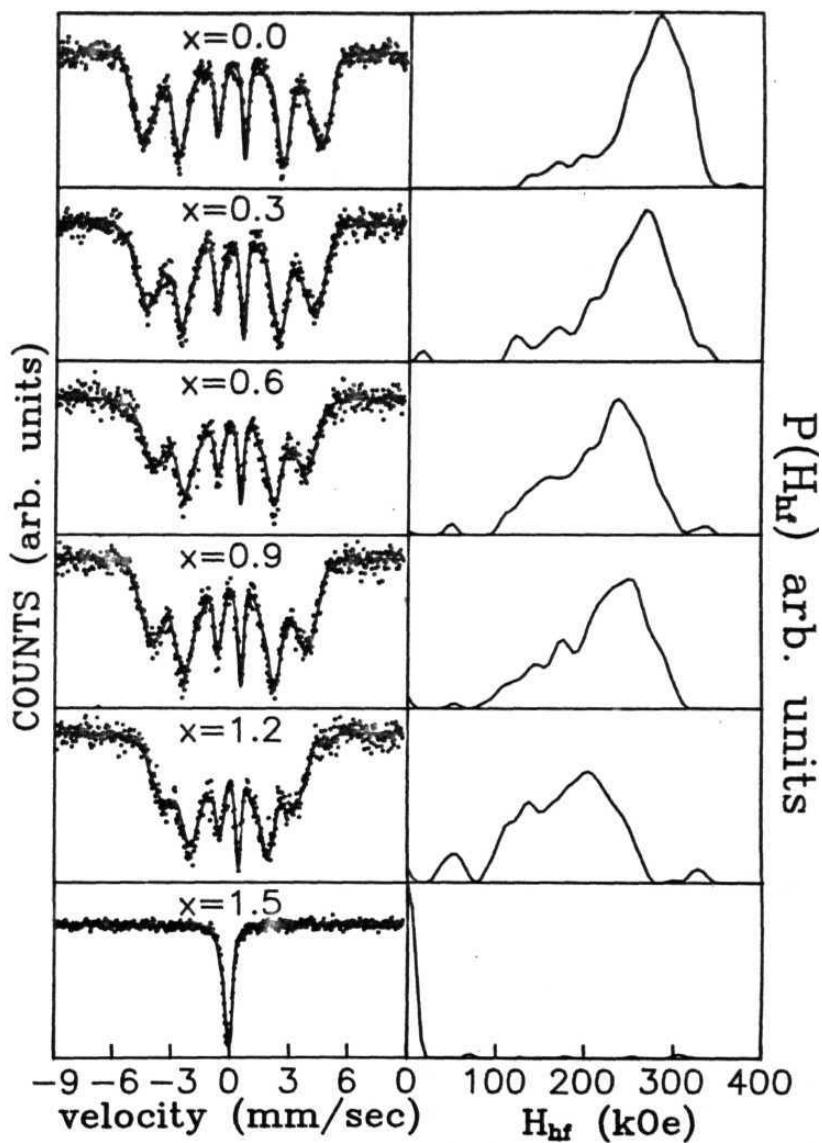


Fig.5.2. Room temperature **Mössbauer** spectra for disordered **$\text{Fe}_{3-x}\text{Mn}_x\text{Al}$** alloys and hyperfine field distributions **cal-**
culated using model-independent Le **Cäer** program.

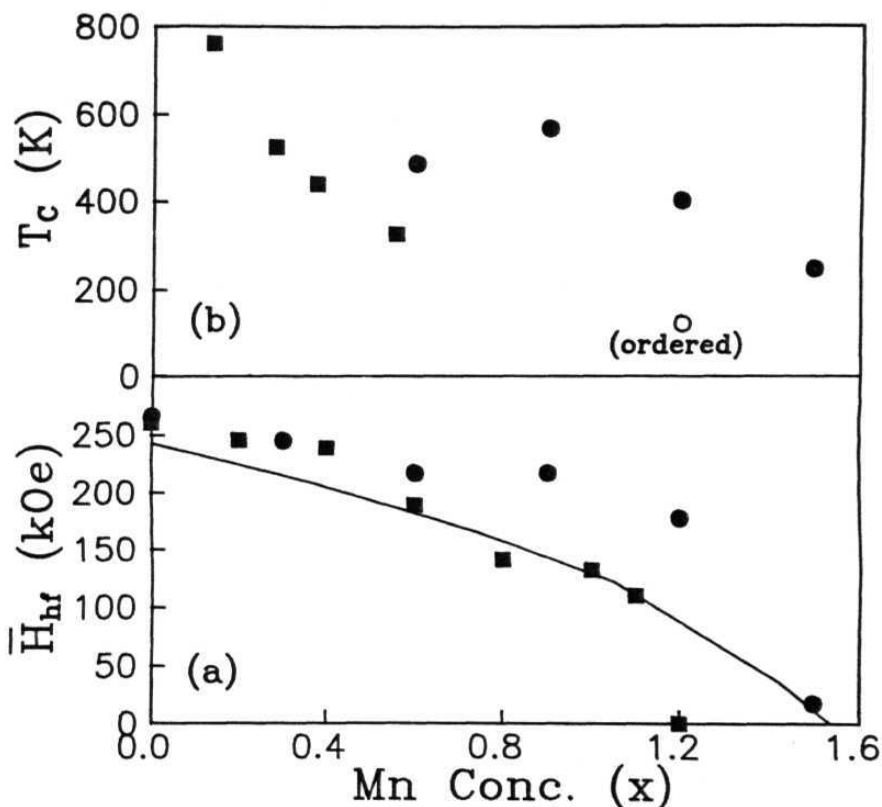


Fig.5.3 a. Variation of average hyperfine field, \bar{H}_{hf} , with Mn concentration (x) for disordered $\text{Fe}_{3-x}\text{MnAl}$ alloys (\bullet : our data and \blacksquare : of Alcazar et.al data (Ref.9)). The solid line represents the theoretical behaviour of \bar{H}_{hf} using site diluted Ising Model.

b. Variation of Curie temperature, T_C , with Mn concentration x for disordered $\text{Fe}_{3-x}\text{MnAl}$ alloys (\bullet : our data) and ordered alloys (\bullet : data of Mager et. al (Ref.8)). The open circle represents the T_C for x = 1.2 composition in the fully ordered state (our work).

pendence of H_{hf} on x is quite different. It may therefore be necessary to take into account the actual nature of Fe-Mn exchange interactions to understand the data instead of assuming Mn to be a simple non-magnetic dilutant like Al.

5.3.b. Hyperfine Fields in Ordered Alloys

To find the nature of Fe-Mn exchange interactions we look at the Mössbauer spectra and hyperfine field distributions of ordered alloys (Fig. 5.4) which were subjected to a heat treatment of 24 hours at 400° C. In the ordered state the hyperfine field distributions for alloys with Mn concentration upto $x = 0.9$ show separation in two regions. The high field region with hyperfine field of about 315 kOe and a broad distribution in low f^*_{ld} region. The higher field corresponds to a configuration with 8 near neighbour (nn) Fe atoms and comes from the Fe atoms at B sites. These sites have 8 AC Fe near neighbours and the association of the high field to this site is; reasonably well established from studies on ordered Fe_3Al alloys [1]. The distribution at lower fields is attributed to Fe atoms located at the AC sites. These sites are twice in number as the B sites and their environment depends on the type of chemical order. For perfect DO_3 order, these sites have only 4 Fe first neighbours and should give a single field of 210 kOe for this configuration. If Mn substitutes for Fe at B site in the DO_3 structure it would give Fe(A,C) sites with 4 or less Fe neighbours since the four D sites are occupied by Si atoms in DO_3 structure (Fig 4.7b). However for the B2 ordered configuration, the 4 D sites which are nn

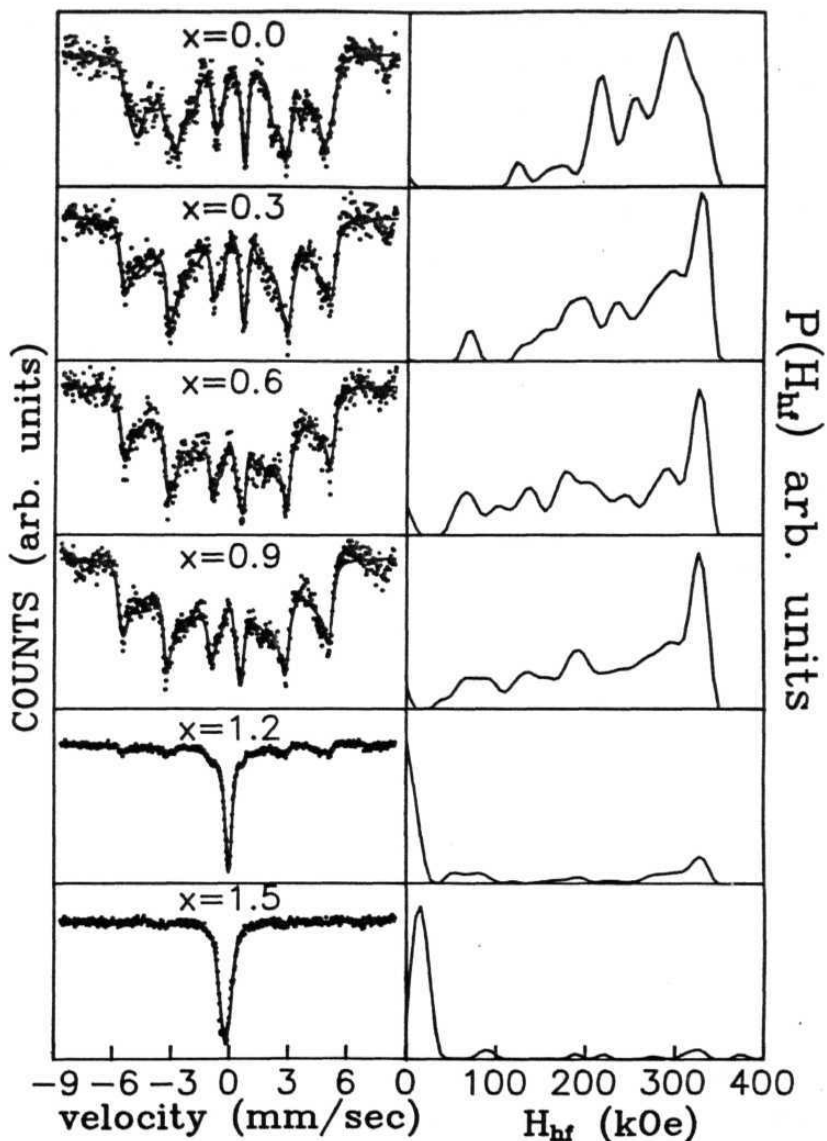


Fig.5.4. Room temperature Mössbauer spectra for ordered $\text{Fe}_{0.5}\text{MnAl}$ alloys and hyperfine field distributions calculated using model-independent Le Cœur program.

to AC sites have a random **occupancy** by Fe as well as **Al** and Mn atoms. This gives a broad distribution in the low field regions centered around 4 Fe nn **configuration** which arises due to a distribution in the number of nn Fe atoms of the AC site. The **observed** wide distribution in the low field region thus arises due to the nn **configurations** of the AC sites and very strongly indicates presence of B2 ordered state in this alloy.

The hyperfine fields corresponding to all Fe **configurations** are easily identifiable in the field **distribution** for $x = 0.6$ composition. These are plotted in Fig. 5.5. This association of the fields to different number of Fe **near** neighbours is well established from studies in **Fe-Al**, Fe-Si and Fe-Ge alloys. The linear increase of hyperfine field with **number** of Fe near neighbours shows that the magnetic properties in this system also are mainly governed by local environment **effects**. It then becomes easy to study the evolution of short range order in the system with a good reliability which will be discussed in the following discussion.

5.3. c. Chemical Ordering and Reentrant Behaviour in $\text{Fe}_{1.8}\text{Mn}_{1.2}\text{Al}$

The ferromagnetic to **paramagnetic** transition temperature (T_c) in the ordered alloys are observed to be lower than the disordered alloys (Fig. 5.3b). The **presence** of Mn at B and D sites in the ordered alloy leads to an **increase** of Fe-Mn pairs in the ordered state relative to the disordered states. The significant decrease in T_c in going **from** disorder to order **therefore** means

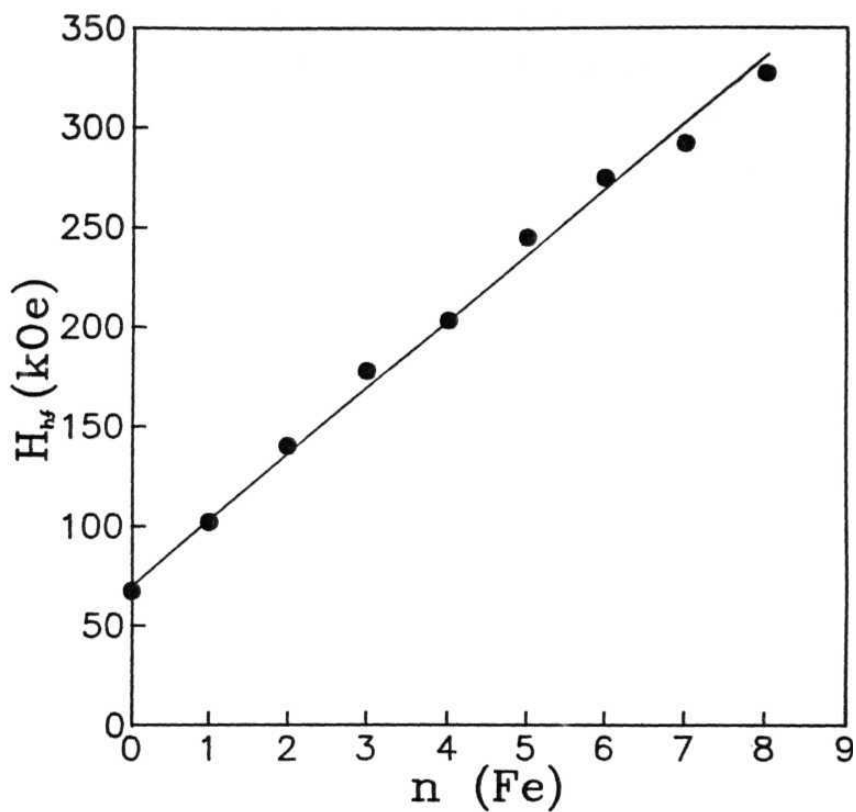


Fig.5.5. Dependence of hyperfine field on number of Fe atoms as near neighbours of an Fe atom in ordered $\text{Fe}_{2.4}\text{Mn}_{0.6}\text{Al}$.

that the **Fe-Mn** exchange is much weaker than the Fe-Fe exchange. Temperature dependent magnetisation measurements were also carried out on the **ordered Fe- $\text{Fe}_{0.8}\text{Mn}_{0.2}\text{Al}$ alloy** which shows a large decrease in T_C in going from the chemically disordered to ordered phase. Fig. 5.6 shows data for magnetisation in zero field and field cooled sample. There is re-entrant behaviour in this system also as was seen for the **Fe-Mn-Si** alloys. The zero field cooled magnetisation is different from field cooled magnetisation below 40 K. This is an evidence for spin glass behaviour and shows the presence of competing **ferromagnetic** and **antiferromagnetic** exchange interactions. Once again the origin of antiferromagnetic exchange lies in the **Mn-Mn** second neighbour interactions which was discussed earlier for FeMnSi alloys and the magnetic behaviour of this system is quite similar to the Si based alloy system [14].

5.3. d. Kinetics of Ordering in **Fe- $\text{Fe}_{0.8}\text{Mn}_{0.2}\text{Al}$**

The kinetics of approach to ordered state from disordered state is studied through a change in the hyperfine field distributions of the $x = 1.2$ alloy as a function of annealing time at 300° C. Fig. 5.7 shows the **Mössbauer** spectra and the corresponding hyperfine field distributions which have been obtained by fitting the data to two Gaussian field distributions [15]. The field distribution centred at the higher hyperfine field value arises from distribution of nn environment of the Fe atoms at B sites whereas the Gaussian distribution at lower field value comes from environment of AC site Fe atoms. With time the intensity of the low field Gaussian is seen to increase whereas the

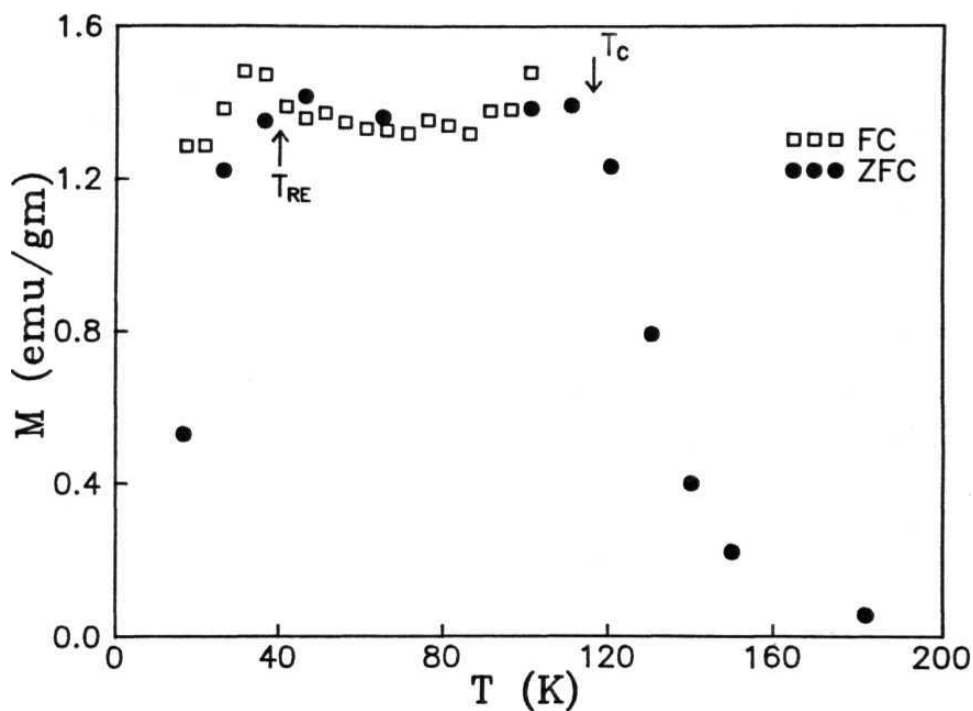


Fig.5.6. Temperature dependence of magnetisation for ordered $\text{Fe}_{18}\text{Mn}_{12}\text{Al}$ alloy (\square : Field cooling and \bullet : Zero field cooling). The Curie temperature (T_C) and Reentrant temperature (T_{RE}) are indicated.

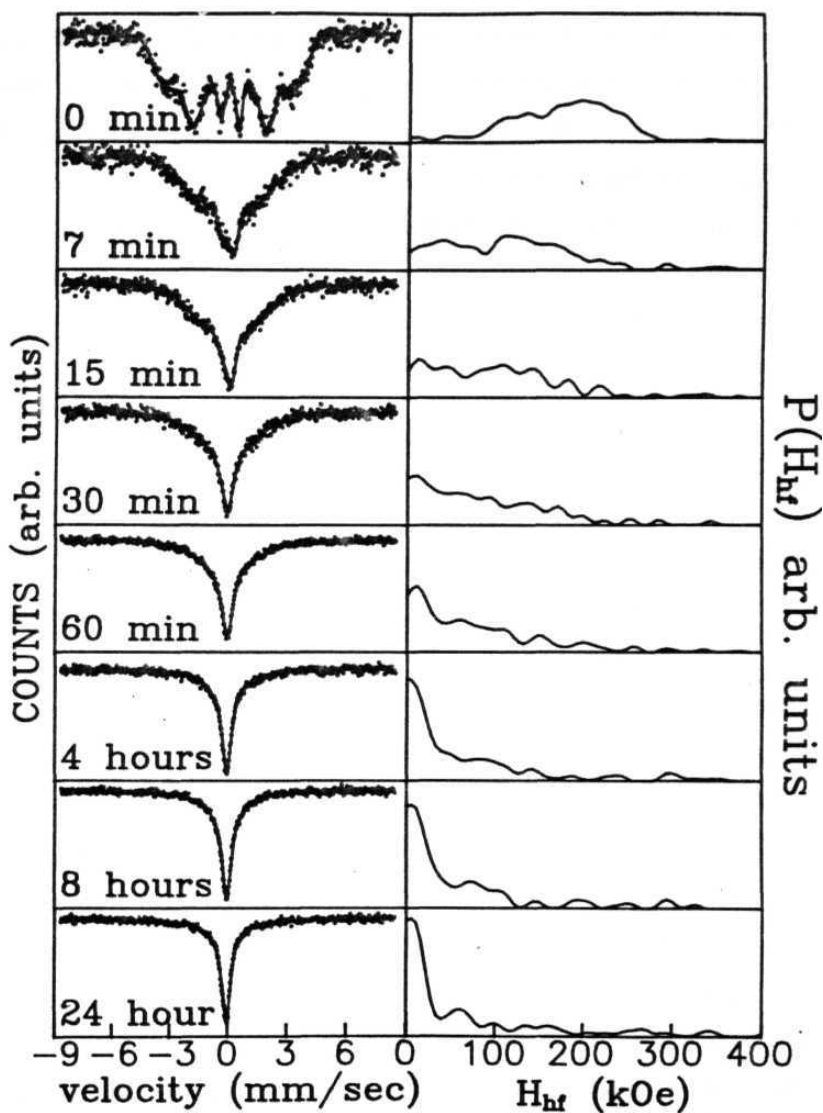


Fig.5.7. Room temperature Mössbauer spectra for $\text{Fe}_{18}\text{Mn}_{12}\text{Al}$ annealed at different times, and corresponding hyperfine field distributions obtained by fitting data to two Gaussian field distributions.

higher field Gaussian intensity decreases rapidly to low values. The increase in low field intensity reflects the growth of ordered B2 **configuration** around the AC sites which consists of all **Al** or Mn atoms as first neighbours and hence a low hyperfine field. The decrease in high field intensity reflects the movement of the wrongly placed B site Fe atoms since in the B2 ordered configuration these sites are to be filled with Mn atoms. We have to keep in mind here that the measured hyperfine field in a **Mössbauer** study is for Fe atoms only.

Fig. 5.8 shows the time dependence of these intensities. The higher field intensity (I_0) shows a more rapid decrease with time than the increase of the lower field intensity (I_1). Such different kinetics of relaxation of order parameters are expected in ternary alloys as shown by **Fultz [16]** who calculated the kinetics of disorder-B2 transformation in pair **approximation** and showed that the evolution of order is affected by **differences** in interatomic potentials, differences in activation barrier height and vacancy ordering. This was done by a numerical integration of rate equations written for different pair variables. However we can employ an intuitive but analytical approach to study the kinetics of evolution of order in the system. This is based on looking at how the change in **thermodynamic** free energy can control the kinetics of ordering. As proposed by **Khachaturyan [17]** and **Fultz [18]**, it is expected that the rate of change of an order parameter η should depend on the sensitivity of the free **energy** G to this order parameter

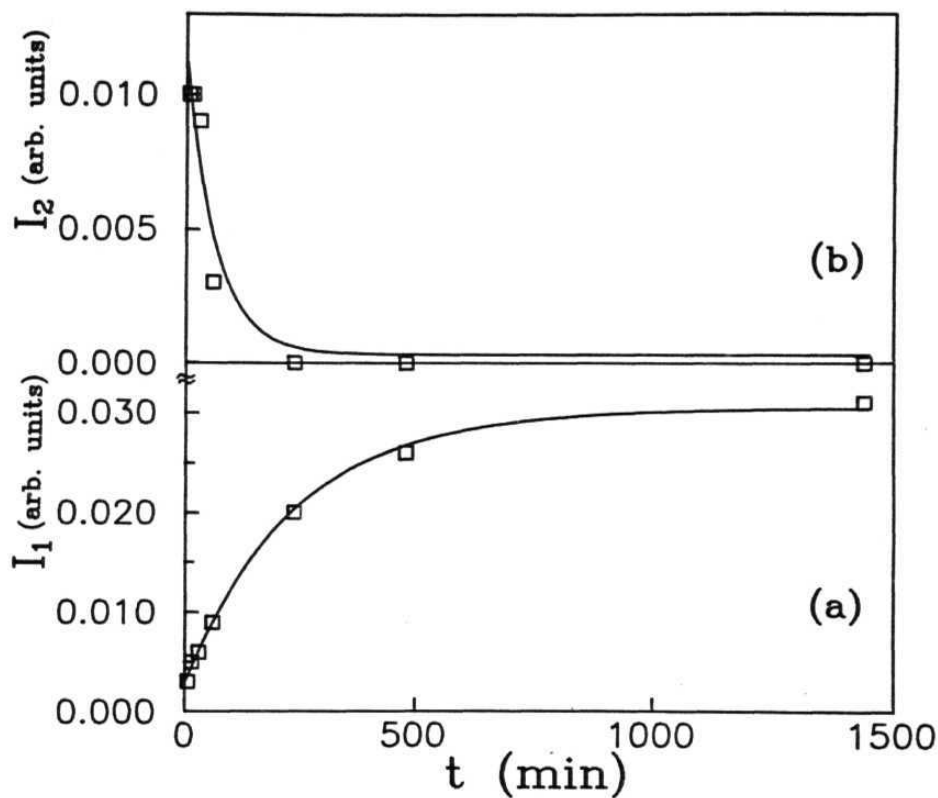


Fig. 5.8. Time dependence of the intensity of low field Gaussian (a) and high field Gaussian (b). The solid lines represent the fit to the data according to equation (5.5) as discussed in the text.

$$d\eta/dt = -(L/kT)(dG/d\eta) \quad (5.1)$$

Where L is the mobility which depends on the mechanism of the ordering, t is the time, k is Boltzman constant and T is temperature. Expanding the free energy in a Taylor series around $\eta = \eta_{eq}$ gives

$$G(\eta) = G(\eta_{eq}) + \frac{1}{2} \left(\frac{d^2G}{d\eta^2} \right)_{\eta=\eta_{eq}} (\eta - \eta_{eq})^2 + \frac{1}{6} \left(\frac{d^3G}{d\eta^3} \right)_{\eta=\eta_{eq}} (\eta - \eta_{eq})^3 + \dots \quad (5.2)$$

where we have set $\left. \frac{dG}{d\eta} \right|_{\eta=\eta_{eq}} = 0$ for stable equilibrium. If a system is relaxing from a state near thermodynamic equilibrium the third order and higher terms in the above expansion can be neglected and one gets

$$d\eta/dt = -A(\eta - \eta_{eq}) \quad (5.3)$$

$A = (L/kT)(d^2G/d\eta^2)_{\eta=\eta_{eq}}$, and this gives a simple exponential relaxation behaviour for the order parameter

$$\eta(t) - \eta_{eq} = (\eta_0 - \eta_{eq}) \exp(-At) \quad (5.4)$$

where η is the order parameter at $t = 0$. We fitted the time dependence of I_1 and I_2 to the simple exponential relaxation behaviour given by Eq. (5.4) and obtained a reasonable fit for I_2 (intensity of the high field Gaussian) but not so for I_1 (intensity of low field Gaussian). If the third order term is also

included in the expansion of $G(\eta)$ in Eq. (5.4) we get after integration of the differential equation

$$\eta - \eta_{eq} = \frac{A(\eta_o - \eta_{eq})[1+B(\eta_o - \eta_{eq})]e^{-At}}{[A+B(\eta_o - \eta_{eq})][1+B(\eta_o - \eta_{eq})(1-e^{-At})]} \quad (5.5)$$

with $B = (L/2kT)(d^3G/d\eta^3)_{eq}$.

Eq. (5.5) gives a good fit to experimental data of I_1 with $A = 4.18 \times 10^{-3}$ and $B = 1.886 \times 10^{-3}$. Fig. 5.8 shows the fit to the data. For I_2 the value of B comes out to be very small (1.48×10^{-5}) and inclusion of the third order term **makes** no significant improvement in the fit.

With $B = 0$, there is a simple exponential relaxation behaviour and $1/A$ gives the relaxation time for the disorder-order **transformation**. Presence of this B term indicates a more complicated dependence of relaxation rate on the instantaneous value of η . Our results show a very significant difference in the kinetic behaviour of the two order parameters. As explained earlier, change in I_1 is a measure of the **kinetics** of movement of wrongly placed Fe atoms from B sites and in the approximation of small B thus has a small relaxation time of **65** minutes (as estimated from inverse of A). The process of ordering around the AC sites as measured by changes in I_2 is more complicated and an approximate relaxation time can be given for this process as 240 minutes.

A physical explanation for the difference in kinetics of the two processes can be given as follows: The rapid movement of

wrongly placed Fe atoms at B sites can proceed by **vacancy-atom** interchange which has a low activation energy. The other slower process of ordering around AC sites then proceeds by movement of Mn and **Al** atoms to the B and D sites and development of equilibrium B2 order takes place.

5.4. CONCLUSIONS

The substitution of Fe by Mn in the binary **Fe₃Al** system gives rise to magnetic properties of the ternary system which depend very strongly on the state of chemical order and our hyperfine field distribution indicates B2 order in the ternary system. Two different rates of temporal evolution of order parameters are observed in the ternary alloy system which can be attributed to two distinct kinetic mechanisms which may be operative in the ordering process.

REFERENCES

- [1] **Z.Q.** Gao and B. **Fultz**, Phil. Mag. 67, 787 (1993).
- [2] L. Anthony and B. Fultz, J. Mater. Res. 4, 1140 (1989).
- [3] B. Fultz, Z.Q. Gao and H. **Handeh**, Hyperfine Interact. 54, 799 (1990).
- [4] M. Tuszynski, **W.** Zarek and E.S. Popiel, Hyperfine Interact. 59, **369** (1990).
- [5] W. Zarek, M. Tuszynski and E.S. Popiel, J. Magn. Magn. Mater. 104-107, **2067** (1992).
- [6] D. Satula, K. **Szymanski**, L. Dobrzynski, J. Waliszewski and A. Malnowski, J. Magn. **Magn.** Mater. 140-144, 61 (1995).
- [7] E. Wieser and S. Mager, Phys. Stat. Sol.(a)40, 497 (1977).
- [8] S. Mager, E. Wieser, T. **Zenick**, O. Schneeweiss, P.N. Stetsenko and V.V. Surikov, Phys. Stat. Sol.(a)52,249 (1979).
- [9] G.A. Perez Alcazar, J.A. Plascak and E. Galvao da **Silva**, Phys. Rev. B38, 2816 (1988).
- [10] D.J. Chakrabarti, Metall. **Trans.B8**, 121 (1977).
- [11] J. Gordon Parr, Acta Cryst. 5, 842 (1952).
- [12] G. Le **Cäer** and J.M. Dubois, J. Phys.E12, 1083 (1979).
- [13] G.A. Perez Alcazar, J.A. Plascak and E. Galvao da Silva, Phys. **Rev.B34**, 1940 (1986).
- [14] T.V.S.M. Mohan Babu, **C.Bansal** and **S.N. Kaul**, J. Magn. Magn. Mater. 140-144, 127 (1995).
- [15] T.V.S.M. Mohan Babu and C. **Bansal**, Phys. Stat. **Sol.(b)180**, 479 (1993).
- [16] B. Fultz, J. Mater. **Res.7**, 946 (1992).

- [17] A.G. **Khachatryan** in "**Progress in Materials Science**" edited by B. Chalmers, **J.W. Christian** and T. **Massalski** (Pergamon press, Oxford, 1975) **Vol 22, p.1.**
- [18] B.Fultz, Nonintuitive features of disorder-order transformation, (preprint, 1994).

CHAPTER 6

**EFFECT OF *Si* SUBSTITUTION ON THE ORDERING OF
Ni₃Fe AND SITE SUBSTITUTION EFFECTS IN $\text{Ni}_3\text{Fe}_{1-x}\text{Si}_x$
ALLOYS**

6.1. INTRODUCTION

There have been several studies undertaken to understand the effect of ternary additions on the hyperfine field **systematics** [1-3] and **L1₂** ordering behaviour of the **Ni₃Fe** alloy [4,5]. In the **L1₂** ordered **Ni₃Fe** structure Fe atoms occupy the cube corner sites and have 12 Ni first neighbours (at the face centre sites) and 6 Fe second neighbours (at cube corners). Addition of Cr to **Ni₃Fe** was found to reduce the number of Fe atoms on Ni sites thereby increasing the degree of **L1₂** order, and the presence of Cr on a Ni first neighbour site decreased the Fe field by 45 kOe [1]. Studies with Sn, **Al**, and Mn substitutions showed that these substituents primarily occupy the Fe site and increase the **L1₂** ordering temperature. This tendency was empirically understood in terms of the heat of solution of metal B in metal A, when A and B form an **A₂B** alloy since both dissolution of metal B in A and **L1₂** ordering lead to breaking of B - B bonds and their replacement by A - B bonds [2].

The heat of solution of Si in Ni is large (1530 **meV**) and the ordering temperature of **Ni₃Si** is also large (1423 **K**) [6]. In this work we therefore study the effect of Si addition to **Ni₃Fe** which has not been experimentally studied as yet. We look at the site substitution behaviour of Si, hyperfine field perturbation at Fe due to presence of Si and the near neighbour effects due to **L1₂** ordering, through a **Mössbauer** effect and X-ray diffraction study of the **Ni₃Fe_{1-x}Si_x** quasi-binary system.

6.2. EXPERIMENTAL

$\text{Ni}_3\text{Fe}_{1-x}\text{Si}_x$ alloys in the composition range $x = 0.0, 0.1, 0.25, 0.5, 0.75$ and 0.9 were prepared by arc melting. Requisite quantities of 4N purity iron, nickel, and silicon powders were mixed thoroughly and pressed into pellets. They were melted under argon atmosphere in an arc furnace with a water cooled copper hearth. Melting was done repeatedly to ensure homogeneity. The typical weight loss in the melting process was 2 %. The alloy ingots were homogenised at 800°C for 48 hours after sealing them in quartz tubes under a pressure of about 10 torr. A part of homogenised alloy ingot was filed to coarse powder and subsequently ground to finer powder in mortar and pestle. The powders were annealed at 475°C for 7 days in vacuum sealed quartz tubes

-4

(≈ 10 torr). Mössbauer absorbers (having natural Fe content of 25 ng/cm) were prepared from alloy powders after mixing with boron nitride. The homogenised ingots of $X = 0$ and 0.25 were splat quenched in an Edmund Bühler ultra quenching apparatus to prepare the disordered alloys.

Samples were characterised by powder X-ray diffraction on a Siefert Isodebyeflex Model 2002 X-ray diffractometer using CuK_α radiation. Room temperature ^{57}Fe Mössbauer spectra were recorded on μP based spectrometer [7]. A ^{57}Co in Rh matrix source was used. The spectra were analysed using a Fast Fourier Transform (FFT) program. The Mössbauer spectrum for $x = 0.75$ showed two resolved six line patterns. The six line pattern due to the lower field was about double the intensity of the pattern due to the

higher field. The FFT program could not fit this complex spectrum. Thus this complex spectrum was fitted using a stripping procedure [8].

6. 3. RESULTS AND DISCUSSION

6.3.a. X-ray Diffraction

The powder X-ray diffraction patterns for all the compositions ($0 \leq x \leq 0.9$) could be indexed to a **fcc** unit cell and the lattice parameter a was calculated using Bradley and Jay plots [9]. The value of a was calculated for each line in the X-ray pattern with indexed **hkl** values and were plotted against $\cos^2\theta$. By the extrapolation of a vs. $\cos \theta$ plot to $\theta = 90^\circ$, the intercept on the ordinate gave the exact value of a . The variation of a with Si concentration X is shown in Fig. 6.1. The value of a for **Ni₃Fe** comes out to 3.54 Å and it is in good agreement with the reported value. The reported value of a for **Ni₃Si** is indicated by a solid circle. For $x = 0.75$ composition, there is indication of an extra phase but the diffraction peaks were not well resolved for this extra phase. However presence of this extra phase was clearly observed in the **Mössbauer** spectrum because **Mössbauer** technique is very much sensitive to the presence of small amount of any phase. The hyperfine field value for this extra phase was calculated from the **Mössbauer** spectrum using stripping procedure. This hyperfine field value coincides with the value for **α -Fe**. It indicates that there is a precipitation of **α -Fe** at this composition. For $x = 0.9$ we got a single phase alloy

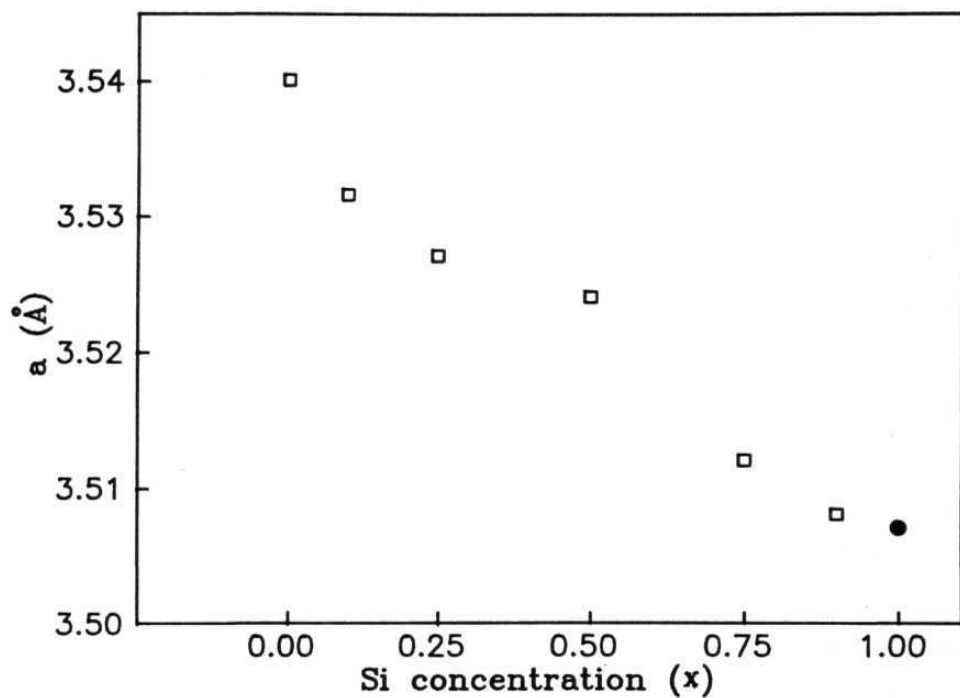


Fig.6.1. Variation of lattice parameter (a) for **fcc** unit cell with Si concentration (x) in **Ni₃Fe_{1-x}Si_x** system. Solid circle represents the value for **Ni₃Si** taken from ref. 12.

and the value of a is close to Ni_3Si value. These observations shows that Ni_3Fe and Ni_3Si were not miscible throughout the composition range and there exist a miscibility gap around $x = 0.75$ composition. Based on the above arguments the ternary phase diagram for this alloy system is drawn. Fig. 6.2 shows the ternary phase diagram and miscibility gap around $x = 0.75$ composition. The numbers 1, 2, 3, 4, 5 and 6 represent $x = 0, 0.1, 0.25, 0.5, 0.75$ and 0.9 respectively. The region C indicates the miscibility gap and solid circle is for $x = 0.75$. These results are qualitatively similar to those of $\text{Ni}_3\text{Fe}, \text{Al}$ alloy system which shows a miscibility gap near $x = 0.5$ composition [10].

6.3.b. Hyperfine Fields, Linewidths and Magnetic Dilution Effects

Fig. 6.3 shows the Mössbauer spectra for the splat quenched alloys of compositions $x = 0$ and 0.25 . The average hyperfine field for the Ni_3Fe alloy ($x = 0$) is 292.7 kOe and the linewidth of the outermost lines is 0.63 mm/sec . The average field and linewidths of outer lines obtained by Drijver et. al [4] for cold rolled foils was 295.7 kOe and 0.75 mm/sec respectively. The effect of increasing order by annealing at 760 K is a decrease in average field (approaching a value of 272 kOe , which is the field observed at Fe in Ni metal) and also a decrease in linewidth. The decrease in field as well as linewidth is correlated to the L1_2 long-range order in the system. Although the average field for the partially ordered samples are seen to fit this dependence very well, the data on cold rolled foils of Drijver et. al are not consistent with this dependence. This is attribu-

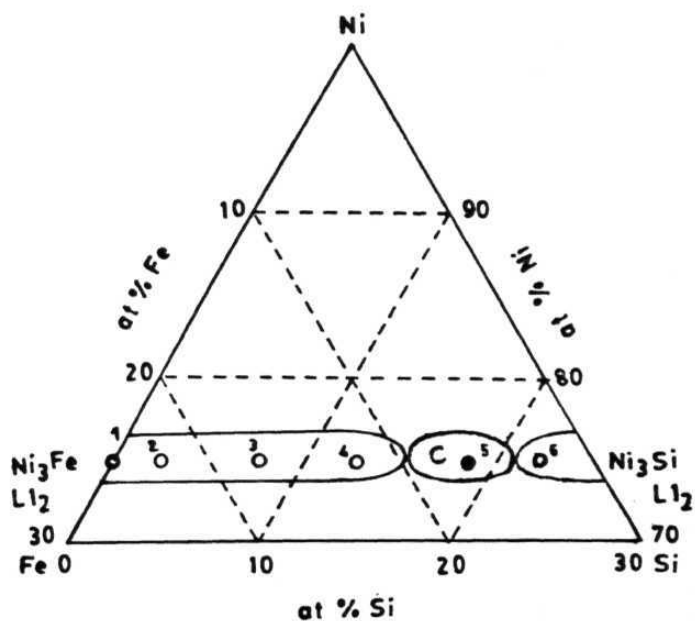


Fig.6.2. Quasi-binary section of the phase diagram for $\text{Ni}_3\text{Fe}_{1-x}\text{Si}_x$ alloy system. C indicates the approximate region of the miscibility gap.

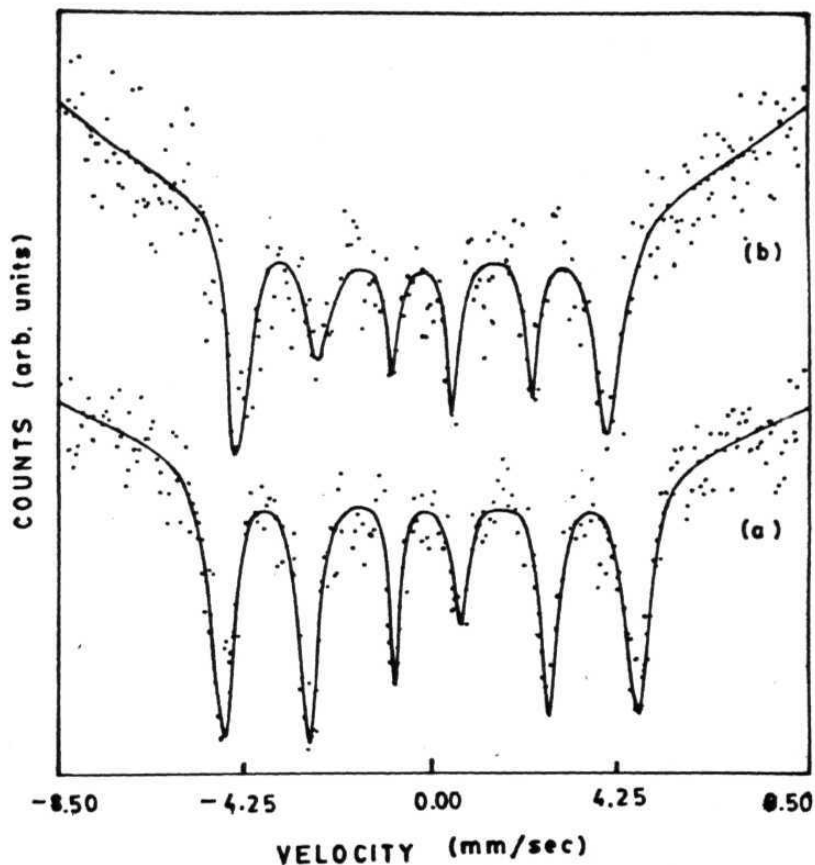


Fig.6.3. Mössbauer spectra for splat quenched alloys: Ni_3Fe (a), and $\text{Ni}_3\text{Fe}_{0.75}\text{Si}_{0.25}$ (b). The solid lines are fits to data using Fast Fourier Transform Program.

ted to the possible change in microstructure of the foils due to cold rolling. The **parameters** obtained from our rapid anvil and piston quenching should be better representative of the state of high chemical disorder in the samples. Similarly the field obtained for our ordered foils is 281 kOe which is slightly higher than the value of 278 kOe obtained by **Drijver et. al** for their ordered samples. The linewidths obtained is slightly lower (0.44 **mm/sec** for our alloys as compared to 0.45 to 0.46 **mm/sec** for **Drijver et. al**) suggesting that the final degree of order achieved is also slightly better in our alloy. The average hyperfine field for the splat quenched **Ni₃Fe_{0.75}Si_{0.25}** alloy is observed to be **260.8** kOe and the linewidth of outer lines is **0.63 mm/sec**. There is thus a large decrease (≈ 32 kOe) in hyperfine field at Fe site due to the presence of Si first near neighbours which arise in the disordered sample due to random occupying of all sites by Fe, Si and **Ni**. This field shift to be compared with dilution effects observed by Stearns [11] in **bcc** Fe-Si alloys. A decrease of 8 percent field at Fe was observed due to presence of Si first neighbours at a distance of $0.87 a_{Fe}$ in the **bcc** system. For Si in **fcc Ni₃Fe**, the first neighbour Fe - Si distance is also about $0.87 a_{Fe}$ but the field decrease observed is 11 percent as compared to the field in disordered **Ni₃Fe**.

6.3.c. Chemical Ordering Effects

The effect of chemical ordering (anneal at **475^o** C for 7 days) on the **Ni₃Fe_{0.75}Si_{0.25}** alloy is to increase the average hyperfine field to 271.3 kOe, a value which is close to the value

of Fe **hyperfine** field in nickel (272 kOe). This shows that the chemical order induced in the system is also of **L1₂** type with Si atoms occupying the Fe sites, thereby producing a first neighbour environment of Fe consisting of 12 **Ni** atoms (face centres) and a second neighbour environment consisting of Fe and Si atoms (at cube corners). The magnitude of hyperfine magnetic field is lower than that obtained for ordered **Ni₃Fe** (281 kOe) which is also consistent with the presence of nonmagnetic Si neighbours at Fe sites in the second neighbour shell.

The effect of the ordering heat treatment (anneal at 475° C for 7 days) on all samples is shown in Fig. 6.4 and the average hyperfine field values are shown in Fig. 6.5. **Drijver** et. al deduced linear correlation between Fe hyperfine field and number of first near neighbour (**n₁**) and second near neighbour Fe (**n₂**) atoms as follows:

$$H = H(0,6) + n_1 \Delta H_1 + (n_2 - 6) \Delta H_2 \quad (6.1)$$

where $H(0,6) = 276.6$ kOe is the field **for** 0 first and 6 second neighbour Fe atoms (fully ordered **L1₂** structure), $\Delta H_1 = 11.6$ kOe is the field contribution due to one Fe first neighbour and $\Delta H_2 = 2.7$ kOe is the contribution due to one second Fe neighbour. Based on Eq. (6.1), the hyperfine field at Fe site in fully ordered **Ni₃(Fe_{1-x}Si_x)** samples with Si substituting Fe atoms in

second neighbour sites and acting as 'magnetic **holes**' in the lattice will be, as shown by the dotted line in Fig. 6.5. The experimental value of hyperfine field for our ordered sample for

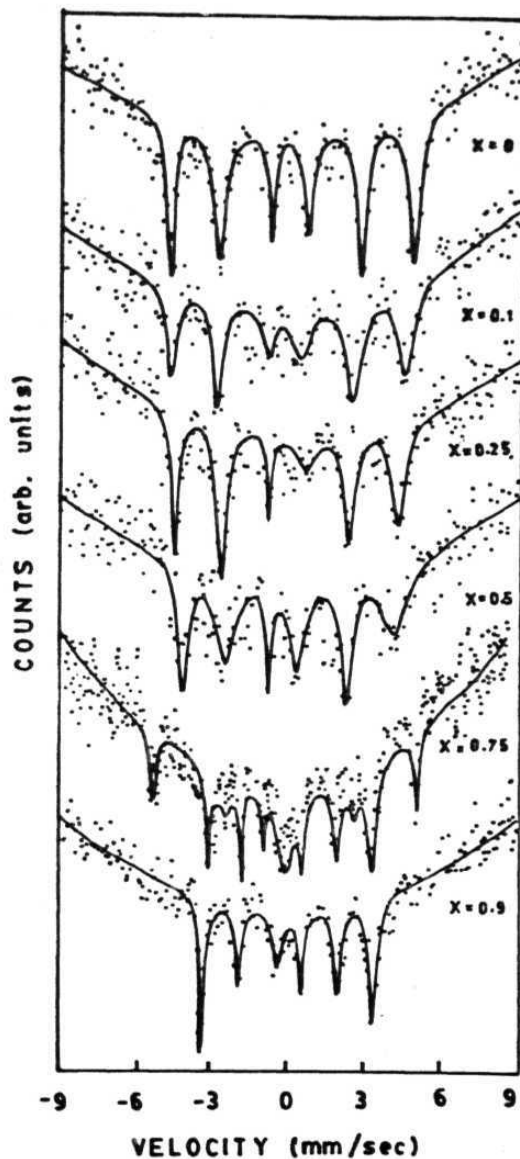


Fig.6.4. Mössbauer spectra for ordered $\text{Ni}_3\text{Fe}_{1-x}\text{Si}_x$ alloys of various compositions subjected to the ordering heat treatment as discussed in text. Solid lines are the fits (for all compositions except $x = 0.75$) to the data using Fast Fourier Transform Program. For $x = 0.75$ composition, a stripping procedure as discussed in Chapter 4 was employed to get the fields corresponding to Fe rich and Ni rich phases.

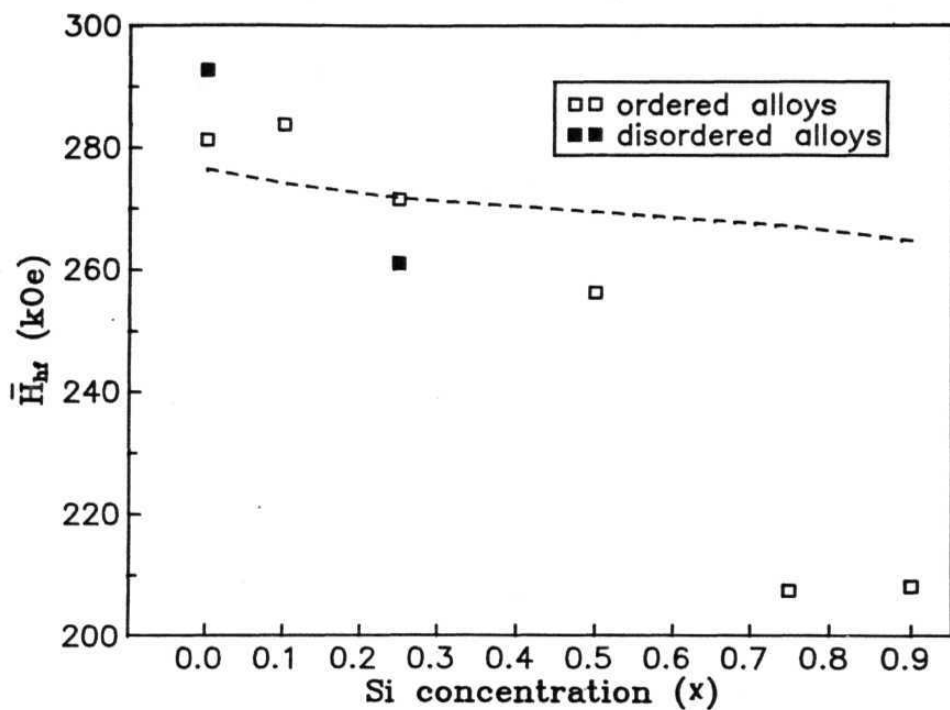


Fig. 6.5. Observed variation of average hyperfine field, \bar{H}_{hf} , in the $\text{Ni}_3\text{Fe}_{1-x}\text{Si}_x$ alloy system. The dashed line is the expected variation for a fully ordered system according to the model of Drijver et. al [4].

$x = 0.25$ is in agreement with the expected value for a well ordered sample. The linewidth of the outermost lines for this sample is observed to be 0.47 m/sec which is close to the value expected for a well ordered sample. At higher Si concentration ($x = 0.5$) the hyperfine field value is much smaller than that expected from a simple dilution approach and this large decrease is due to presence of Si atoms which can be also present in the first neighbour shell if the ordering is not complete. This is also borne out by the very large linewidth (0.93 m/sec) for the sample. Beyond this composition, the $x = 0.75$ alloy shows phase decomposition (Fe rich Ni_3Si and $\alpha\text{-Fe}$) and a predominantly Ni_3Si phase at $X = 0.9$. This corroborates the X-ray diffraction data discussed earlier.

6.4. CONCLUSIONS

Although Ni_3Fe and Ni_3Si both crystallize in an fcc structure there exists a miscibility gap around $x=0.75$ composition in the quasi binary $\text{Ni}_3\text{Fe}_{1-x}\text{Si}_x$ system. The field reduction at Fe site due to presence of Si first neighbours is slightly larger (11 %) in the fcc Ni_2Fe system as compared to the field reduction (8%) due to Si first neighbours in the bcc Fe-Si alloy. Ordering treatment of splat quenched Ni_3Fe and $\text{Ni}_3\text{Fe}_{0.75}\text{Si}_{0.25}$ alloys gives L1_2 order with only Fe and Si second neighbours to Fe sites suggesting that Si atoms show preferential substitution of Fe sites.

REFERENCES

- [1] T.E. Cranshaw, J. Phys. **F: Met. Phys.** 18, 43 (1988).
- [2] T.E. Cranshaw, J. Phys. Condens. Matter 1, **6431** (1989).
- [3] T.E. Cranshaw, J. Phys. Condens. Matter 2, 2743 (1990).
- [4] J.W. Drijver, F. van der Woude and S. Radelaar, Phys. Rev. B16, 985 (1977).
- [5] J.W. Drijver, F. van der Woude and S. Radelaar, Phys. Rev. B16, 993 (1977).
- [6] K. Krolas, Phys. Rev. Lett. **85A**, 107 (1981).
- [7] J.T.T. Kumaran and C. Bansal, Nucl. Instrum. and Methods **B61**, 357 (1991).
- [8] T.V.S.M. Mohan Babu and C. Bansal, Phys. Stat. Sol.(b) **180**, 479 (1993).
- [9] H.P. Klug and L.E. Alexander, X-ray Diffraction Procedures (Wiley, New York, 1974) pp. 591.
- [10] V.G. Rivlin and G.V. Raynor, Int. Met. Rev. 3, 79 (1980).
- [11] M.B. Stearns, Phys. Rev. **147**, 439 (1966).
- [12] E.A. Brandes (Ed.), "Smithells Metall Reference Book", 6ed., (Butterworth, London 1983) p. 6.

CHAPTER 7

QUADRUPOLE SPLITTING IN $FeSi$ AND EFFECT OF AS SUBSTITUTION IN $(Fe_{1-x}Ni_x)_{0.5}Si_{0.5}$ ALLOYS

7.1. INTRODUCTION

FeSi and other transition **metal** silicides (CrSi, **MnSi**, CoSi and **NiSi**) possess the B20 cubic structure [1]. The structure of FeSi is shown in Fig. 7.1. The space group is $T^4 - P2_13$. There are four iron atoms and four silicon **atoms** in a unit cell in positions $(x, x, x; \mathbf{x+1/2, 1/2-x, x; \bar{2}})$ with lattice parameter $a = 4.489 \text{ \AA}$, $x_{\text{Fe}} = 0.137 \pm 0.0020$ and $x_{\text{Si}} = 0.842 \pm 0.004$. Each iron atom is surrounded by seven silicon atoms, and each silicon atom by seven iron atoms. Out of seven silicon atoms around iron atom, one lies along $\langle 111 \rangle$ direction at a distance of 2.29 \AA , three silicon second neighbours at a distance of **2.36** \AA , and the remaining three silicon third neighbours at a distance of 2.53 \AA . Each of this group of three silicon atoms is located symmetrically about the trigonal axis. In addition to these silicon **neighbours**, each iron **atom** has six iron neighbours at a distance of 2.75 \AA . Although the system has B20 cubic structure, the local coordination around Fe atom is less than cubic and results in nuclear electric quadrupole splitting of iron energy levels [2]. Similarly the seven Fe atoms around Si are located at 2.29 \AA (one atom), 2.34 \AA (3 atoms) and 2.52 \AA (3 atoms).

The physical properties of FeSi are unusual. At low temperatures the electrical resistivity shows activated behaviour with a small gap of 0.1 eV . However for $T \geq 300 \text{ K}$, the resistivity increases with T as in a metal [3]. Although magnetic **susceptibility** shows a maximum at 500 K and suggests **anti-ferromagnetically** ordered state below 500 K , neutron diffraction measurements show

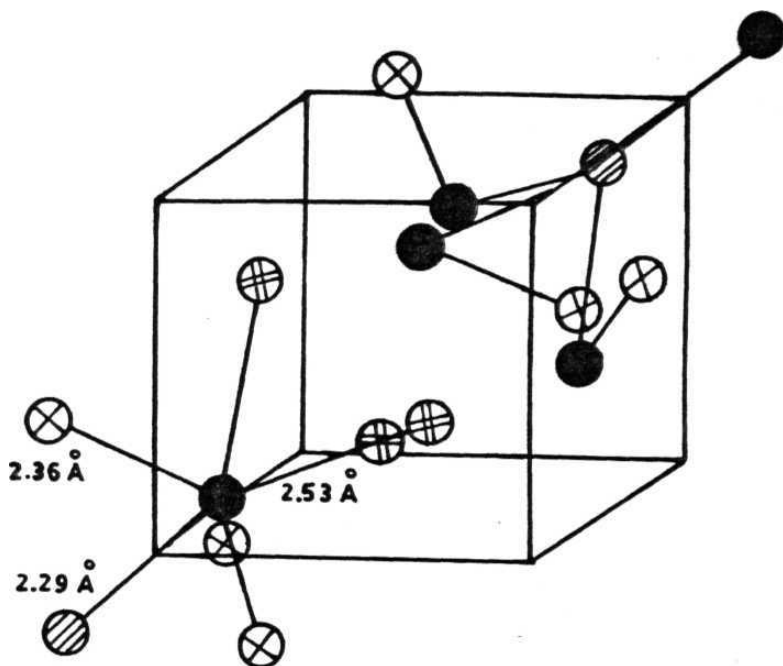


Fig.7.1. B20 cubic structure of FeSi. The Fe atom (solid circle) has one Si first neighbour at 2.29 Å along $\langle 111 \rangle$ direction, three Si second neighbours at 2.36 Å and three Si third neighbours at a distance of 2.53 Å.

no magnetic ordering [4]. It has been proposed that this **narrow** gap characteristic of FeSi is due to a hybridisation gap between conduction band and a localised magnetic moment which is similar to the situation in rare-earth **Kondo** insulators [5]. We have carried out measurement of electric field gradient (EFG) in FeSi and Ni substituted FeSi and found that the calculated field gradient based on ionic lattice contribution can account for the observed value. This indicates a highly ionic nature of this compound which is a property also observed in other hybridisation gap insulators.

7. 2. **EXPERIMENTAL**

A series of samples of composition $(\text{Fe}_{1-x}\text{Ni}_x)_{0.5}\text{Si}_{0.5}$ with $x = 0, 0.05, 0.1, 0.25, 0.5, 0.6$ and 0.75 were prepared by arc melting. The ingots were homogenised at 800°C for 48 hours. The powders **prepared** from the homogenised ingots were annealed at 400°C for 48 hours. **Mössbauer** absorbers were prepared from annealed powders.

7.3. RESULTS AND DISCUSSION

7.3.a. X-ray Diffraction

Representative X-ray diffraction patterns for $x = 0, 0.25$ and 0.6 are shown in **Fig.7.2**. For the samples with composition $x = 0, 0.05, 0.1, 0.25$ and 0.5 , all the lines in the X-ray diffraction pattern could be fitted to a cubic structure. For **sam-**

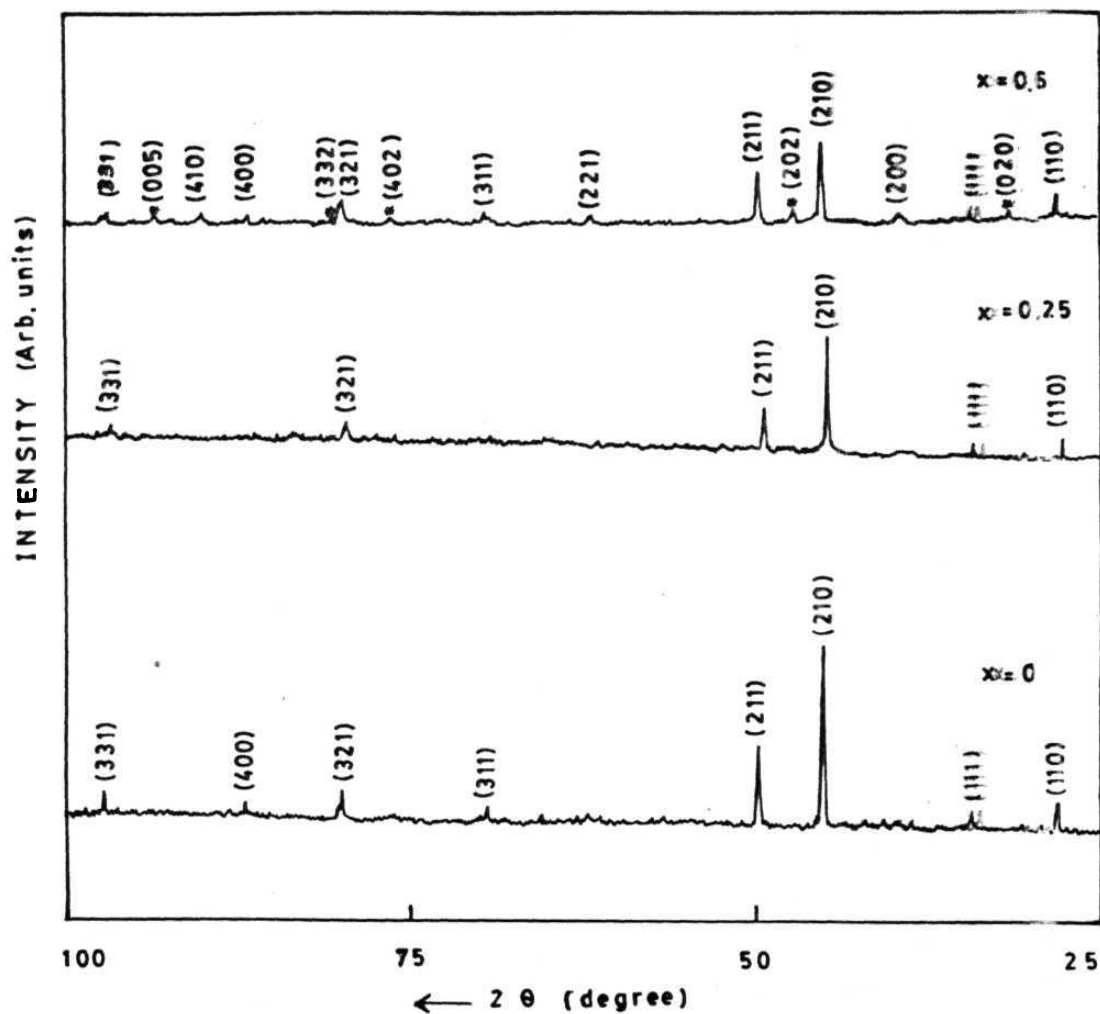


Fig.7.2. Powder X-ray diffraction patterns for $(\text{Fe}_{1-x}\text{Mn}_x)\text{Si}$ alloys with $x = 0, 0.25$ and 0.6 . For $x = 0.6$ composition the lines correspond to orthorhombic phase are indicated by *.

ples with $x = 0.6$ and 0.75 , additional lines were observed which could not be indexed with cubic lattice. The observed additional lines were fitted to a orthorhombic unit cell with lattice parameters close to the values reported for NiSi system ($a = 5.62$ Å, $b = 5.18$ Å, and $c = 3.34$ Å) by Toman [6]. The indexing of the powder patterns for $x = 0$, 0.25 , and 0.6 compositions is shown in Tables 7.1 - 7.3. Fig. 7.4a shows composition variation of lattice parameter for the cubic phase. These observations show that the samples are obtained in a single cubic phase upto $x = 0.5$ composition and a mixture of cubic and orthorhombic phases is obtained beyond $x = 0.5$ composition.

7.3.b. Mössbauer Spectroscopy

The room temperature Mössbauer spectra for all the compositions are shown in Fig. 7.3. The Mossbauer spectra were analysed using a fast Fourier Transform (FFT) program. All the spectra could be fitted to two Lorentzian lines with linewidths in the range of 0.15 to 0.18 mm/sec (HWHM). The quadrupole splitting (Δ) and isomer shift δ (relative to α - Fe) were evaluated from fitted line positions. The isomer shift δ and quadrupole splitting Δ as a function of Ni concentration (x) are shown in Fig. 7.4b and 7.4c. We now calculate the quadrupole splitting assuming that the lattice contribution is dominant. The quadrupole splitting for

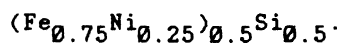
57 Fe arising from electric field gradient of the lattice is given by

$$\Delta E_Q = \frac{1}{2} e^2 q V_{33}^{\text{lat}} \left[1 + \frac{\eta^2}{3} \right]^{1/2} (1 - \gamma_\infty) \quad (7.1)$$

Table 7.1. Indexing of Powder X-ray diffraction pattern for FeSi,

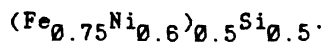
degree	$(I/I_0) \times 100$	hkl	exp A	d_{cal} A
28.00	17	110	3.187	3.185
34.50	9	111	2.600	2.601
44.80	100	210	2.023	2.015
49.50	45	211	1.841	1.840
69.10	8	311	1.359	1.358
79.70	16	321	1.203	1.204
86.80	8	400	1.122	1.126
97.00	12	331	1.029	1.033
103.80	8	421	0.978	0.983
135.30	7	432	0.833	0.836
140.20	8	521	0.819	0.822

Table 7.2. Indexing of Powder X-ray diffraction pattern for



2 θ degree	(I/I ₀) $\times 100$	hkl	d _{exp} Å	d _{cal} Å
28.00	12	110	3.187	3.178
34.50	8	111	2.600	2.595
45.10	100	210	2.010	2.010
49.70	38	211	1.834	1.835
79.90	17	321	1.231	1.201
86.80	7	331	1.030	1.031

Table 7.3. Indexing of Powder X-ray diffraction pattern for



2 θ degree	(I/I ₀)×100	hkl	d _{exp} Å	d _{cal} Å
28.05	29	110	3.181	3.179
31.50	9	0.20	2.840	2.840*
34.50	20	111	2.597	2.598
35.37	6	120	2.538	2.538*
35.90	10	021	2.501	2.501*
40.11	12	200	2.248	2.248
40.42	10	112	2.231	2.205*
45.16	100	210	2.008	2.011
47.15	18	202	1.928	1.930*
49.85	62	211	1.829	1.835
62.20	10	221	1.492	1.499
69.56	13	311	1.351	1.356
76.52	10	402	1.245	1.246*
80.06	29	321	1.199	1.202
80.71	7	332	1.190	1.192*
85.80	10	430	1.133	1.132*
86.93	15	400	1.121	1.124
90.26	10	410	1.088	1.090
93.70	10	005	1.057	1.056*
97.08	12	331	1.029	1.029
122.56	17	510	0.879	0.881

Lines correspond to orthorhombic phase

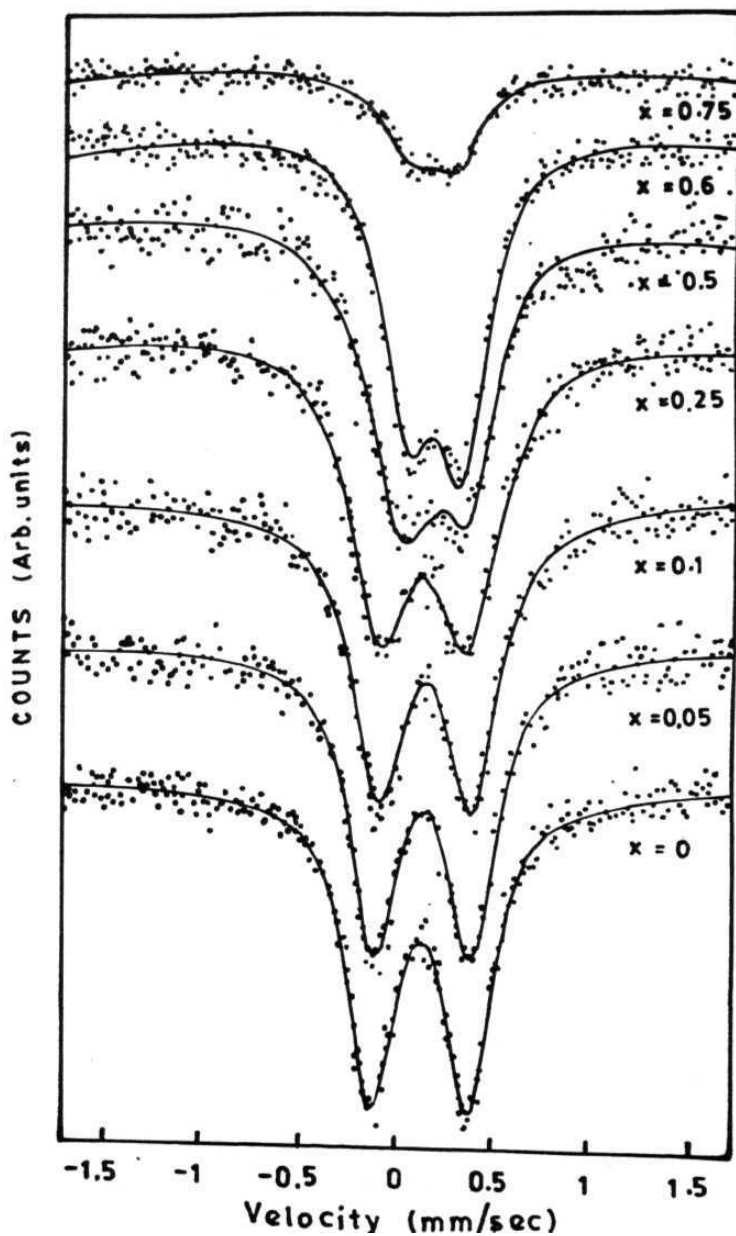


Fig.7.3. Mössbauer spectra of $(\text{Fe}_{1-x}\text{Ni}_x)_{0.5}\text{Si}_{0.5}$ alloys for various nickel concentrations (x). The solid lines are fits to data using two Lorentzians.

where Q is the nuclear **quadrupole** moment, V_{33} is the largest **com-**
 ponent of **EFG** tensor in a set of principal **axes**,
 $\eta = (V_{11} - V_{22})/V_{33}$ is the asymmetry parameter, and r_∞ is
Sternheimer antishielding factor. We consider only the seven
 silicon atoms around Fe which lie upto the third near neighbour
 shell. The EFG contribution from the lattice is calculated using
 the equation

$$V_{ii}^{\text{lat}} = \sum_n q_n \left(3x_{ni}^2 - r_n^2 \right) / r_n^5 \quad (7.2)$$

where q_n is the charge, r_n is the distance from the central Fe
 atom and x . with $i = 1, 2, 3$ is the position of the n th ion. We
 first carry out a principal axis **transformation** by the applica-
 tion of rotation matrix

$$R = \begin{bmatrix} \cos\alpha & -\sin\alpha & 0 \\ \cos\beta\sin\alpha & \cos\beta\cos\alpha & -\sin\beta \\ \sin\beta\sin\alpha & \sin\beta\cos\alpha & \cos\beta \end{bmatrix}$$

with $\alpha = 45^\circ$ and $\beta = 54.40^\circ$. The new coordinates of the silicon
 atoms under this rotation and the components of EFG tensor are
 given in Table 7.4. From these coordinates, we find that the
 asymmetry parameter $\eta = 0$ and the largest component of EFG **ten-**
2
 sor, $V_{33} = 12.033$ q/a . To calculate the numerical value of the
 EFG tensor component V_{33} we need to substitute an appropriate
 value of charge q on the Si near neighbours of Fe.

Table 7.4. Coordinates of Si atoms in the rotated frame **and** their contribution to EFG at Fe.

Si atom	x'/a	y'/a	z'/a	$(a^3/q)v_{11}$	$(a^3/q)v_{22}$	$(a^3/q)v_{33}$
1	0.0000	0.0000	-0.2737	-7.500	-7.500	15.000
2	-0.2234	0.2790	0.6686	-2.974	-1.454	4.427
3	0.3535	0.0538	0.6686	1.104	-5.527	4.422
4	-0.1301	0.3333	0.6686	-4.762	0.349	4.416
5	0.4836	-0.1290	0.0912	11.190	-5.780	-5.415
6	-0.1301	0.4832	0.0912	-5.755	11.169	-5.410
7	-0.3535	-0.3535	0.0912	2.685	2.724	-5.410
				-6.012	-6.019	12.030

7.3.c. Resonating **Valence** Bond Theory and Valence State of Si and Fe

Pauling and Soldate [1] have discussed the nature of the bonds in FeSi and related crystals from their structure and bond lengths. They have calculated the valence state of iron **and** silicon using the resonating valence bond theory.

According to this resonating valence bond theory [7], **silicon** atom with four stable tetrahedral **sp** orbitals in its outer shell which can not form more than four electron-pair bonds can however resonate among more than four positions. For Metallic resonance of valence bonds to occur, some of the **atoms** must possess an extra orbital i.e. metallic orbital. The silicon atom itself possess a metallic orbital (3d orbital), its four bonds undergo resonance about it, if the surrounding atom possess the metallic orbital. The resonance of the four bonds of the silicon atom takes place in such a way that bond numbers are equal to simple fractions $1/2$, $1/3$, $2/3$, ... etc. The observed interatomic distances 2.34 Å (for three bonds) and 2.52 Å (for three bonds) differ by 0.18 Å, it corresponds to a factor $1/2$ in bond number $1/3$. The bond number for 2.52 Å is taken as $1/3$. The bond numbers are always inversely proportional to bond distances. So, the bond number for 2.34 Å is $2/3$. The bond distance 2.29 Å is 0.05 Å smaller than 2.34 Å. Then the bond number for 2.29 Å should be slightly greater than $2/3$ and is taken as 1. Hence the bond numbers for bond distances 2.29 Å, 2.34 Å and 2.52 Å are 1, $2/3$ and $1/3$ respectively. The sum of the bond numbers is $4[1+(2/3) \times 3 + (1/3) \times 3]$ which is equal to the normal valence 4 for

silicon. In calculating the valence state of silicon atom, the six silicon neighbours at 2.78 Å are not taken into account because the bond number is very small and they can not form bonds with silicon atom. Hence the silicon atom can be described as one of its four tetrahedral sp bond orbitals is used in forming a non-resonating single bond with one iron atom at 2.29 Å, the other three orbitals resonate between three iron atoms at 2.34 Å and three iron atoms at 2.52 Å.

Pauling and Soldate deduce the state of iron atom in FeSi to be hexavalent iron. It uses four of its orbitals in forming bonds with seven surrounding silicon atoms – one single bond, three $2/3$ bonds and three $1/3$ bonds. Two orbitals are used in forming six $1/3$ bonds with six neighbouring iron atoms. From all these bonds, the valence state of iron comes to be $6[1 + (2/3) \times 3 + (1/3) \times 3 + (1/3) \times 6]$.

7.3.d. Quadrupole Splitting in FeSi

Taking the charge on Si to be four and the unit cell volume as 90.458 Å^3 , the EFG is calculated with the quadrupole moment for the Fe nucleus $Q = 0.2$ barns. The EFG comes out to be **0.16 m/sec**. The Sternheimer antishielding factor (γ_∞) for 3d ions has been calculated by Sen and Schmidt [8] using uncoupled charge and momentum perturbed Hartee-Fock (UCHF) wave functions. The value of r_{00}^2 for Fe ($3d^2$) configuration comes out to be -2.2. With the calculated EFG and γ_∞ values and using Eq. 7.1, the calculated quadrupole splitting comes out to be **0.512 m/sec**. It is

in very good agreement with our **experimental** value 0.5119 **mm/sec**. This observation confirms the negligible contribution to EFG from valence electrons. This highly localised ionic character of FeSi is a common property which it shares with other rare-earth Rondo insulators such as **CePd₃** and **URu₂Si₂** and is also confirmed by presence of infra-red active phonon modes [11,12].

7.3.e. Effect of Ni Substitution on Quadrupole Splitting and Isomer Shift Behaviour

From Fig. 7.4, it is evident that the substitution of Ni for Fe decreases quadrupole splitting smoothly from 0.52 **mm/sec** for $x = 0$ to 0.25 **mm/sec** for $x = 0.75$. The cubic lattice parameter is constant throughout the concentration range studied. There is a slight increase in isomer shift δ (relative to **α -Fe**) with the increase of Ni concentration. The atomic radius of nickel atom is approximately equal to the atomic radius of iron atom and **hence** there is no change in lattice parameter with the substitution of Ni for Fe. The observed change in quadrupole splitting can arise due to the change in number of (3d + 4s) **electrons** of Fe. With the presence of Ni near Fe, the electronic **configuration** of Fe

$$\begin{array}{cc} 2 & 2-x \end{array}$$

will change from 3d to 3d . This results in a decrease in magnitude of the antishielding factor γ_{∞} and hence a decrease in quadrupole splitting. Akai et. **al** [9] performed systematic **calculations** of charge transfer effects in Fe from substitutional impurities with charges between 0 and 56 in the neighbourhood of Fe. It is found that for the 3d series, charge flows from Fe to the impurity near neighbour site on substitution by an element to

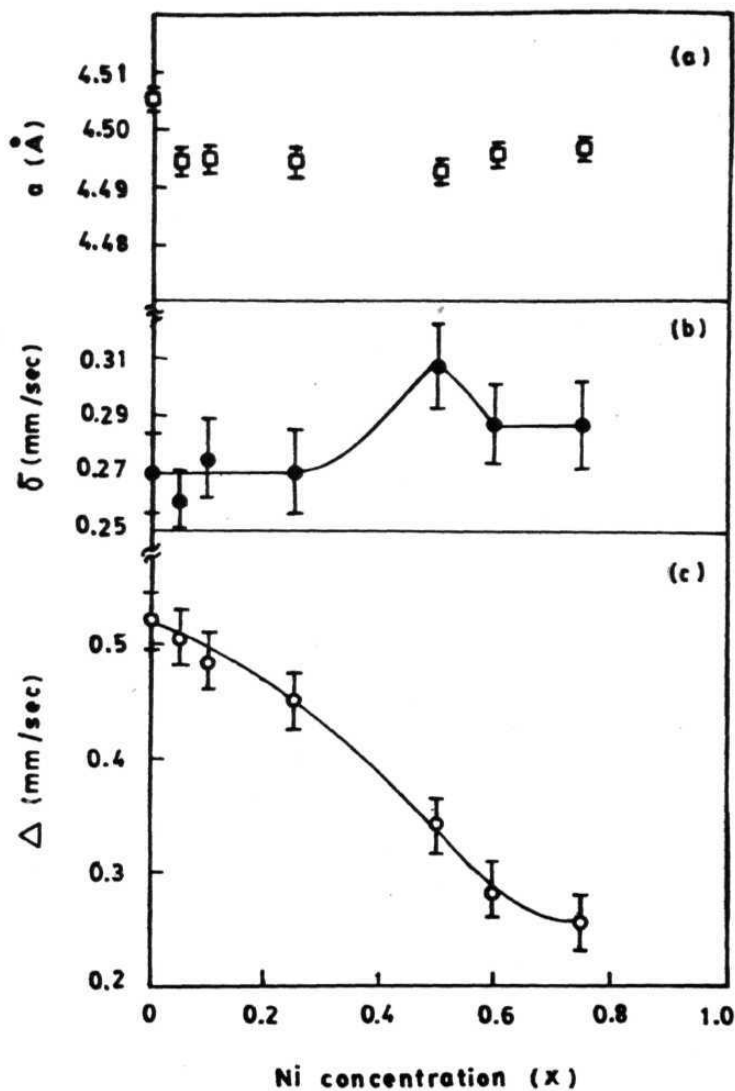


Fig.7.4. Variation of cubic lattice paraneter (a), isomer shift δ (relative to α - Fe) and guadrupole splitting Δ with nickel concentration (x) in $(\text{Fe}_{1-x}\text{Ni}_x)_{0.5}\text{Si}_{0.5}$ alloys.

the right of Fe in **the** periodic table (and vice versa). This is consistent with the observed decrease of Fe charge for Ni **substi-**tuted alloys. A slight increase in **isomer** shift data also shows a decrease in the Fe (3d + 4s) electron density with Ni addition [10].

7. 4. **CONCLUSIONS**

The observed quadrupole splitting at Fe in FeSi can be explained by lattice ionic contribution and this behaviour is consistent with other **Kondo** insulators and their properties. With addition of Ni, there is a decrease in quadrupole splitting and this has been attributed to charge transfer from Fe to Ni based on calculations of Akai et. **al.** It would be of interest to see how this charge transfer affects the anomalous transport properties of FeSi.

References

- [1] L. Pauling and A.M. Soldate, Acta Cryst. 1, 212 (1948).
- [2] **G.K. Wertheim**, V. Jaccarino, J.H. **Wernice**, J.A. Seitchik, H. Williams and **R.C. Sherwood**, Phys. **Lett.18**, 89 (1965).
- [3] V. Jaccarino, G.K. Wertheim, J.H. Wernick, L.R. Walker and Sigwards **Arajs**, Phys. Rev. 160, 476 (1967).
- [4] H. Watanabe, H. **Yamamoto** and K. **Ito**, J. Phys. **Soc. Japan** 18, 995 (1963).
- [5] Z. Schlesinger, Z. Fisk, **Hai-Tao** Zhang, M.B. Maple, J.F. DiTusa and G. Aepple, Phys. Rev. Lett. 71, **1748** (1993).
- [6] K. Toman, Acta Cryst. **4**, 462 (1951).
- [7] L. Pauling, Nature, London 161, 1019 (1948).
- [8] K.D. Sen and **P.C. Schmidt**, Phys. Rev. **A23**, 1026 (1981).
- [9] H. Akai, **M. Akai**, S. **Blügel**, B. Drittler, H. Ebert, K. Terakura, R. Zeller and P.H. Dederichs, Progr. **Theor. Phys. Suppl.** 101, 11 (1990).
- [10] T.V.S.M. Mohan Babu and C. Bansal, Phys. Stat. Sol.(b) 177, K83 (1993).
- [11] D.A. Bonn, J.D. Garrett and T. **Timusk**, Phys. Rev. **Lett.** 61, 1305 (1988).
- [12] F.E. Pinkerton, A.J. Sievers and J.W. Wilkins, Phys. Rev. Lett. 47, 1018 (1981).

SUMMARY

The results of the work described in this thesis can be summarised as follows:

It was possible to exploit the high sensitivity of the **Mössbauer** technique to the **chemical environment**, coupled with complimentary susceptibility and **FMR** measurements, to study the richness of the magnetic structure of $\text{Fe}_{3-x}\text{Mn}_x\text{Si}$ ternary alloys in detail. The competing exchange interactions together with the specific site substitution behaviour in this system were found to give rise to distinct hyperfine field variations at sites with different neighbour environments. The reentrant transition at low temperatures has been reasoned to be due to spin canting which can **accomodate** the competing exchange interactions. A better understanding of the magnetic behaviour of this complex system has therefore emerged from this study.

The addition of Cr to Fe_3Si showed that the solubility of Cr is limited upto $x = 0.5$ in $\text{Fe}_{3-x}\text{Cr}_x\text{Si}$ alloys and the presence of Cr_3Si phase is observed beyond $x = 0.5$ composition. This is in contrast to Mn and V additions to Fe_3Si which show solubility over a wide concentration range. In the Cr substituted alloys, the presence of B32 and B2 ordered structures in addition to DO_{19} order is also indicated.

In the $\text{Fe}_{3-x}\text{Mn}_x\text{Si}$ alloy system it is not possible to get the

chemically disordered state even by rapid **quenching**, whereas the situation in $\text{Fe}_{3-x}\text{Mn}_x\text{Al}$ alloy system is favourable and it is easy to get chemically disordered alloys in this system by a moderate quenching rate. A study of the changes in magnetic behaviour due to chemical ordering was carried out and a very pronounced effect of near neighbour environments on the hyperfine field distributions was observed. The presence of Mn in Fe_3Al was found to stabilise the B2 phase which is only a **metastable** phase between 550°C and 800°C in Fe_3Al . The kinetics of ordering at the inequivalent sites were seen to be distinct and this is an interesting observation. Magnetic measurements on $x = 1.2$ composition alloy showed reentrant behaviour similar to the Mn substituted Fe_3Si system.

Addition of Si to the **fcc** Ni_3Fe system made it possible to see the effect of Si first neighbours on the hyperfine field at Fe in an **fcc** lattice and it was found that the field reduction at Fe site due to Si first neighbour is larger as compared to Si first neighbours in the bcc lattice. On ordering, Si showed a preferential substitution for Fe sites in the L_{12} ordered structure and it is also suggested that a better degree of ordering may be achieved for the sluggishly ordering Ni_3Fe permalloy due to the presence of Si.

The quadrupole splittings were measured in the $(\text{Fe}_{1-x}\text{Ni}_x)_a(\text{Si})_b$ alloy system. A calculation of EFG for FeSi based on ionic character of the lattice gave a good agreement

with experimental value. This suggests that FeSi also has ionic character similar to other Rondo insulators. The transport **pro-** properties of these systems have attracted considerable interest. Addition of **Ni** to FeSi decreases the quadrupole splitting at Fe due to charge transfer effects and it would also be of interest to study the transport properties of this ternary system.